

A Northwest-Southeast Asymmetry in the Crab Supernova Remnant

by

Allison Loll

A Dissertation Presented in Partial Fulfillment
of the Requirements for the Degree
Doctor of Philosophy

ARIZONA STATE UNIVERSITY

May 2010

© 2010 Allison Loll
All Rights Reserved

A Northwest-Southeast Asymmetry in the Crab Supernova Remnant

by

Allison Loll

has been approved

April 2010

Graduate Supervisory Committee:

Steven Desch, Chair

Paul Scowen

Sumner Starrfield

Rogier Windhorst

John Shumway

ACCEPTED BY THE GRADUATE COLLEGE

A Northwest-Southeast Asymmetry in the Crab Supernova Remnant

by

Allison Loll

has been approved

April 2010

APPROVED:

, Chair

Supervisory Committee

ACCEPTED:

Department Chair

Dean, Graduate College

ABSTRACT

This dissertation presents results from a Hubble Space Telescope WFPC-2 imaging survey of the Crab Nebula in F502N ([O III]), F673N ([S II]), F631N ([O I]) and F547M (continuum). These observations have revealed several Northwest-Southeast (NW-SE) asymmetries in the morphological properties of the nebula that I attribute to the proper motion of the pulsar in the NW direction. The spin-down luminosity of the pulsar generates the pulsar wind nebula (PWN) which remains centered around the pulsar in time. The pressure of the PWN has caused a shock that propagates into freely-expanding ejecta; due to the pulsar's proper motion, the shock has propagated farther in the NW direction than it has in the SE. Assuming that density of the ejecta decreases with distance from the explosion center, I show that the shock is encountering lower density ejecta in the NW causing higher shock speeds there than in the SE. The difference in shock speeds has caused a NW-SE asymmetry in the formation of filaments and the length and development of Rayleigh-Taylor fingers. I applied an existing theoretical model of PWN to the Crab and found that the pulsar's NW motion has prevented acceleration of the filaments in the SE, explaining why the SE shows an unorganized morphology and lacks long R-T fingers. In the NW, the interface has been accelerating for at least 100 years, and the R-T instability has produced very long, well-developed fingers. I utilized the continuum image to study the correlation between dust (seen via extinction of synchrotron emission) and low-ionization gas and found that dust can be found everywhere that there is low-ionization emission; this suggests the dust formed in the supernova explosion and was swept up with the gas as the shock passed through. I have estimated the gas-to-dust

ratio of several filaments to be in the range of 0.050-0.100, several times higher than what is typical for the interstellar medium.

This dissertation is dedicated to my husband, Joseph, and my son, Brandon, for their unconditional love and support during these many years.

ACKNOWLEDGMENTS

I would like to acknowledge the support for this work that I was given by the Arizona State University/NASA Space Grant, the ASU Department of Physics and the ASU School of Earth and Space Exploration. Support for this work was also provided by STScI grant HST-GO-08222.01-A.

First and foremost, I would like to thank my husband, Joseph, and my son, Brandon, for always being supportive and understanding in my pursuit of this degree and the time and effort it took to obtain it. They have seen the best and worst of my days, and yet have always encouraged me to continue and do whatever it took to finish this.

My advisor, Steven Desch, has been the most influential person in the completion of this degree. Thank you, Steve, for taking the scattered puzzle pieces and helping me put them together in such a way that I am able to tell a magnificent story about a magnificent astrophysical object.

I would also like to thank Jeff Hester, who devoted years to teaching me about the Crab Nebula and many other astrophysical phenomena, and my committee members: Paul Scowen, Sumner Starrfield, Rogier Windhorst, and John Shumway, who have each gone out of their way to help and encourage me during my time at ASU. I have been fortunate to have help from various other collaborators as well, including Ravi Sankrit, William Blair, Jon Morse, and Lisa Will. I must also thank my first mentor, Sharon Montgomery, for doing all she did to prepare me for graduate school, including those seven most memorable nights observing at McDonald Observatory.

I couldn't have completed this degree without the love and support of the many

friends that I have met during this time. I thank all of you for your friendship during graduate school. I personally want to thank Keely Snider, Amber Straughn, Russell Ryan, Steven Finkelstein, Todd Veach, Joseph Foy, Kevin Healy, Kazuyuki Tamura, Seth Cohen, and Jennifer Neakrase. You have all become part of some of my best memories and will forever be special people in my life.

My family has been incredibly supportive of my education my entire life and I want to thank them for always believing I could do this. I want to thank my mother, Elaine, for laying in the driveway with me late at night to watch meteor showers and lunar eclipses. I thank my brothers and sisters: Nelson, Teresa, Russell, Carolyn, and Kevin, for their continued support. Carolyn, you have been there for me in so many ways, and I hope that I can be as good to you as you have always been to me.

I send a final thank you to everyone in my life, new friends and old, encouraged and believed in me then and now.

TABLE OF CONTENTS

	Page
LIST OF TABLES	xi
LIST OF FIGURES	xii
CHAPTER 1 INTRODUCTION	1
1.1 Overview of Supernova Explosions	1
1.2 Pulsars and Associated Pulsar Wind Nebulae	6
1.3 Background of the Crab Nebula	12
1.3.1 Overview of the Crab Pulsar	14
1.3.2 Overview of the Filaments	20
1.3.3 Interaction of the Pulsar Wind and the Ejecta	24
1.3.4 Magnetic Fields in the Crab Nebula	29
1.4 Dust in the Crab Nebula	34
1.5 Overview of this Dissertation	37
CHAPTER 2 <i>HST</i> <i>WFPC-2</i> OBSERVATIONS OF THE CRAB NEBULA	41
2.1 Data Reduction	41
2.2 Creating <i>HST</i> mosaics	45
2.3 Overview of <i>HST</i> Observations	57
2.4 Supporting Observations	60
2.4.1 Fabry-Perot Data	60

CHAPTER	Page
CHAPTER 3 The Variation of Pre-Shock Ejecta Density	64
3.1 The Effect of the Nebula’s Geometry on Ejecta Density	65
3.2 Constructing a 3-D Ellipsoid to Model the Crab Nebula	68
3.3 The Pre-shock Ejecta Density is Asymmetrical	77
3.4 Results	78
CHAPTER 4 Varying Shock Speeds Around the Perimeter of the Crab . . .	81
4.1 Shock Properties as a Function of Preshock Ejecta Density	81
4.2 Observational Support of Varying Shock Speed	85
4.2.1 Containment of the Synchrotron Nebula	87
4.2.2 An Asymmetry in the Ionization Structure of the Filaments .	91
4.3 Results	96
CHAPTER 5 A Theoretical Model for the NW-SE Asymmetry	100
5.1 Existing Numerical Model of PWN and Ejecta	100
5.2 Limitations of the Existing Model	106
5.3 Applying the Existing Model to the Crab Nebula	109
5.3.1 Predicting an Asymmetrical Rate of Expansion	110
5.3.2 Predicting the Asymmetry of R-T Fingers	114
5.3.2.1 Ages of R-T Fingers	115
5.4 Results	118
CHAPTER 6 An NW-SE Asymmetry in the Filaments and R-T Fingers . .	120

CHAPTER	Page
6.1 Introduction	120
6.2 An Asymmetry in the Thickness and Density of the Filaments	123
6.3 An Asymmetry in the Morphology of R-T Fingers	129
6.3.1 R-T Finger Lengths and Development	130
6.3.2 Ionization Structure at the Tips of R-T Fingers	134
6.4 Proper Motions of R-T Fingers	141
6.4.1 Development of R-T fingers in Time	146
6.5 Results	149
CHAPTER 7 Dust Extinction in the Crab	154
7.1 Introduction	154
7.2 Dust Absorption in the Crab Nebula	159
7.3 Correlating Dust Absorption Features with Low-Ionization Emission	160
7.4 Results	181
CHAPTER 8 Conclusions	186
8.1 Summary	186
8.2 Future Work	193
REFERENCES	196

LIST OF TABLES

Table		Page
1	Exposure Dates and Pointing Information for <i>HST</i> Observations . . .	41
2	Fits used to align the <i>HST</i> Observations	46
3	<i>HST</i> Filter bandpass properties	55
4	Comparison of Fluxes Between Calibrated <i>HST</i> Images and Observed Spectra	56
5	Projection of the expansion index, a , ± 100 years in the NW and SE.	117

LIST OF FIGURES

Figure	Page
1. Phases of Supernova Remnant Evolution	7
2. Synchrotron Nebula in Different Wavelengths	16
3. Image of Crab Pulsar	19
4. Examples of Filaments, R-T Fingers, and the Cooling Region	22
5. Interaction of PWN and Freely Expanding Ejecta	26
6. Geometry of Magnetic Field Around the Pulsar	30
7. Fields of Observations	43
8. Oxygen I Mosaic	50
9. Sulfur II Mosaic	51
10. Oxygen III Mosaic	52
11. Continuum Mosaic	53
12. Combined Color Mosaic	54
13. 2-D Ellipse Fit to Edge of Nebula	69
14. Ellipsoid	73
15. Geometry of Ellipsoid Angles	74
16. 3-D Distances Around the Perimeter	76
17. Cooling Function	86
18. Comparison of Shock and Synchrotron Nebula in NW	88
19. Comparison of Shock and Synchrotron Nebula in South	90
20. Comparison of Shock and Synchrotron Nebula in SE	92

Figure	Page
21. Locations where Line Profiles were Taken	93
22. Emission Line Profiles at the Edge of the Nebula (1)	94
23. Emission Line Profiles at the Edge of the Nebula (2)	95
24. Projected Evolution of the Nebula	116
25. Emission Line Profiles of Filaments	125
26. Oxygen III - Sulfur II Image of Filaments	128
27. Asymmetry in R-T Finger Length	131
28. Histogram of R-T Finger Lengths	132
29. Histogram of Separation of Fingers	135
30. Line Intensities of R-T Fingers	137
31. Line Intensities for R-T Fingers in the NW	138
32. Proper Motions of R-T Fingers (1)	144
33. Proper Motions of R-T Fingers (2)	145
34. Dust in the Nebula	161
35. Transmission of Oxygen III Filter	163
36. Region 1	166
37. Example of Determining Dust-to-Gas Ratios	168
38. Schematic of Dust in the Nebula	170
39. Region 2	174
40. Region 3	176
41. Region 4	180

CHAPTER 1

INTRODUCTION

The Crab Nebula is the remnant of a Type II supernova explosion that was first observed on Earth by Chinese astronomers on July 4, 1054 AD. The nebula was visible in the daytime sky for two weeks and in the night sky for nearly two years before becoming too dim to be seen with the naked eye (Clark & Stephenson 1977). The Crab was rediscovered telescopically in 1731 by the English astronomer John Bevis and is the first object listed in Charles Messier's famous catalogue of non-cometary objects (M1). Due to its close proximity, about 2 kpc (Trimble 1968), and being one of the youngest supernova remnants in the Galaxy, the Crab remains one of the most studied objects in all of astrophysics.

1.1. Overview of Supernova Explosions

Supernova (SN) explosions can be categorized as one of two types: Type I (a,b, and c), and Type II, with the type being determined by their observed spectral properties. The following review of supernovae draws heavily on Hansen, Kawaler, & Trimble (2004) and (Carroll & Ostlie 1996). Type Ia supernovae contain no hydrogen in their spectrum and they can be found in all types of galaxies and stellar populations. The population of Type Ia SN regardless of the age of the environment implies that a change in metallicity can not account for the lack of hydrogen in the spectra of these objects. Theoretical models indicate that Type Ia explosions occur when a carbon-oxygen white dwarf accretes material from a nearby companion in a red giant phase (Carroll & Ostlie 1996). Due to the equation of state for a white dwarf ($P \propto \rho^{5/3}$), when matter is accreted onto the degenerate core the star will decrease in volume and increase in density (Hansen, Kawaler, & Trimble 2004). When the mass

of the white dwarf reaches about $1.3M_{\odot}$, the pressure and compressional heating are high enough to begin nuclear burning. Due to the degenerate nature of the star, there is a runaway explosion that completely disrupts the white dwarf, leaving nothing from the core intact (Carroll & Ostlie 1996). The light curves of all Type Ia supernovae decline in brightness at a remarkably consistent rate, about 0.065 magnitudes per day after they reach maximum brightness (at ≈ 20 days), because the light curves correspond to the radioactive decay of specific elements (Carroll & Ostlie 1996).

The Crab Nebula is thought to be the result of a Type II “core-collapse” supernova explosion (Chevalier 1977). There are three types of core collapse supernovae and they are classified as types Ib, Ic, and II. These differ only in the presence or absence of hydrogen emission in the spectra, or likewise the presence of a hydrogen atmosphere at the time of the explosion. The supernova occurs when a star more massive than $8M_{\odot}$ (Iben & Renzini 1983) can no longer undergo exothermic nuclear fusion in the stellar core. Massive stars begin like all others, fusing hydrogen into helium in the core until the supply of hydrogen runs out. Next, helium is fused to make carbon and oxygen in the core via the CNO cycle, with a shell surrounding the core where the temperature is high enough for hydrogen burning. This is the final phase of nuclear processing in low mass stars ($< 8M_{\odot}$), but stars with masses greater than $\approx 8M_{\odot}$ will fuse successively heavier elements, producing an onion-like structure with shells of higher level nuclear burning at the center and successively lower levels of nuclear burning in shells surrounding the core. The duration of each nuclear burning cycle becomes shorter and shorter because fusing heavier elements

requires extremely high temperatures, which means that the reaction rates are faster and the luminosities are higher. In addition, the binding energies of heavier nuclei are greater which causes the fusion of heavier elements to produce less energy per gram. For the core to have enough pressure to support the star, more reactions must take place per time interval. Fusion of heavier and heavier elements continues until the core is made up of iron nuclei (and iron-peak elements) and is supported by electron degeneracy pressure. Nuclear fusion goes no further than iron because the fusion of iron is an endothermic reaction and would decrease pressure support of the star. At this point, there are still shells of nuclear processing surrounding the core. The silicon-burning layer surrounding the core continually deposits iron-ash onto the core. As in the case of the white dwarf mentioned above, when mass is added to degenerate material the volume shrinks, increasing the pressure and temperature. This raises the mean energy of the thermal photons enough to photodissociate iron via the reaction ${}^{56}_{26}\text{Fe} + \gamma \rightarrow 13{}^4_2\text{He} + 4n$, which is followed by ${}^4_2\text{He} + \gamma \rightarrow 2p^+ + 2n$. At this point, the temperatures in the core are high enough ($\approx 10^{10}$ K) that electron capture (or inverse beta decay) also takes place and turns protons into neutrons by the reaction $p^+ + e^- \rightarrow n + \nu_e$. The combination of these two reactions and the energy being lost due to escaping neutrinos is detrimental to the survival of the star; pressure equilibrium between the reactions occurring in the core and surrounding shells and the outer stellar layer no longer exists.

The continuing deposition of iron ash onto the core eventually causes the core to reach the critical mass known as the Chandrasekhar Limit ($M \approx 1.4M_{\odot}$) where

even electron degeneracy pressure can no longer support the weight of the outer stellar layers, and the core collapses (Hansen, Kawaler, & Trimble 2004). The core collapses homologously (i.e. the speed of collapse is directly proportional to the distance from the center) in a matter of seconds. Once the density exceeds about $2.7 \times 10^{14} \text{ g cm}^{-3}$ and the radius of the core is only tens of kilometers, the nuclei are so close together that the strong force becomes repulsive (Carroll & Ostlie 1996). The core rebounds and sends pressure waves (which steepen into a shock) throughout the outer stellar layers. The pressure of trapped neutrinos adds to the energy of the shock, causing the star to explode (Bethe & Wilson 1985).

The energy released in this explosion can be estimated by calculating the total gravitational potential energy available, $|\Delta\Omega| \approx GM^2/R$. Estimating a mass of $1M_{\odot}$ and a radius of 10 km for the neutron star, the energy released is on the order of 10^{53} ergs and this is consistent throughout Type II core collapse supernovae. About 10^{51} ergs is in the form of kinetic energy via a shockwave while the majority of the energy is released in neutrinos (Dopita & Sutherland 2003).

We now discuss the evolution of the star after the explosion, following Dopita & Sutherland (2003). The shock wave from the explosion drives all of the stellar layers above the core explosively outward at speeds of up to $30,000 \text{ km s}^{-1}$. Initially, the gas expands freely and the ejecta cool adiabatically. This is called the “fireball” stage. Thermal instabilities and incomplete mixing enhance the clumpiness of the ejecta. Models by Kifonidis et al. (2003) show that iron-group elements are distributed in overdense clumps within an anisotropic shell of ejecta expanding at speeds of

about $17,000 \text{ km s}^{-1}$. Between what would have been the Si/O and (C + O)/He boundaries of the progenitor star, Rayleigh-Taylor (R-T) instabilities and neutrino-driven convection cause this layer of ejecta to form clumps of metal-rich gas within minutes of the explosion and the clumpiness is enhanced as the gas expands and cools.

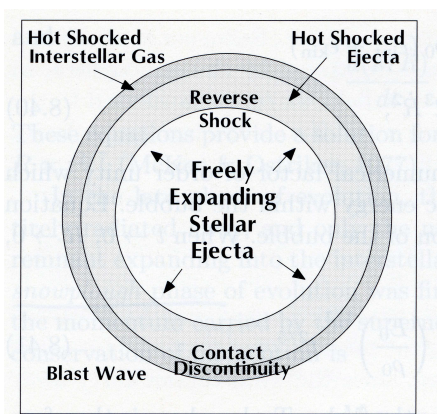
After a long period the expanding ejecta interacts with and sweeps up enough of the surrounding interstellar medium to develop a critically large pressure difference between the two media. When this occurs, a second shock wave is driven into the interstellar medium with a velocity determined by the speed of the fastest moving ejecta. The shock plows through the interstellar medium and is quickly slowed down as it sweeps up mass, causing a reverse shock to begin propagating back toward the explosion center, through the freely expanding ejecta. At this point there is a shell of freely expanding material at the center, surrounded by hot shocked ejecta which is separated from the outermost hot shocked interstellar gas by a contact discontinuity, as shown in Figure 1. Eventually the reverse shock propagates through all of the supernova ejecta, heating the gas to high temperatures. At this time, the mass of gas that has been swept up by the outward moving blast wave is greater than the mass expelled during the explosion. This marks the beginning of the Sedov-Taylor phase. During this phase, the pressure of the expanding, hot shocked ejecta serves to keep the initial blast wave propagating outward and the kinetic and thermal energies are equal and conserved. The shock will continue to slow as it pushes into more ISM, and eventually the dynamical expansion time ($\tau_{exp} = R/v_s$) becomes less than the cooling time of the shocked gas, and a layer of cooled ISM forms at the boundary between the

shock and the hot, shocked ejecta. The thermal energy of the shockwave is radiated away, decreasing the overall energy of the hot, shocked ejecta which is driving the shock. When all of the thermal energy of the ejecta has radiated away, the remnant continues to expand due to the momentum of the dense ISM shell. This phase is called the “snowplow phase” and it continues until the expansion velocity becomes subsonic with respect to the ISM that it is moving into. The remaining energy is dissipated away through turbulence in the physical interaction with the ISM.

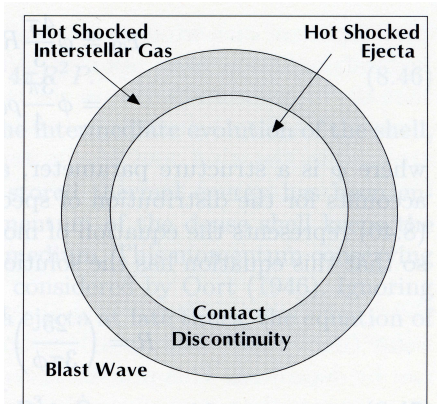
There are two other types of core collapse supernova explosions - Type Ib and Type Ic. The main difference, observationally, is that neither Type Ib or Type Ic supernovae show evidence of hydrogen in their spectra, similar to Type Ia supernovae. Both Type Ib and Ic supernovae have only been found in spiral galaxies and in young stellar populations and are therefore believed to be the result of dying massive stars that have lost their hydrogen envelope. The current theories suggest that these stars have main-sequence masses of about $20M_{\odot}$ and either transfer the hydrogen envelope to a close binary or lose the envelope to pre-supernova stellar winds, leaving a $4-6M_{\odot}$ helium layer and the onion-shell structure of nuclear burning moving toward the core. The core is eventually composed of degenerate iron and collapses as discussed above. The presence or absence of helium in the Type Ib and Ic supernovae is believed to be due to the original metallicity of the progenitor.

1.2. Pulsars and Associated Pulsar Wind Nebulae

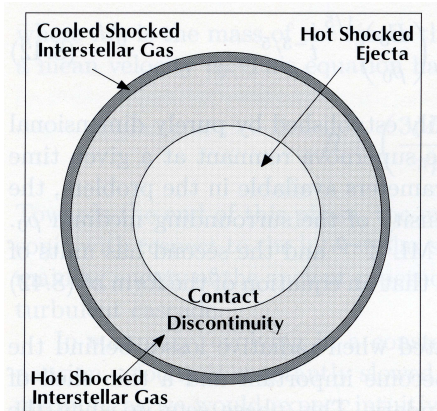
Type II, core-collapse supernova eject all of their stellar layers outward but the core will remain intact. The core may be in the form of a neutron star (if the



a. Supernova Remnant: pre Sedov-Taylor Phase



b. Supernova Remnant: Sedov-Taylor Phase



c. Supernova Remnant: post Sedov-Taylor Phase

Figure 1. Cartoon representing the fireball, Sedov-Taylor, and snowplow phases of a core collapse supernova explosion. [Taken from Dopita & Sutherland (2003).] Since the Crab Supernova occurred in a relatively empty region of space, a reverse shock has not formed and the original blastwave is continuing outward.

progenitor had a mass between $8-25M_{\odot}$) or a black hole ($M > 25M_{\odot}$) (Carroll & Ostlie 1996). Neutron stars have masses that are around the Chandrasekhar limit ($1.4M_{\odot}$) and less than the Oppenheimer-Volkoff limit, which is the upper limit for hydrostatic equilibrium for a neutron star [$5M_{\odot}$, Bradt (2008)]; above this mass, the neutron star would collapse to a black hole. The radius of a neutron star is about 10 km (Hansen, Kawaler, & Trimble 2004), meaning the density of these compact objects reaches about $2 \times 10^{15} \text{ g cm}^{-3}$ (Hansen, Kawaler, & Trimble 2004). Due to the extremely high density of neutron stars, general relativity must be considered as well as nuclear forces when describing the equation of state.

Asymmetries during core collapse cause the neutron star to be pushed or “kicked” in a random direction, with typical velocities being about $400-500 \text{ km s}^{-1}$ (Gaensler & Slane 2006). Interestingly, there is a tendency for neutron stars to have a “spin-kick” alignment, meaning that their rotation axis is aligned with their proper motion (Johnston et al., 2005, Wang et al., 2006). Wang et al. (2007) created a model that suggests that an initial angular momentum of the neutron star is required to achieve the spin-kick alignment. An asymmetric release of neutrinos can also result in the alignment if there are extremely strong magnetic fields present or if the neutron star is in a very rapid spin.

Core collapse supernova events may form a pulsar, a rapidly rotating neutron star with a strong magnetic field ($B \approx 10^{12} \text{ G}$) that emits pulses of light that are precisely spaced in time. As discussed in Shapiro & Teukolsky (1983), a picture now commonly accepted for pulsars is the so-called magnetic dipole model, which

consists of a rapidly rotating neutron star that has a magnetic dipole oriented at an angle α from the rotation axis. Pulsars cannot be axisymmetric; emission from an axisymmetric system would not change with time to produce the pulses of energy coming from these stars. The time-variance we see is due to the tilt of the magnetic axis with respect to the axis of rotation. Since the magnetic dipole is not aligned with the axis of rotation, the magnetic field at any location on the neutron star's surface changes constantly as the pulsar rotates. The origin of the pulsed emission from pulsars, according to most theoretical models, is due to the radiation being emitted in a narrow, conical beam of radiation that is fixed with the magnetic dipole (not the rotation axis) and that is co-rotating with the neutron star. As the beam rotates, an observer on earth notes "pulses" of emission that occur when the beam is pointed at (strong pulse) or away from (weaker pulse) our line of sight.

The rotating magnetic dipole generates a rotating magnetosphere around the pulsar. The strong magnetic fields associated with pulsars (10^{12} G) permits pair-production, which is when photons produce electcharged particles become trapped in the strong magnetic field and are accelerated around the magnetic fields lines (Ruderman & Sutherland 1975). Ions may be lost at the equatorial region to maintain charge neutrality (Gaensler & Slane 2006) and may also be trapped in the relativistic flow. The particles are accelerated as they spiral around magnetic field lines and they radiate via synchrotron emission. Synchrotron emission, characterized by being highly linearly polarized in the plane of the circular motion of the accelerated particles (Carroll & Ostlie 1996), carries energy away from the pulsar (Kennel & Coroniti

1984a). The dissipation of the rotational kinetic energy of the pulsar into the magnetic and particle energies is referred to as the “spin down luminosity” ($L_{\text{spin}} = |\dot{E}|$) of the pulsar.

The spin down luminosity is dependent on both the magnetic field and the rotational kinetic energy of the pulsar. The magnetic field at the pole of the pulsar, B_p , is related to the magnetic dipole moment $|m|$ according to $|m| = B_p R^3/2$ where R is the radius of the neutron star. The energy radiated away in the form of relativistic particles (synchrotron emission) is determined by $\dot{E} = -(2/3)c^{-3} |\ddot{\mathbf{m}}|^2$. The magnetic moment is defined as $\mathbf{m} = (B_p R^3/2)(e_{\parallel} \cos(\alpha) + e_{\perp} \sin(\alpha) \cos(\Omega t) + e'_{\perp} \sin(\alpha) \sin(\Omega t))$, where Ω is the angular velocity of the pulsar, e_{\parallel} is a unit vector parallel to the rotation axis, and orthogonal to the rotation axis are the fixed vectors e_{\perp} and e'_{\perp} . Taking the derivative of \mathbf{m} twice and substituting into the equation for \dot{E} shows that the spin-down luminosity is

$$\dot{E} = -\frac{B_p^2 R^6 \Omega^4 \sin^2 \alpha}{6c^3}. \quad (1.1)$$

The synchrotron emission originates from the rotational kinetic energy of the pulsar given by $E = (1/2)I\Omega^2$, and therefore $\dot{E} = I\Omega\dot{\Omega}$. Since \dot{E} is negative, this implies that $\dot{\Omega}$ is negative, or that the pulsar is slowing down in time. Typical values for pulsar spin-down luminosities are between $\approx 10^{28} - 10^{38}$ erg s⁻¹. This is to be compared to the typical rotational kinetic energies where $E \approx 1/2(2MR^2/5)(\Omega)^2$, $M \approx 2M_{\odot}$, $R \approx 10$ km, $\Omega \approx 2\pi(30\text{ms})^{-1}$ giving a rotational kinetic energy of about 3×10^{49} erg.

The pulsar can continue to convert its rotational energy into particle energy for at least 10^4 years. Positrons and electrons stripped from the pulsar’s poles become

trapped in the magnetic field and are accelerated to relativistic speeds. The acceleration of the particles causes them to emit synchrotron radiation (Gaensler & Slane 2006). These relativistic particles form amorphous-looking nebulae referred to as a pulsar wind nebulae (PWN) or synchrotron nebulae. The supernova remnants themselves are called “filled-center” supernova remnants (SNRs) because their centers are “filled” with energetic particles that induce radiation. The Crab is a young, nearby example of this class of SNR, which includes up to about 50 other known examples between our Galaxy and the Magellanic Clouds (Gaensler & Slane 2006).

The evolution of PWN have added complexities compared to the typical core-collapse supernovae discussed above. Just after the explosion, the PWN is near the center of the expanding ejecta because the neutron star or pulsar has not moved much. The pressure in the PWN at this time is much larger than the pressure in the ejecta immediately surrounding it and therefore expands so rapidly that a shock is driven into the ejecta. The expansion velocity of the PWN continues to increase, and the relativistic particles have a sound speed equal to $c/\sqrt{3}$ (J.L. Synge, 1956), keeping the amorphous synchrotron nebula always relatively centered on the pulsar. Relativistic jets, such as what is seen in the Crab Pulsar, may cause the synchrotron nebula to be non-spherical, but nonetheless the synchrotron nebula is symmetrically distributed around the pulsar. The rotation of the pulsar causes the toroidal magnetic field to increase and the Poynting flux ($\mathbf{F} = \mathbf{E} \times \mathbf{B}$) varies with the angle from the rotation axis (Gaensler & Slane 2006). Conservation of energy flux along the magnetic field lines causes the Lorentz factor, defined as $\gamma = (1 - v^2/c^2)^{-1/2}$, of the wind to vary

with latitude ($\gamma \propto \sin^2\Phi$, where Φ is the angle from the rotation axis), such that γ is smallest at the poles. The magnetization parameter, defined by $\sigma = B^2/(4\pi\rho\gamma c^2)$, is much greater at the poles of the neutron star than it is at the equator. This variation along the surface of the pulsar creates the toroidal structure of the pulsar wind nebula, such that the nebula is elongated along the pulsar spin axis, and models suggest that jets form due to the collimation of the magnetic field lines that are in the direction of the rotation axis (Gaensler & Slane, 2006, and references therein).

Eventually, after the nebula has reached the Sedov-Taylor phase discussed above, the reverse shock will collide with the outward moving PWN. A typical timescale for this interaction to occur is a few thousand years (Blondin et al. 2001). By this time, a pulsar (and PWN) that has a high proper motion will no longer be located at the center of the supernova remnant and any asymmetries in the expansion of the supernova ejecta further complicate the evolution; models of this interaction show large distortions in the morphology of the PWN which can cause the PWN to no longer be centered on the pulsar (Gaensler & Slane 2006). This is the likely the eventual fate of the Crab Nebula.

1.3. Background of the Crab Nebula

The Crab Nebula is a relatively young remnant (955 yr), and the proximity of the nebula to Earth (2 kpc) provides a unique opportunity to study this object. The Crab has been the prototype for studying Type II supernovae, but it has some unique characteristics that should be addressed. Perhaps most importantly, HI observations show that the Crab Nebula exists inside a relatively empty bubble that has a radius

of about 90 pc (Romani et al. 1990). The visible Crab supernova remnant has dimensions of only 4.4×2.9 pc (Hester 2008). The outermost ejecta, if expelled at a velocity of about $10,000 \text{ km s}^{-1}$, would have only traveled a distance of about 10 pc by this point. The Crab supernova explosion, therefore, is known to have been a cavity explosion. This is important for two reasons. First, the lack of surrounding interstellar medium (ISM) would affect the overall evolution of the remnant because the blastwave from the explosion would not be encountering a significant amount of gas to slow the propagation of the shock front. This means that the blast wave would have to travel significantly farther than in the typical Type II SN explosion before there is a large enough pressure difference between the shock and the ISM for a reverse shock to form. There has been no direct observation of emission that would be characteristic of either the original blastwave or a reverse shock in the region surrounding the Crab Nebula. The lack of an observable blast wave is understood because the Crab was a cavity explosion, and the emission levels of a tenuous ISM ($n \approx 0.01 \text{ cm}^{-3}$) would be below observational detection limits. Also due to the low density surroundings, the shock would not have the large pressure difference necessary for a reverse shock to form and propagate back into the nebula.

The Crab Nebula is a PWN and this also affects the evolution of the remnant. The PWN is expanding outward (driven by the spin-down luminosity of the pulsar) into the surrounding, freely expanding ejecta. The large pressure inside the PWN causes a shock to propagate into the freely expanding ejecta. This results in a thin (relative to the size of the nebula as a whole) layer of shocked, cooling gas that is

visible as thermal line emission at the outer boundary of the nebula. The thermal line emission tends to be concentrated into filaments. Since the Crab supernova was a cavity explosion, the filaments can be assumed to be composed of only stellar ejecta - not ISM. The ejecta is visible due to both radiative cooling behind the shock and subsequent photoionization from synchrotron radiation. This is a unique feature of the Crab Nebula because normally the ejecta from a Type II supernova explosion would be much too faint to be seen this long after the event because there is no energy source to excite the atoms to make the ejecta visible and observable.

It is best to think of the Crab Nebula as having three separate, and spatially distinct, visible components: the pulsar, the synchrotron nebula (or PWN), and the filaments. More ejecta lie well outside of the filaments but is not visible (Hester 2008). These three components interact with each other and form the quite dynamical nebula that we know as the Crab.

1.3.1. *Overview of the Crab Pulsar*

The supernova that produced the Crab Nebula contains a central pulsar, named PSR 0531-21, which is the only component of the progenitor star that is still intact after the explosion (once the stellar core). The Crab Pulsar was discovered in 1968 by Comella et al. (1969) using observations of the Crab Nebula in radio wavelengths, and this pulsar was the first pulsar to be associated with a supernova explosion. By measuring the time between the precise pulses of emission from the pulsar, Comella et al. (1969) determined the pulsar has a period of 33.3 ms.

The period of the pulsar is observed to be slowing at a rate of $\dot{P} = 4.21 \times 10^{-13}$ s s⁻¹ (Hester 2008). Using the moment of inertia for a sphere with $R = 10$ km and $M = 1.4M_{\odot}$, $I = (2/5)MR^2 \approx 1.1 \times 10^{45}$ g cm². Using $\Omega = 2\pi/P \approx 190$ s⁻¹ and $d\Omega/dt = -(2\pi)(P^{-2})(\dot{P}) \approx 2.4 \times 10^{-9}$ s⁻², then according to the equations above the energy loss associated with the Crab Pulsar is $L_{\text{spin}} \approx 5 \times 10^{38}$ ergs s⁻¹, and this energy is distributed into the surrounding synchrotron nebula. Particles, such as protons and electrons, become trapped in the magnetic field lines and are accelerated to relativistic speeds. This amorphous nebula, called the PWN or the synchrotron nebula, can be viewed at all wavelengths from X-ray to radio. Figure 2 depicts the spatial distribution of this radiation which overlays three wavelength regimes: The X-ray *Chandra* images of the pulsar highlight the innermost region of the synchrotron nebula (Hester et al. 2002); the *HST* data (from this dissertation) shows the synchrotron nebula in optical emission; and the *VLA* image shows the outermost regions of the synchrotron nebula at radio wavelengths (Bietenholz & Kronberg 1990).

Assuming a power-law electron spectrum and a constant supply of particles to the PWN from the pulsar, there is a point where the synchrotron radiation and inverse-Compton scattering losses exceed losses due to relativistic bremsstrahlung (free-free) radiation and adiabatic expansion. This occurs at the “breaking frequency”, defined as

$$\nu_b = 10^{21} \left(\frac{B_{\text{PWN}}}{1 \mu\text{G}} \right)^{-3} \left(\frac{t}{10^3 \text{ yr}} \right)^{-2} \text{ Hz} \quad (1.2)$$

where B_{PWN} is the magnetic field of the PWN. Most particles with energies above the breaking frequency ($\approx 4\text{MeV}$) radiate all of their energy quickly and never travel to

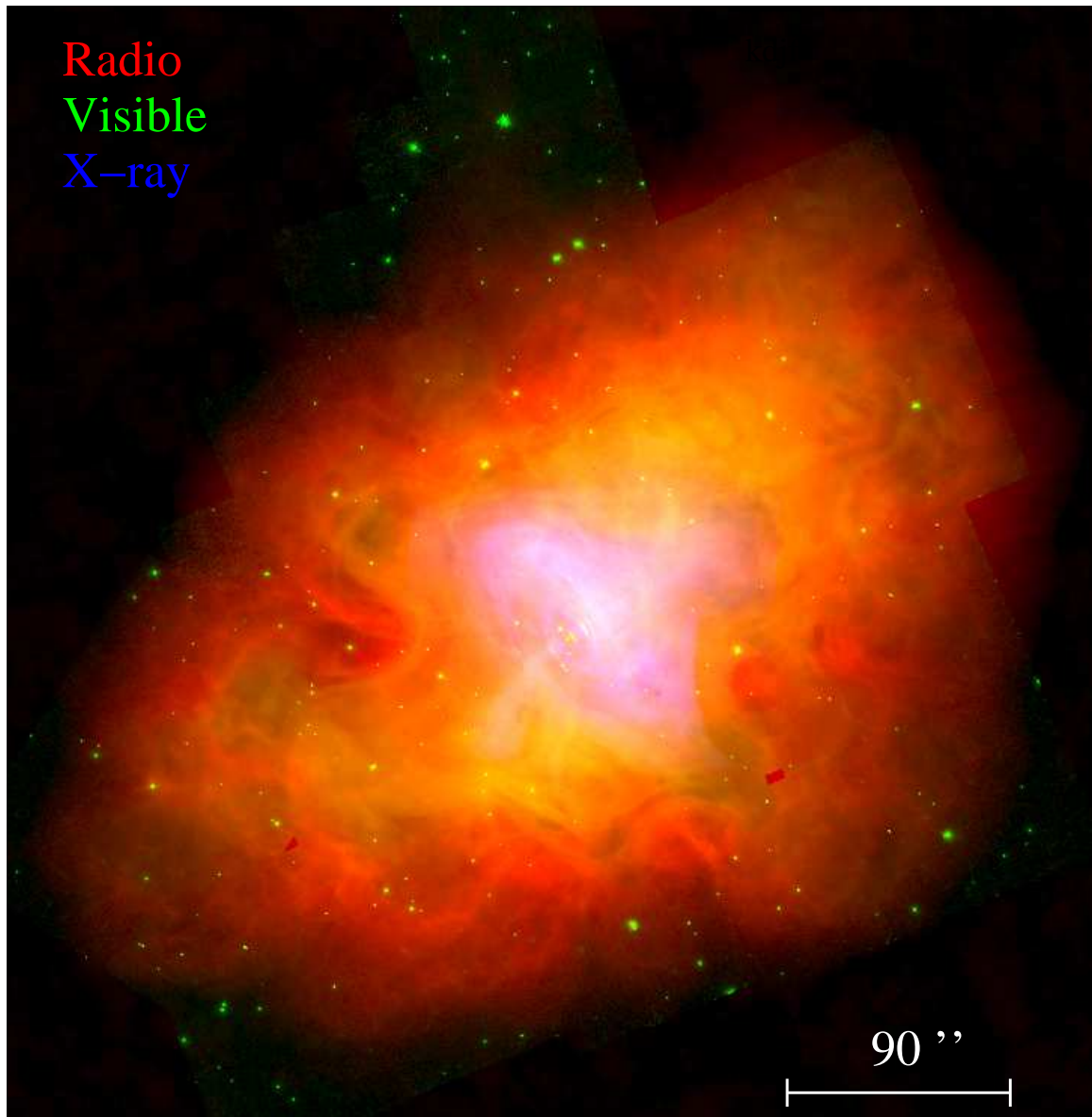


Figure 2. An image of the Crab Nebula showing the synchrotron nebula in various emission lines: X ray in blue [Chandra, (Hester et al. 2002)], visible emission in yellow (*HST*, this work) and radio wavelengths in red [VLA, (Bietenholz & Kronberg 1990)]. Assuming a distance to the Crab equal to 2 kpc, then $90'' \approx 0.87$ pc.

the edge of the nebula (Gaensler & Slane 2006) while particles with frequencies less than ν_b can travel farther distances. For this reason, the energy associated with the radiation decreases with increasing distance from the pulsar. The optical radiation emitted by the synchrotron nebula extends significantly farther from the pulsar than does the X-ray emission, while the radio emission is observed to extend the farthest from the pulsar.

Several studies have been done to measure the proper motion of the pulsar, with the most recent by Kaplan et al. (2008) giving $\mu_\alpha = -12 \pm 0.4 \text{ mas yr}^{-1}$ and $\mu_\delta = +4.1 \pm 0.4 \text{ mas yr}^{-1}$, with the total motion being about 13 mas yr^{-1} in the northwest direction. The equation relating proper motion to transverse velocity is

$$v_t = \frac{\mu(\text{''/yr})d}{206265\text{''/rad}} \quad (1.3)$$

so that with our values, $v_t = (13 \text{ mas yr}^{-1})(2000\text{pc})/206265\text{'' rad}^{-1}) = 1.2 \times 10^{-4} \text{ pc yr}^{-1}$, or about 120 km s^{-1} in the plane of the sky. This is slower than, but comparable to, the typical kick velocities of pulsars ($300\text{-}400 \text{ km s}^{-1}$). If we account for the tilt of the nebula into the sky by 30° , the likely velocity is more like 140 km s^{-1} .

The detailed energetics of the pulsar are best seen by looking at the pulsar's immediate environment. The *Chandra X-ray Observatory* image of the Crab Pulsar, shown in Figure 3, shows a torus of strong x-ray emission that appears elliptical along our line-of-sight to the nebula. The major and minor axes of the torus are approximately 83'' and 46'' , respectively. Assuming that the torus is nearly circular around the pulsar, Hester et al. (1995) determined that the torus is tilted about 33° into the plane of the sky, with the NW side being farther from Earth. Nearly

perpendicular to the torus there is a jet of X-ray emission (and an associated counter-jet) that are outflows of material from the pulsar. These jets flow outward about 0.25 pc along the toroid axis (Hester et al. 2002) in a southeast-northwest (SE-NW) direction. The jets of the pulsar, which are aligned with the pulsar spin axis, are remarkably symmetric with the proper motion of the pulsar (Ng & Romani 2006). In addition, the axis of the jet is in aligned with the overall symmetry of the nebula, being tilted about 130-140° E of N in the plane of the sky (Hester 2008). These angles of inclination are consistent with the geometry of the overall nebula (Lawrence et al. 1995). The overall elliptical nature of the nebula, though, is determined by the pulsar's magnetic field, which will be discussed in more detail in a subsequent section.

X-ray emission is observed closest to the pulsar in the form of a torus with long, X-ray jets streaming from the poles in a SE-NW direction (Hester et al. 2002). *Chandra* observations of the pulsar show a shock in the pulsar wind close to the pulsar as well as a torus of emission surrounding the pulsar (Hester et al. 2002). These jets associated with the shock lie along a line from the SE to the NW and generally follow the major axis of the elliptical shape of the nebula. The torus has been observed to vary on timescales of days, expanding outward from the pulsar. Both the jets and torus are carrying energy away from the pulsar, and the relativistic particles associated with these features experience energy losses from both synchrotron radiation and adiabatic expansion.

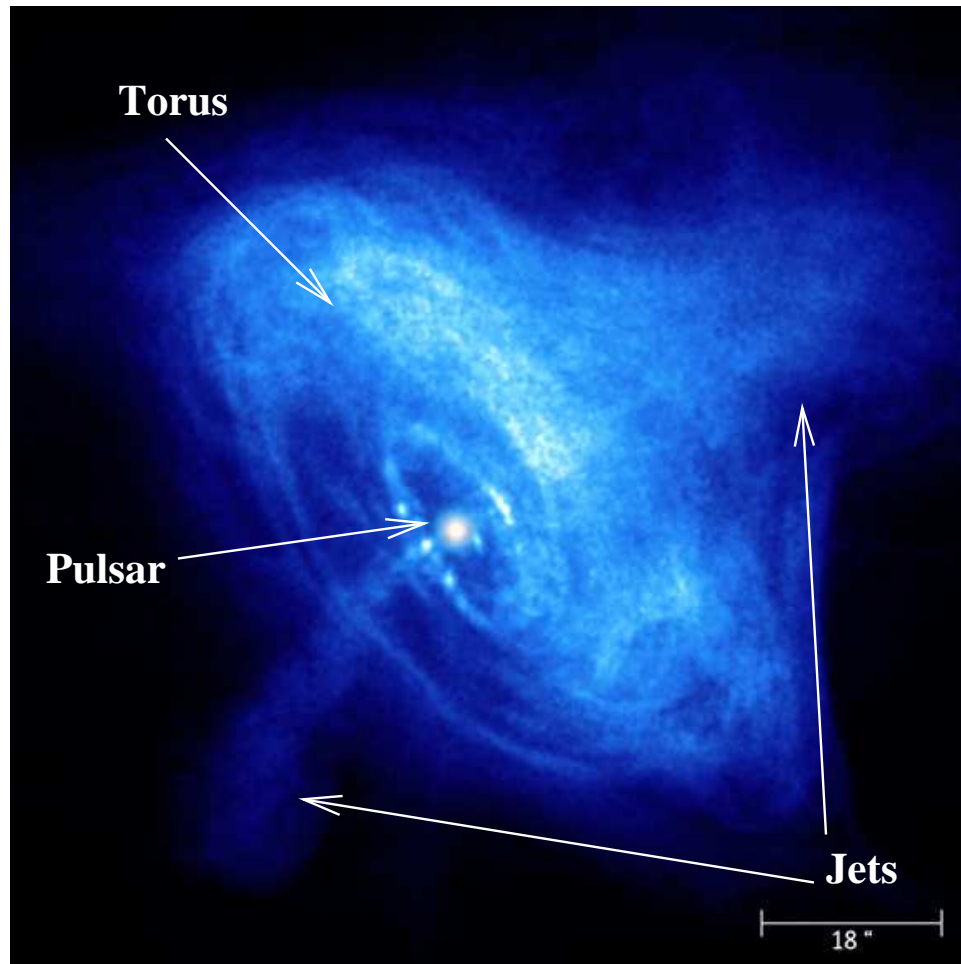


Figure 3. The region surrounding the Crab Pulsar imaged by the *Chandra X – ray Observatory*. Credit: NASA/CXC/ASU/J. Hester et al. 2002

1.3.2. *Overview of the Filaments*

The pulsar at the center of the Crab Nebula generates enough energy to dramatically affect the dynamics of the overall nebular system. This was first realized by Virginia Trimble in her groundbreaking paper “Motions and Structure of the Filamentary Envelope of the Crab Nebula” (Trimble 1968). The filaments Trimble describes are composed of stellar ejecta that literally lie on the surface of the synchrotron nebula and appear as long arc-like areas of concentrated optical line emission. The filaments are dense enough that all three emission lines can be found, although the line intensities can vary over very small scales. A figure that points out these features in the Crab Nebula is presented in Figure 4. The filaments have a cloud-like form in that they are large, bubble-like protrusions over the entire nebula (Hester 2008). Filaments that appear close to the center of the nebula have the same bubble-like structure as those filaments seen near the edge, but viewed at different angles. Radiation emitted by the filaments is thermal in origin with $T \approx 10,000$ K, (Sankrit et al. 1998). The proper motion of the filaments as they expand can be used to back-calculate an age for the remnant. Using several observations of the Crab over a total of 27 years, Trimble (1968) measured the proper motions of filaments and projected them back in time to determine both an approximate explosion center and an estimated age. Surprisingly, the data gave a convergence date of 1140 AD, or 86 years after the observed explosion. This difference indicates that the filaments are not expanding freely, as would be expected for ejecta in a typical Type II supernova remnant, but have been accelerated over time. The cause of this acceleration is ultimately the pulsar, via the

synchrotron nebula. The spin-down luminosity of the pulsar drives up the interior pressure of the synchrotron nebula, creating an outward force on the filaments and causing them to expand at a rate faster than the expected free expansion velocity (Trimble & Woltjer 1971).

Observations of the filaments show that where they exist they are in contact with the surface of synchrotron nebula, thereby almost completely surrounding the synchrotron nebula with a dense shell of ejecta. This confinement has the effect of slowing the expansion of the pulsar wind. The pulsar continually supplies energy to the synchrotron nebula, and the filamentary confinement of the relativistic wind ultimately increases the pressure in the interior part of the nebula. At some point in its evolution, the pressure in the synchrotron nebula had a large enough differential with the outside gas that a shockwave was released. This idea was first suggested by Chevalier (1977). Later, Sankrit & Hester (1997) used measured line intensities to show that the shock is not simply expanding into surrounding interstellar medium but rather is catching up with and propagating into freely expanding ejecta lying outside of the visible filaments. The model by Sankrit & Hester (1997) used a shock velocity with a speed equal to the estimated free expansion velocity of the ejecta (with an explosion date of 1054 AD) minus the expansion velocity of the synchrotron nebula and found that the model predicted line intensities that were quite similar to the spectroscopically measured line intensities of the filaments. They showed that photoionization of the filaments due to high energy photons from the synchrotron nebula could not produce the strengths of higher ionization lines that are observed in

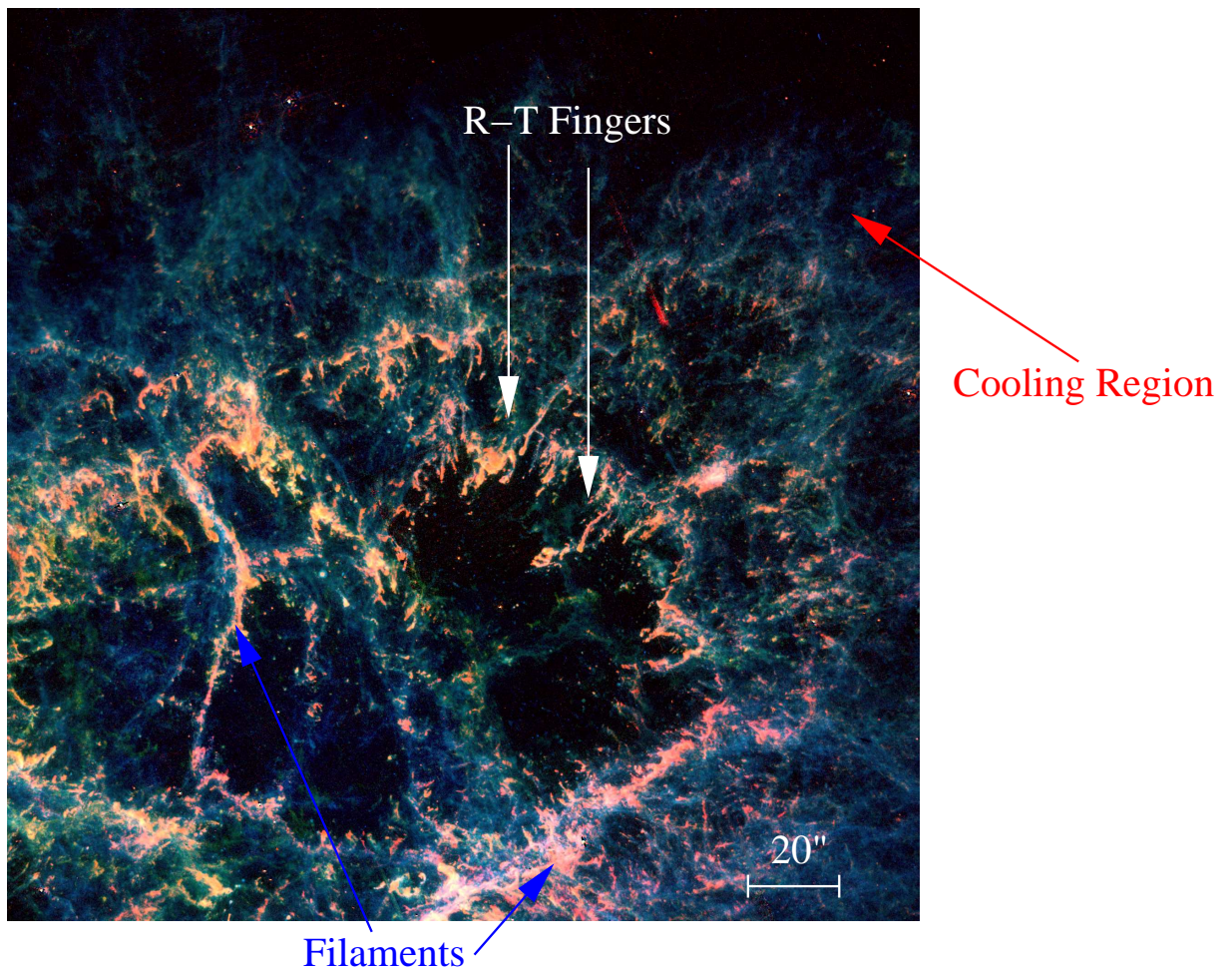


Figure 4. An image of the Crab Nebula with the filaments, R-T fingers, and cooling regions pointed out. Filaments appear as thin, arcuate, and connected emission. R-T fingers form from the filaments but protrude to the interior of the synchrotron nebula, and the cooling region behind the shock is visible via diffuse [O III] emission.

the Crab (Ne V, [O III], C IV). The temperatures of the filaments also suggest that they are heated by more than photoionization alone. Fesen & Kirshner (1982) used spectrophotometry and line ratios of a few filamentary positions to conclude that the [O III] line temperatures range between 11,000 to 18,300 K, [N II] temperatures have an upper limit of 13,600 K, [O II] temperatures range between 7700 and 16000 K, and [S II] temperatures are between 7500 and 13,000 K. The average electron density of the filaments inferred from [O II] to [S II] ratios is 1300 cm^{-3} , which is what would be expected from shocked gas that cools radiatively and compresses.

There have been many spectroscopic studies of the Crab Nebula that have led to clues about the filamentary composition. Many of the emission lines seen in the filaments are forbidden lines that are the result of magnetic dipole transitions with very low transition probabilities (10^{-4} s^{-1}). These lines are considered “forbidden” because of their very low probability rate and because they can never occur on Earth. Forbidden transitions can only occur in regions that are below a critical density, n_{crit} , defined as the electron density where the rate of spontaneous radiative decay equals the rate of collisional deexcitation for an excited state. When the density of electrons is $\leq n_{\text{crit}}$, the collision rate is so small that an atom may remain in an excited state for minutes or even hours before releasing a photon and going back to the ground state. As an example, the critical density of [O III] is $n_{\text{crit}} = 4.35 \times 10^3 \text{ cm}^{-3}$ and for [O I] is $n_{\text{crit}} = 3.14 \times 10^4 \text{ cm}^{-3}$ (Dopita & Sutherland 2003). We see both of these emission lines in the Crab Nebula filaments along with forbidden line emission from [S II], [O II], [Fe V], [N II], [Ar III], and others (Fesen & Kirshner 1982).

Spectroscopy of the Crab at optical and near-infrared wavelengths have led MacAlpine et al. (2007) to suggest that correlations between various emission lines at certain locations in the nebula can be used to determine the amount of nuclear processing that the filaments at that location have undergone. Filaments show a range of [N II] $\lambda 6583$ to [S II] $\lambda 6731$ line ratios, and MacAlpine et al. (2007) conclude that this is evidence of various levels of oxygen burning. The authors also suggest that the sulfur and argon leading to [S II] $\lambda 6731$ and [Ar III] $\lambda 7136$ emission were coproduced in the supernova because of their strong mutual spatial correlation in the nebula. Uomoto & MacAlpine (1987) found that a large filament crossing east to west across the face of the nebula has a He I $\lambda 5876/H\beta$ line ratio higher than the solar value and for this reason has been termed the high-helium torus (Woltjer 1958). This area may have a helium mass fraction of up to 95 % (MacAlpine et al. 2007). The overabundance of helium remains to be explained.

1.3.3. *Interaction of the Pulsar Wind and the Ejecta*

Jun (1998) modeled the interaction of the expanding, synchrotron bubble with the ejecta that is expanding freely from the supernova explosion. In this model, there are actually four shocks. There is the original blast wave that was produced when the core of the progenitor collapsed and rebounded, sending the outer layers of the star outward. This shock would currently be propagating at the location of the outermost ejecta and extends the farthest distance from the nebula. The model also includes the reverse shock that is moving inward toward the center of the nebula, produced by a pressure difference between the expanding ejecta and swept-up ISM. Neither of these

shocks are observed in the Crab; however, the densities and shock speeds that would be expected would produce emission that is below observational levels so they may be present but unobservable. In addition, since the Crab was a cavity explosion, we would not expect there to be any significant swept-up ISM at the location of the SN blastwave. The Jun (1998) model also includes a third shockwave that is caused from the expanding synchrotron nebula impinging on the backside of the ejecta and finally there is a wind-termination shock near the pulsar. Figure 5 shows these respective areas. The self-similar model of Jun (1998) concerned only the region between the contact discontinuity (at the synchrotron-filament boundary) and the location of the shock front, and a constant luminosity was assumed. They determined that if the ejecta has a power-law falloff in density, and the filaments cool adiabatically, then the filaments produced will be thicker, but if the post-shock gas can cool radiatively, then the filaments formed are thinner and denser. The models also showed that if the luminosity of the pulsar decreases in time, then the filamentary shell becomes thinner but the density is relatively unaffected. We describe the Jun (1998) model more completely in Chapter 5.

The model by Sankrit & Hester (1997) of the shock being driven by the synchrotron nebula into the freely expanding ejecta suggests that the shock is moving at speeds slow enough ($v_s \approx 150 \text{ km s}^{-1}$) that the post-shock gas may cool radiatively, mostly via forbidden transitions, within timescales smaller than the age of the Crab. The location of the post-shock cooling region is marked by the outer edge of high ionization emission, such as Ne V and [O III], and reaches distances of roughly 2 pc

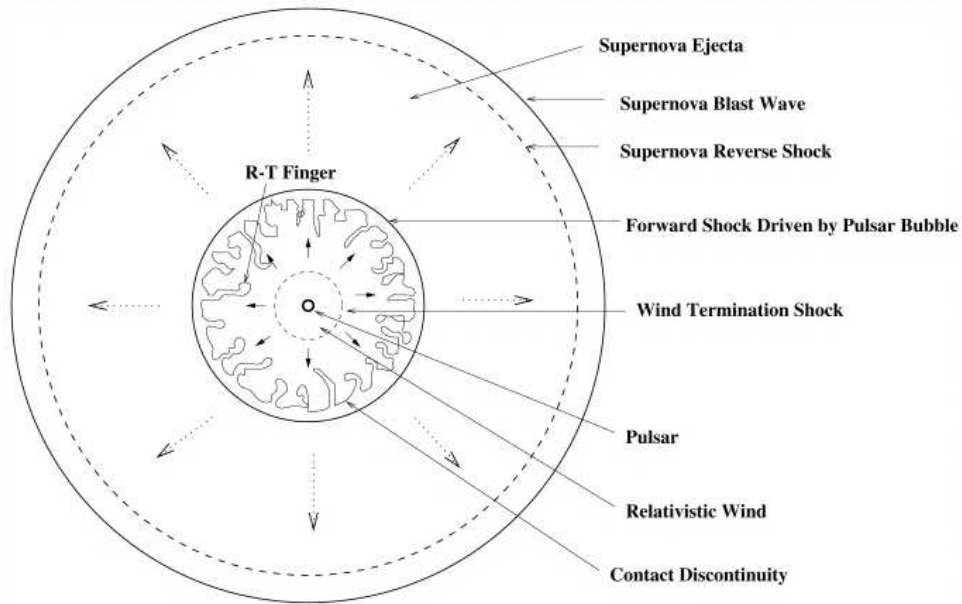


Figure 5. A schematic of the interaction of a Pulsar Wind Nebula with surrounding freely expanding ejecta. Figure taken from Jun (1998).

from the location of the pulsar along the long axis of the nebula on the sky.

Jun (1998) created a two-dimensional numerical simulation to determine how instabilities develop from the interaction of a pulsar wind nebula with the surrounding supernova ejecta. They found that only hundreds of years after the explosion, the expanding PWN begins to accelerate into the freely expanding ejecta and these simulations produced filamentary structures not unlike what are seen in the Crab Nebula *HST* observations. There is a large density contrast between the filaments [$\approx 10^3 \text{ cm}^{-3}$, Fesen & Kirshner (1982)] and the synchrotron nebula [$n \approx 1 \text{ cm}^{-3}$, Jun (1998)], marked by a contact discontinuity where the two media meet. The forced expansion of the synchrotron nebula generates an effective gravity vector pointing radially towards the position of the pulsar. All of these factors combined (the large density gradient between the relativistic plasma and the cooled ejecta with the ef-

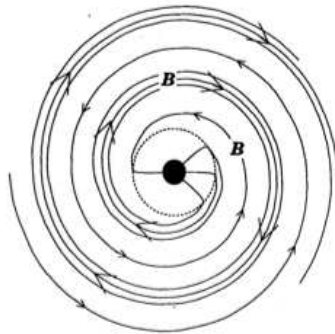
fective gravity caused by the expansion of the synchrotron nebula) have caused the contact between the synchrotron nebula and thermal ejecta to be subject to magnetic Rayleigh-Taylor (R-T) instabilities (Hester et al. 1996). R-T instabilities occur when a light material (synchrotron nebula) accelerates into a denser medium (filaments), like the heated wax inside of a lava lamp. The R-T fingers grow from the filaments, and are attached to the filaments at the contact discontinuity. R-T fingers have been noted in the filaments of the Crab Nebula for years (Hester et al. 1996) and the persistence of these fingers is due to the large density difference between the shocked ejecta and the relativistic pulsar wind. The filament thickness increases with time as the shock continues to accelerate and overrun more ejecta, and the R-T fingers grow as material from the filamentary shell is siphoned into them. The gas at the tips of the fingers, the rounded part that protrudes farthest into the synchrotron nebula, becomes compressed as more and more material flows into the finger, and the tips may reach densities ten times higher than the overlying filaments (Jun 1998). The results of the Jun (1998) model suggest that the R-T instability begins about 250 years after the explosion, based on their observed lengths and expansion velocities. They predict that the fingers have their highest growth rates about 1000 - 2000 years after the explosion, which is precisely the time frame in which we are viewing the Crab Nebula. 60 - 75% of the total shocked mass may be contained in the fingers, which are accelerating away from the pulsar, but at a rate slower than the shock speed. After about 2000 years, the Jun (1998) model predicts that the fingers will be fully developed and therefore the incoming mass from the shock will remain in the

outer filamentary shell.

The R-T fingers protrude into the synchrotron nebula and are surrounded by synchrotron radiation on all sides. The synchrotron nebula continues to expand around the fingers where the resistance is lower causing the wave-like appearance of filaments in between the R-T fingers. Sankrit et al. (1998) studied the photoionizational structure of long R-T fingers using *HST WFPC-2* data in seven line filters. The images showed that [OIII] is mostly diffuse and surrounds the outer part of the fingers. Lower ionization lines, such as [S II] and [O I], are contained in the dense cores of the R-T fingers where there is shielding from ionizing photons by the outer filamentary layers. Sankrit et al. (1998) created a photoionization model of the fingers that correctly predicted the line ratios of [O I], [O III], and [S II], strongly suggesting that the stratification seen in the R-T fingers is due to photoionization by extreme ultraviolet (EUV) photons originating from the synchrotron nebula and is not due to shock heating. It is important to realize that [O III] emission in the Crab is formed by both radiative cooling from behind the shock (found at the edges of the nebula) and also by photoionization from the synchrotron emission (at the contact discontinuity). [S II] may also be found due to both cooling behind the shock and photoionization. [O I], however, is only present due to shielding in the densest gas where the atoms are not subjected to ionizing extreme ultraviolet (EUV) radiation. (The gas behind the shock contains ionized oxygen; [O I] must have formed after the shocked ejecta cooled.)

1.3.4. *Magnetic Fields in the Crab Nebula*

Synchrotron radiation, such as that emitted in the synchrotron nebula in the Crab, is highly polarized because the radiation is emitted in the plane perpendicular to the magnetic field. *HST* ACS observations studying polarization in the Crab found that in some regions the polarization can have values of nearly 70% (Hester 2008). In order to produce enough energy to have synchrotron emission, Burbidge (1956) determined that there must be a very large magnetic field (10^{-2} to 10^{-3} G); the emission could not be explained as being due solely to gravitationally trapped magnetic flux associated with the progenitor. The theoretical explanation for the large magnetic field is that the rotation of the pulsar has wound up a poloidal field and amplified the toroidal field, resulting in a flow of magnetized plasma away from the pulsar (Piddington 1957). A schematic of the magnetic field geometry close to the pulsar is shown in Figure 6, both from a polar view and a side view. Because the polarization relies on an ordered field, one expects the polarization to be high near the pulsar and then break down as the magnetic plasma begins interacting with the filaments (Michel et al. 1991). Images taken by Michel et al. (1991) using the Wide-Field PFUEI CCD camera on the Palomar 1.5 meter telescope showed that the linear polarization is symmetrically centered on the pulsar. The linearly polarized emission has the shape of hourglass, which would be consistent with the radiation being preferentially emitted from the spin-equatorial zone of the pulsar (in the shape of a torus) and having the spin axis tilted approximately 30 degrees to our line of sight (Michel et al. 1991).

A**Polar View of a Partially Oblique Rotator**

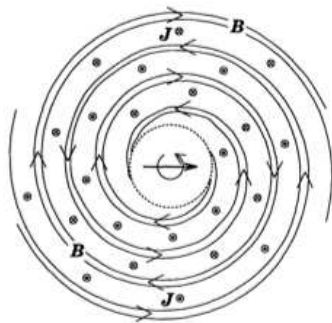
Geometry of the Magnetic Field

The view shows the field geometry in one hemisphere only.

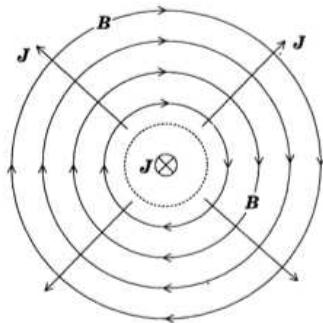
The sign of the DC field and polar current is reversed in the opposite hemisphere.

The sign of the AC fields and currents are the same in the opposite hemisphere.

The equatorial region is dominated by Coroniti's striped magnetic wind. The polar region is dominated by the Poynting flux from the rotating dipole.



The AC component of the B field and currents. Along the axis the circularly polarized Poynting flux from the rotating dipole dominates.



The DC component of the B field and current. B is azimuthal. J is in along the poles and out in the equatorial plane.

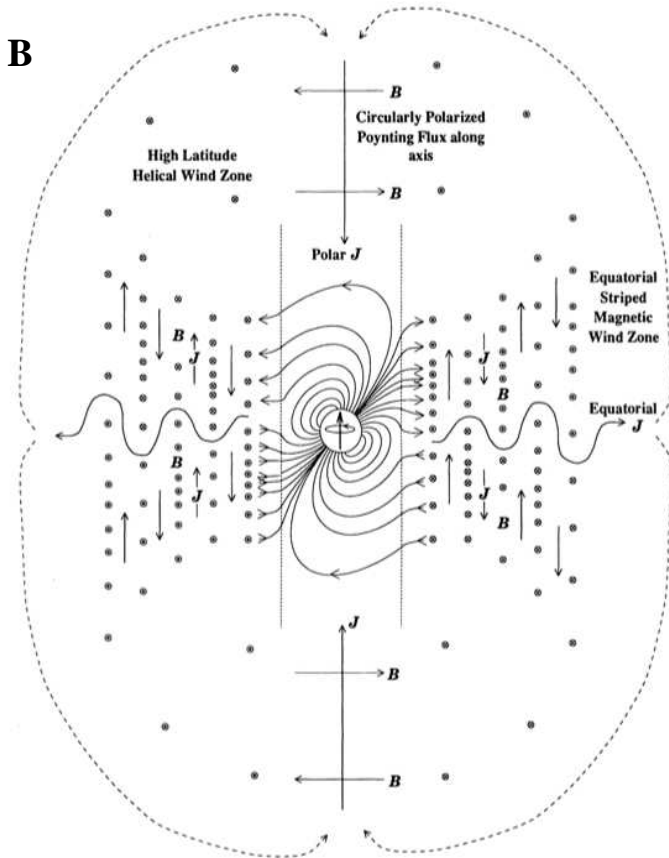
B

Figure 6. (A) Polar view of the magnetic field geometry of the pulsar wind in the oblique rotator model of a pulsar. (B) Side view of the magnetic field geometry of the pulsar wind in the oblique rotator model of a pulsar. Both figures taken from Hester et al. (1995).

When Michel et al. (1991) observed the Crab synchrotron nebula in totally unpolarized light, they found that the filaments impede the flow of the pulsar wind and cause the magnetic field lines to twist. Twisting the magnetic field lines twist has the effect of making the the synchrotron appear unpolarized because the electric field vector twists as well and the emission becomes circularly polarized.

Michel et al. (1991) estimated the time it would take for a magnetic field to penetrate a filament as $\tau = \mu_o \sigma L^2$, where $\mu_o = 4\pi \times 10^7$ is the permability of free space, σ is the conductivity and L is the length of a filament. Assuming that the filament has a length of $L \approx 10^{15}$ m and $\mu_o \approx \epsilon_o \omega_p$ where the collision rate is equal to the local plasma frequency ($\omega_p \approx 3 \times 10^6 \text{ sec}^{-1}$), then τ is nine orders of magnitude greater than the age of the remnant ($\tau \approx 10^{12}$ yr). This calculation strongly suggests that the magnetic field can not penetrate the filaments, and the filaments should be effectively superconducting. Resulting longitudinal currents in the filaments caused by the interaction with the magnetized plasma help to keep them intact and make them persistent structures in the nebula. The persistence of the filaments means that they continue to impede the expansion of the synchrotron nebula.

The magnetic tension in the filaments will keep the interface between the synchrotron nebula and filaments stable until the buoyancy forces are strong enough to overcome the magnetic tension. As discussed above, there are prominent R-T fingers observed in the Crab Nebula. In order for the R-T instability to take effect, the filaments must have enough mass to make the buoyancy force greater than the magnetic tension (Chandrasekhar 1961). The magnetic Lorentz force (per volume) is defined

as

$$\mathbf{F}_{\text{mag}} = \frac{\mathbf{j} \times \mathbf{B}}{c} = \frac{\nabla \times \mathbf{B} \times \mathbf{B}}{4\pi} \quad (1.4)$$

which can be separated into terms corresponding to magnetic pressure and the magnetic tension,

$$\mathbf{F}_{\text{mag}} = \nabla_{\perp} \left(\frac{B^2}{8\pi} \right) + \frac{(\mathbf{B} \cdot \nabla) \mathbf{B}}{4\pi}. \quad (1.5)$$

The second term describes the magnetic tension, and has magnitude equal to

$$\frac{B(\mathbf{B} \cdot \nabla)}{4\pi} \approx \frac{B^2}{4\pi R_c} \quad (1.6)$$

where R_c is the radius of curvature of a magnetic field line induced by a perturbation, which is approximately equal to the wavelength of the instability, λ . Therefore, the instability occurs when the magnetic tension force cannot compensate for the buoyancy force, or

$$\frac{B^2}{4\pi\lambda} < g_{\text{eff}}(\rho_{\text{ej}} - \rho_{\text{PWN}}) \quad (1.7)$$

where B is the magnetic field strength in the filaments, λ is the wavelength of the perturbation, and g_{eff} is the acceleration of the synchrotron nebula into the freely expanding ejecta. We can further this idea by recognizing that the density of the relativistic plasma, ρ_{PWN} is much less than the density of the shocked ejecta, ρ_{ej} , and then it becomes clear that the growth of R-T fingers requires that $\rho_{\text{ej}} \sim B^2/g\lambda$ (Hester et al. 1996). The critical wavelength for the onset of the R-T instability is

$$\lambda_{\text{crit}} = \frac{B^2}{4\pi\rho_{\text{ej}}g_{\text{eff}}}. \quad (1.8)$$

and the fastest growing wavelength of the instability is actually equal to twice that value (Hester et al. 1996). Equilibrium conditions imply that as the gas making up

an R-T finger cools, material is poured in from the outer filaments in order to keep the thermal pressure in balance with the effective gravity along magnetic field lines (Hester et al. 1996).

Hester et al. (1996) used numerical simulations of a magnetic R-T instability to show that the density of the skin determines the morphology of the interface. Low density skin ($\rho/\rho_{\text{crit}} < 1$) will remain stable at the interface, and progressively larger densities will lead to finger formation ($\rho/\rho_{\text{crit}} \approx 1$), and then secondary Kelvin-Helmholtz (K-H) instabilities (characterized by mushroom-shaped flattened tips and vortices) ($\rho/\rho_{\text{crit}} \gg 1$). More recent hydrodynamic models of the formation of R-T instabilities due to PWN expanding into supernova ejecta by Bucciantini et al. (2004) show that efficient radiative cooling is a critical component in the formation of fingers and therefore the fingers most likely formed shortly after the explosion when the nebula was much denser and cooled more quickly. They also determined that the Thin-Shell (TS) instability may be the dominant instability for large wavelength instabilities, or those perturbations that are on scales much larger than the shell thickness. The TS instability occurs when the skin thickness is much smaller than the curvature radius of the nebula and the skin is forced to bend due to density perturbations resulting in a wave-like appearance of the skin but no finger development. This may be the cause of the arcuate edges seen around most of the perimeter of the Crab if the instability occurred early in the expansion and then the shape has been retained throughout time. The scalloping has a scale of about $\theta = \pi/10$ (Hester 2008), based on roughly 20 bubble-like protrusions around the edge of the nebula.

Simulations show that perturbations with angular sizes greater than $\pi/6$ distort the entire shell which is characteristic of the TS instability. This bubbled morphology is likely present over the entire surface of the nebula. The brightest filaments are typically seen where bubbles meet, which may be where the gas is concentrated due to the TS instability. The smaller scale perturbations in the filaments, however, are due to R-T instabilities. Around $\pi/8$, the R-T instability becomes dominant and fingers develop, but the overall shell still shows TS curvature. The K-H instability does not come into effect until angular sizes smaller than $\pi/16$ because the growth rate increases for smaller wavelengths leading to more shear at the tip. When a magnetic field is introduced into the Bucciantini et al. (2004) models, the fingers grow more slowly and secondary K-H instabilities are suppressed. They also showed that once the system reaches equipartition between the magnetic and thermal pressure, growth of the finger stops. Hester et al. (1996) argue that the density of the gas at the contact-discontinuity is high enough that once an instability takes effect, the magnetic component of the instability can be neglected and the instability develops as it would in the non-magnetic case. The evidence for this are the examples of K-H instabilities and also regions where fingers have detach completely (despite the magnetic reconnection) leaving a sphere of dense gas within the synchrotron nebula [Hester et al. (1996), Blair et al. (1997)].

1.4. Dust in the Crab Nebula

Optical images of the synchrotron nebula have shown evidence of dust in the Crab Nebula. The first optical evidence of dust was by Woltjer and Véron-Cetty

(1987) via extinction of background synchrotron radiation in a continuum image. More extinction features have since been cited using narrow-band continuum filters and high-resolution, ground-based imaging (Fesen & Blair 1990; Hester et al. 1990). The Crab is not unique in this regard. Many young supernova remnants have been found to have an infrared excess consistent with thermal emission from dust (Merrill 1980; Dwek et al. 1983; Graham et al. 1983). In fact, the dust in the Crab was first detected in infrared by Marsden et al. (1984), who used IRAS data to show that the Crab Nebula IR spectrum at long wavelengths is dominated by dust with a temperature of 70 K. Recent Spitzer data of the Crab taken with MIPS at 24 and 70 μm showed an infrared excess across this region; however, these authors were uncertain if the excess was due to warm dust or line emission (Temim et al. 2006). Assuming a blackbody spectrum ($T \approx 70$ K), the dust would have a peak wavelength of about 40 μm . It is likely that the excess emission measured by the *Spitzer Space Telescope* is due to warm dust in the nebula, but that the peak dust emission is outside of the *Spitzer Space Telescope* bandpass. *HST* images near the center of the Crab show that most of the dust extinction features reside in concentrated areas that coincide with the cores of the filaments (Blair et al. 1997) and therefore correlate best with [O I] emitting gas. This is expected since both [O I] and dust can only exist in regions that are well shielded from synchrotron radiation. Fesen & Blair (1990) assumed a radii of dust grains around $a = 0.075\mu\text{m}$, consistent with presolar SiC grains, and a density of 2-3 g cm^{-3} to estimate that the Crab contains a dust mass of at least $2 \times 10^{-6}M_{\odot}$. They note that this is probably less than the true dust mass

because they were measuring extinction of synchrotron light and the observations couldn't detect extinction values less than 0.08 magnitudes.

There are two possible scenarios for the origin of dust in the Crab Nebula, both of which are still being debated and actively researched. Cernuschi, Marsicano, & Codina (1967) were the first to suggest that dust could condense from the supernova ejecta at a time shortly after the explosion when gas densities were very high. Wooden et al. (1993) combined airborne and groundbased infrared data of SN 1987A and found evidence that a minimum of $10^{-4} M_{\odot}$ of dust forms in the supernova ejecta within about 775 days after the explosion. In this scenario, the dust would have been swept up along with the ejecta as the synchrotron nebula expanded outward (Cernuschi, Marsicano, & Codina 1967). Another possibility is that the dust is actively forming in the relatively dense filaments and R-T fingers as the densities climb and temperatures drop and the conditions necessary for dust to aggregate are achieved.

The filamentary densities have proven to reach values much higher than originally thought. Graham et al. (1990) discovered two locations in the Crab filaments that showed infrared H_2 emission. The presence of molecular hydrogen was quite unexpected considering the high-energy environment and the low dissociation energy of H_2 (4.6 eV); however, Graham et al. (1990) found that a column density, N , of $\approx 10^{19} \text{ cm}^{-2}$ is sufficient enough to shield the molecule from photoionizing photons over the life of the remnant. Graham et al. (1990) argue that the molecule must have formed early in the expansion of the nebula when densities were higher, because

the densities in the filaments are currently too low for such a fragile molecule to be forming. The tips of R-T fingers have widths between about 0.8 - 1.5'' ($1'' = 3 \times 10^{16}$ cm at $d = 2$ kpc). Using the value of the column density above and $N = n_{H_2}R$ where R is the radius of the tip of the finger, then the number density of molecular hydrogen can be estimated to be between 440 - 830 cm^{-3} . This corresponds to an actual density of between $1.5 - 2.8 \times 10^{-21}$ g cm^{-3} . Assuming that the tips of R-T fingers are spherical, then the mass contained within them is about $1-3 \times 10^{-5} M_{\odot}$.

1.5. Overview of this Dissertation

Clearly the Crab Nebula is an extremely dynamical system. From the powerful pulsar, to the synchrotron nebula, the filaments, and ejecta beyond, the pieces of this nebula are all physically intertwined to form the nebula that we see. This dissertation presents new observations that are the highest resolution images of the Crab Nebula to date. They provide the best observational data set available to test the hypotheses presented in this dissertation and allow us to test a numerical model of the interactions between PWN and freely expanding ejecta.

Chapter 2 of this dissertation presents the first *HST* images to cover the entire nebula in three emission lines ([O III], [S II], and [O I]) and show the same region in the continuum. Using this range of emission lines allows us to study high, intermediate, and low ionization states respectively. The F547M (continuum) mosaic complements the line emission by indicating the physical bounds of the contact discontinuity and showing locations where dust is present in the nebula, seen by extinction in the continuum light.

Chapter 3 will discuss how we used the *HST* observations of [O III] presented here in conjunction with *VLA* observations by Bietenholz & Kronberg (1990) and Fabry-Perot analysis by Lawrence et al. (1995) to model the three dimensional structure of the Crab Nebula. This information was used to measure the distance of the shock from both the pulsar and expansion (or explosion) center, defined as the place in space the filaments project to if projected backwards in time. We find that the synchrotron nebula has expanded farther from the expansion center in the northwest side of the nebula and we use this result to provide evidence that the pre-shock ejecta density, or the density of the ejecta that lies outside of the perimeter of the current shock location, varies around the nebula. Specifically, we suggest that in the northwest (NW) region of the nebula the pre-shock ejecta density is lowest.

In Chapter 4 of this dissertation, we suggest that the shock in the northwest (NW) side of the remnant is moving faster than the shock in the SE which has caused an asymmetry in the morphological and physical properties of the filaments. This is a direct result of the differing pre-shock ejecta densities because when the pre-shock density is lower, the shock will propagate faster. Our data indicate that the shock is non-radiative in the northwest region and radiative around the other two-thirds of the nebula. In the southeast, the shock may be making the transition from radiative to non-radiative. Observationally this is shown by the NW gas showing higher ionization states, thicker cooling regions, and a lack of an [O III] boundary and disconnected filaments. We use the *HST* line images to measure line intensities of the gases and also to measure the thickness of the actual filamentary boundary.

In Chapter 5, we discuss the theoretical model by Jun (1998) describing the interaction between a PWN and freely expanding ejecta. We use his results and apply them to more accurately represent the dynamics taking place in the Crab Nebula, namely the transverse velocity of the pulsar and the distribution of the ejecta around the explosion center, to predict the NW-SE asymmetry we see in the shock speeds, the ionization structure of the filaments, and the development of R-T fingers. We use this model, in conjunction with results from the shock model by Sankrit & Hester (1997), to show that the R-T fingers likely began growing earlier in the NW than they did in the SE and therefore the fingers are longer there. We are able to use these results to predict the future evolution of the filaments.

In Chapter 6 we discuss a NW-SE asymmetry in the lengths and ionization structure of R-T fingers. Line intensities of the fingers were used to study the ionization structure and densities. We measured the lengths of R-T fingers in the NW and SE and find that the fingers in the NW are more than 2-3 times longer than they are in the SE. The instability is much more active in the SE and we suggest this is due to the contact-discontinuity only recently becoming accelerated and the dominant wavelength has yet to be established. The tips of R-T fingers show 3-4 times the line intensities that we see in the SE, indicating higher densities. These results are indicative of the ages of the fingers; NW fingers are older and have had more time to grow and collect gas at the tips.

Chapter 7 discusses the correlation of dust and low-ionization line emission in the Crab Nebula. We incorporated Fabry-Perot data to determine which filaments

are on the front side of the nebula, and we found that everywhere that we could constrain [O I] emission to be on the front side of the nebula, there was also some level of extinction due to dust. This indicates that the dust and gas are well-mixed and that the dust likely formed soon after the supernova explosion. For several dust absorption features, we calculated the most accurate gas-to-dust ratios for the nebula and found that the ratio is between 0.050-0.100. This value is more than 5 times higher than what is found in typical ISM (and much higher than the region surrounding the nebula), meaning that the dust we see was likely created in the explosion. This has important implications to astronomers studying how Type II supernovae may enrich the universe with dust.

Chapter 8 presents the conclusions of the dissertation as well as future research that would complement this work.

CHAPTER 2

HST WFPC-2 OBSERVATIONS OF THE CRAB NEBULA

2.1. Data Reduction

We present here the results of the first *HST Wide Field and Planetary Camera - 2* (WFPC-2) dataset to cover the entire Crab Nebula. The survey includes eight WFPC-2 fields. Each field is imaged in the following filters: F502N ([O III]), F673N ([S II]), F631N ([O I]) and F547M (a filter admitting a relatively line-free continuum). The images were collected between October 1999 and January 2002. The [O III] images were exposed for 2600 seconds, the [O I] images were exposed for 1300 seconds, the [S II] images were exposed for 1300 seconds and finally the F547M images were exposed for 900 seconds. These exposure times were determined based on the emission properties in the nebula for each emission line. The exposure times, dates, and locations are presented in Table 1, and the orientations of the pointings are indicated in Figure 7.

Table 1
Exposure Dates and Pointing Information for *HST*
Observations

Exposure ID (U5D10)	Field	Narrow-band Filter	Date (UT)	RA ($^{\circ}$ ' " (J2000))	Dec ($^{\circ}$ ' " (J2000))
101R	1	Cont	27 Jan 2000	05 34 23.24	+22 00 06.17
102R, 103R, 104R		[O I]			
105R, 106R		[O III]			
107R, 108R		[S II]			
201R	2	Cont	26 Jan 2000	05 34 25.44	+22 02 34.27
202R, 203R, 204R		[O I]			
205R, 206R		[O III]			
207R, 208R		[S II]			
301R	3	Cont	24 Oct 1999	05 34 28.99	+21 59 48.08
302R, 303R, 304R		[O I]			
305R, 306R		[O III]			
307R, 308R		[S II]			
401R	4	Cont	3 Dec 2000	05 34 30.97	+22 02 11.34

Continued on next page...

Table 1 – Continued

Exposure ID (U5D10)	Field	Narrow-band Filter	Date (UT)	RA ($^{\circ}$ '''(J2000))	Dec ($^{\circ}$ '''(J2000))
402R, 403R, 404R		[O I]			
405R, 406R		[O III]			
407R, 408R		[S II]			
501R	5	Cont	28 Jan 2000	05 34 40.31	+22 01 13.07
502R, 503R, 504R		[O I]			
505R, 506R		[O III]			
507R, 508R		[S II]			
601R	6	Cont	29 Jan 2000	05 34 38.46	+21 58 54.65
602R, 603R, 604R		[O I]			
605R, 606R		[O III]			
607R, 608R		[S II]			
701R	7	Cont	11 Oct 1999	05 34 42.83	+21 59 42.99
702R, 703R, 704R		[O I]			
705R, 706R		[O III]			
707R, 708R		[S II]			
801R	8	Cont	9 Jan 2002	05 34 35.15	+22 03 50.92
802R, 803R, 804R		[O I]			
805R, 806R		[O III]			
807R, 808R		[S II]			

Each of the *HST* *WFPC-2* fields consist of four separate Charge Coupled Device (CCD) chips. Three of the chips (CCDs 1-3) are *Wide Field Cameras* (*WFC*) and chip 4 is a *Planetary Camera* (*PC*). All of the CCDs are 800×800 pixels. The resolution of each *WFC* is $0.1''$ per pixel. The Crab Nebula lies at a distance of roughly 2 kpc (Trimble 1968), meaning one pixel in a *WFC* corresponds to 3×10^{16} cm. The *PC* is built for a higher resolution, with roughly twice the resolution of the *WFC*s but a smaller field of view. The difference in resolution between the *WFC*s and the *PC* causes a *WFPC-2* field to have a step-like appearance, with the smaller *PC* in the upper right quadrant and the *WFC*s surrounding it.

The data set presented here covers the entire Crab Nebula and consists of eight *HST* “fields”, or *WFPC-2* pointings. Each individual CCD was normalized

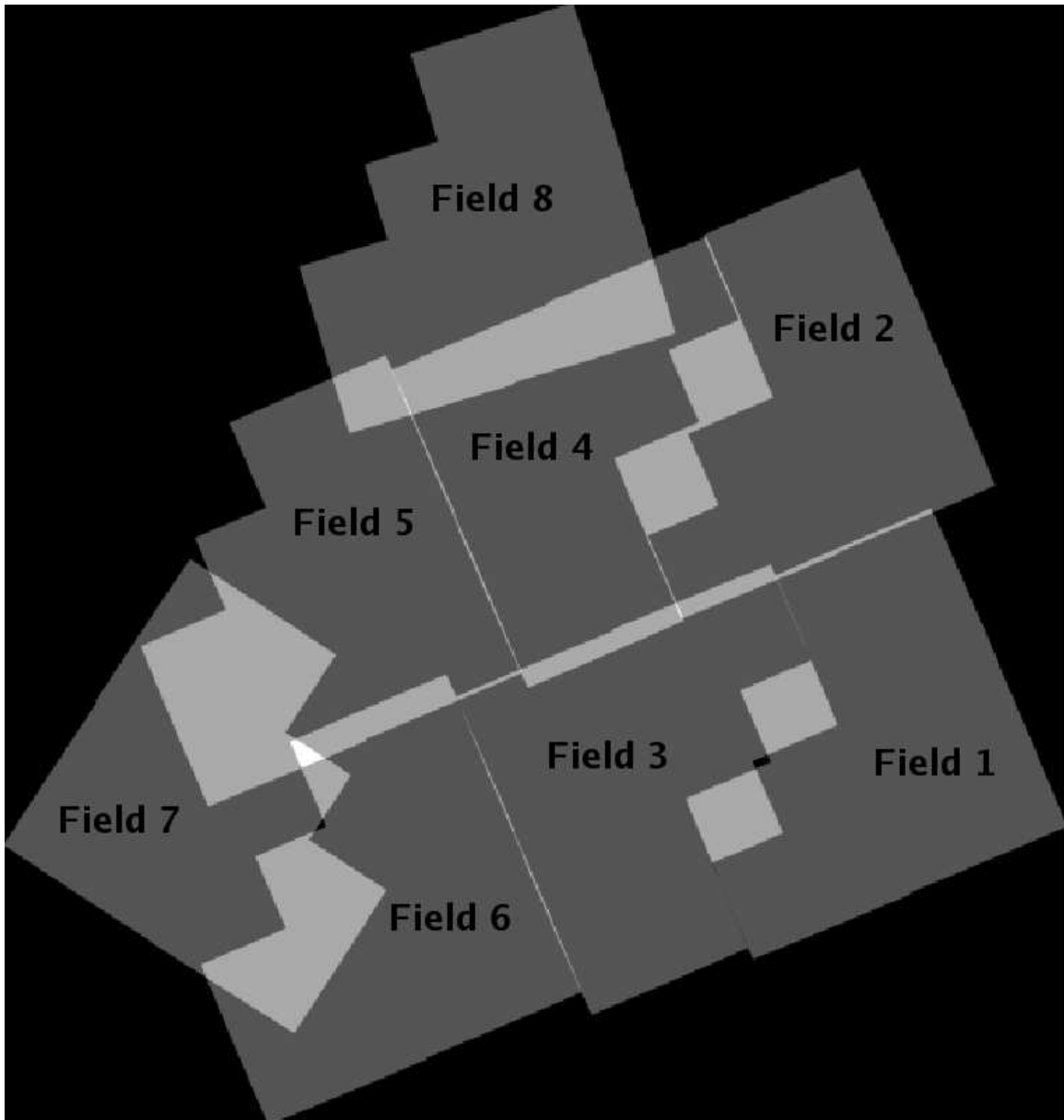


Figure 7. Locations of the eight *HST* *WFPC-2* pointings. North is up and East is to the left.

with a mask taken from the *HST* data archives by dividing the appropriate mask for a given filter from the corresponding line image. The data came independently from each CCD chip. We assembled each field mosaic using an algorithm written using the program Interactive Data Language (IDL) created by ITT Visual Information Solutions. The fields were observed twice in the [O III] and [S II] filters, three times for the [O I] filter and once for the F547M filter. The emission lines ([O III], [S II], and [O I]) were observed multiple times for the purpose of removing cosmic ray contamination from the images. To do this, the duplicate field observations of a line image were overlaid and an algorithm was developed to search for and remove bright, linear groups of pixels that were present in one of the images but not present in the other observation(s). This procedure worked well because cosmic rays occur randomly in the observations. Duplicate sets of the line images were then co-added to increase the signal-to-noise ratio. The fields did contain “seams” where the chips joined together, and the seams were more pronounced in fields where the intensity of the line emission was low. We attempted to reduce the appearance of seams by linearly interpolating across the seams. The success of this technique was dependent on the signal-to-noise ratio in those fields because regions of higher signal-to-noise resulted in much better interpolation. This procedure was completed independently for each of the eight fields, and for each line filter to ensure the best results.

There were not multiple images taken of the F547M (continuum) data set. For these images, cosmic rays were removed by flagging pixels with intensities higher than 2.5σ and replacing those pixels with the average of surrounding pixels. This technique

worked quite well because the continuum images have a much higher signal-to-noise ratio, and therefore have less random noise and smoother data than the emission line images. The seams between the WFCs and the PC of the continuum image were corrected with linear interpolation in exactly the same way as the line images were.

2.2. Creating *HST* mosaics

A mosaic of all eight *HST* fields was made for each emission line ([O III], [S II], [O I] and the Continuum) using algorithms we created just for this purpose. First, it was essential that the stellar astrometry was correct. For the astronomical alignment, we incorporated a visible image of the Crab Nebula taken with the Very Large Telescope (*VLT*) available in the *European Southern Observatory (ESO)* archives under program ID 60.A.9203(C). Astrometry information on seventy-three stars that were in the field of view of the *VLT* image and which had accurate positions listed in the *General Star Catalog II (GSC2)* were used to apply a linear and rotational transformation to the *VLT* image using the IDL routine *xfitgsc2*.

Next we aligned each *HST* field to the astrometrically correct *VLT* image. We measured the (x, y) coordinates of every star that was present in both the *HST* field and the *VLT* images so that a linear fit could be applied to the *HST* field that would match the header to the *VLT* astrometry. The transformations were checked by looking at a subtracted image (*VLT* - *HST*) to see if the stars in fact aligned properly. In each case, both the data field and a data field mask were transformed in order to keep track of regions with overlap and each mask was smoothed using a gaussian smoothing procedure to decrease the appearance of sharp edges. One by one,

each successive *HST* field was added in until all eight fields were included. Finally, the stacked emission line (or continuum) mosaic was divided by the stacked mask mosaic to properly weight areas of overlap. The values of the transformations used in each *HST* field are presented in Table 2.

Table 2
Fits used to align the *HST* Observations

Field	Filter	dx (pixels)	dy (pixels)	dR (pixels)	theta ($^{\circ}$)	rchi
1	F547M	-25.4222	5.79826	1.00005	-0.00112042	0.308042
	F631N	-25.6150	7.13816	0.999999	0.0188366	0.270935
	F502N	-25.5185	6.13138	1.00002	0.00127465	0.207225
	F673N	-25.3604	5.38047	1.00006	-0.00353599	0.371403
2	F547M	-21.0626	-6.87171	1.00076	-0.000497344	0.168330
	F631N	-21.0626	-6.87171	1.00076	-0.000497344	0.168330
	F502N	-21.5233	-6.67641	1.00079	0.00237607	0.273781
	F673N	-21.3230	-7.28130	1.00085	-0.00123992	0.188801
3	F547M	-14.9005	-7.58312	0.999442	0.00391050	0.522818
	F631N	-14.6157	-7.32522	0.999317	0.00389479	0.354328
	F502N	-14.3947	-7.52938	0.999292	0.00106632	0.127052
	F673N	-15.0036	-7.75843	0.999483	0.00247943	0.293447
4	F547M	-14.3583	-10.9227	1.00025	-0.00230865	0.476596
	F631N	-14.4408	-10.9570	1.00027	-0.000793122	0.220157

	F502N	-14.4612	-11.0531	1.00031	-0.00145990	0.275079
	F673N	-14.5372	-11.1224	1.00033	-0.00154471	0.282567
5	F547M	-9.06041	-5.68388	1.00064	-0.000112753	0.343574
	F631N	-7.65804	-5.62538	1.00035	-0.0112372	0.641944
	F502N	-7.06882	-5.56199	1.00020	-0.0297282	0.355247
	F673N	-9.10859	-5.89025	1.00071	-0.000877149	0.139145
6	F547M	-14.4258	3.50343	1.00201	-0.0269640	0.794560
	F631N	-14.4377	3.40869	1.00204	-0.0274242	0.182992
	F502N	-14.4704	3.14098	1.00206	-0.0361875	0.367727
	F673N	-14.5016	3.48505	1.00204	-0.0265286	0.254924
7	F547M	-6.42050	-6.10033	1.00076	0.0967548	0.914392
	F631N	-6.11038	-5.75644	1.00056	0.0956320	0.161156
	F502N	-6.17022	-5.74550	1.00061	0.0937959	0.131925
	F673N	-6.21676	-5.88723	1.00069	0.0928345	0.154974
8	F547M	-11.0217	-4.79788	0.999653	0.00159454	0.643221
	F631N	-10.9154	-5.18017	0.999709	-0.000852699	0.219690
	F502N	-10.9950	-4.64700	0.999609	0.00116701	0.220980
	F673N	-11.4531	-4.65083	0.999662	0.00357632	0.324711

The *HST* fields that cover regions outside of the nebula (that we will refer to as the “sky background”) all had minor differences in the pixel values. These regions should have very close to the same value since there is no signal being emitted this

area except the background noise; however the *HST* observations were completed over a period of two years and therefore had measureable differences. To correct for these Digital Charge (DC) offsets between different *HST* observations, we randomly choose field five (Figure 7) to represent the standard simply because this field contained a large amount of sky to use for background scaling and also overlaps three other fields. Because the *PC* and *WFCs* have different resolutions, they were scaled independently to apply the best corrections. We began re-creating the eight-field mosaic by aligning the fields together one by one with only the *WFCs* (the *PC* was masked out). Over regions of overlap, typically in an area where there was no line emission (just outside of the nebula) the intensity was measured from one field to the other field. When the scaling could not be made in an area with no line emission, a region with the least amount of emission was chosen. A linear scaling was determined that would make the data vary smoothly from one field to the next. Once the eight *WFCs* fields were all scaled and represented in the mosaic, individual *PC* chips were included using an identical method. This procedure was followed independently for each emission line filter and for the continuum filter.

The mosaics presented in this dissertation have been recreated using all of the transformations and DC corrections discussed above such that there is only one re-sampling of the data. This was done by creating an algorithm that placed each *WFPC-2* chip into the correct position in the mosaic independently and mapping the x,y locations of each pixel in the chip before and after placing it in the mosaic. Each transformation was done for the chip itself, a map of the x coordinates, a map

of y coordinates, and a mask. As before, the mosaic was built up, adding piece by piece. In areas where the seams between chips were visible or there was not complete overlap, data from the final, re-sampled mosaic discussed above was inserted. It should be noted that the continuum filter was scaled by eye and subtracted from the line images to provide the best possible image of just the emission line being observed. There is still continuum emission present, however, in the line images. Each of the three emission line mosaics and the continuum mosaic are shown in Figures 8, 9 10, and 11 representing [O I], [S II],[O III] and the continuum respectively. A colored combination of all four filters is shown in Figure 12, where red is the continuum, green is [SII] + [O I], and blue is [O III]. In all of the mosaics, north is up and east is to the left.

Narrowband line filters, like those used in these observations, are not ideal for observing the Crab Nebula because the ejecta is moving at speeds up to 1500 km s^{-1} (Trimble 1968) and emission at these velocities is doppler-shifted outside the *HST* filter bandpass. Due to this limitation, the emission lines are best sampled near the edge of the nebula where the motion is tangential to our field of view. Near the center of the nebula where the ejecta has the highest radial velocity, the line emission can be shifted well outside of the Full-Width Half Maximum (FWHM) of the filter bandpass. One must keep in mind that across the face of the nebula where radial velocities are largest there is line emission that is not represented in the *HST* mosaics. Table 3 shows the filter limitations as a function of velocity.

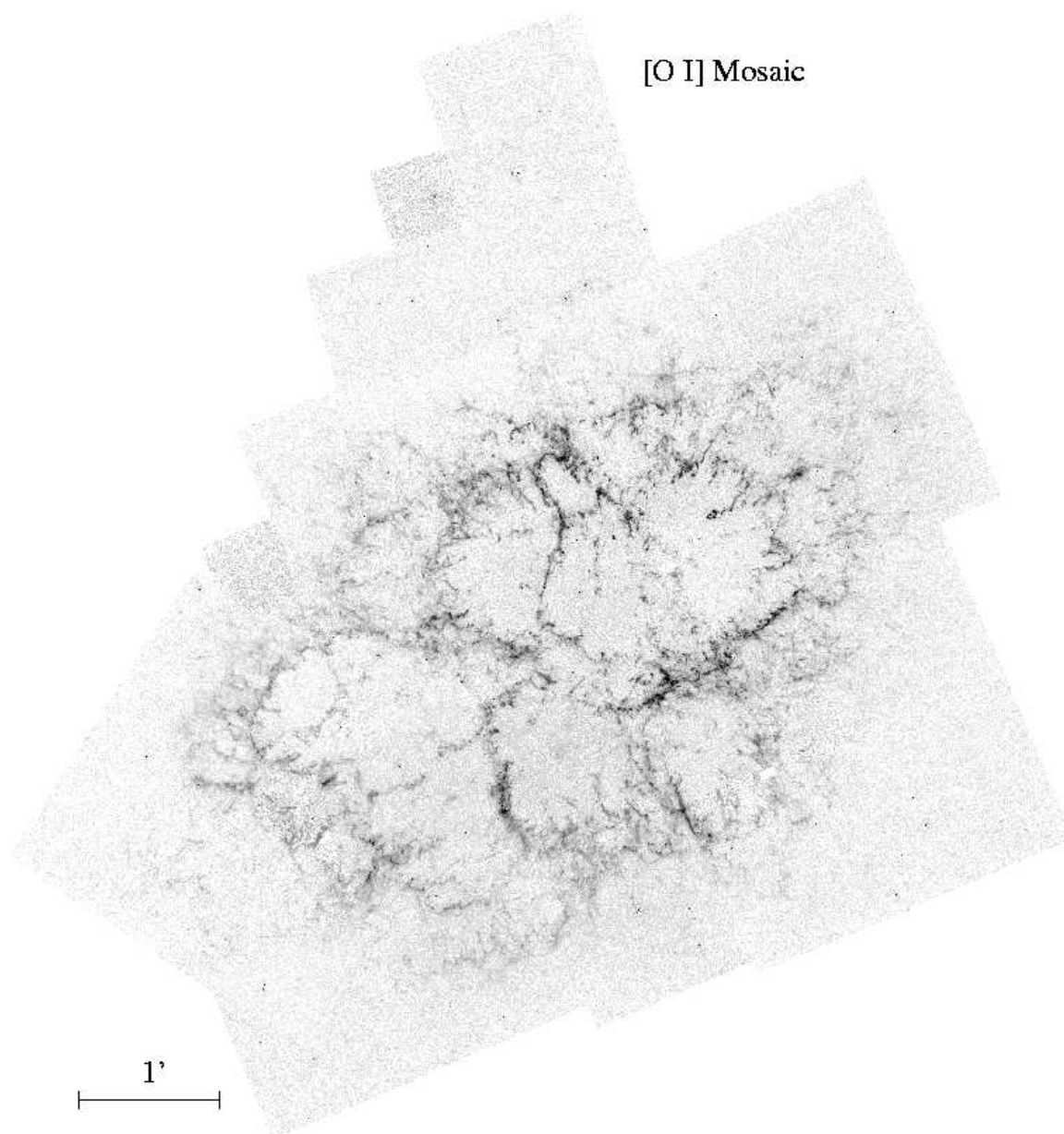


Figure 8. The [O I] *HST* mosaic. North is up and East is to the left.

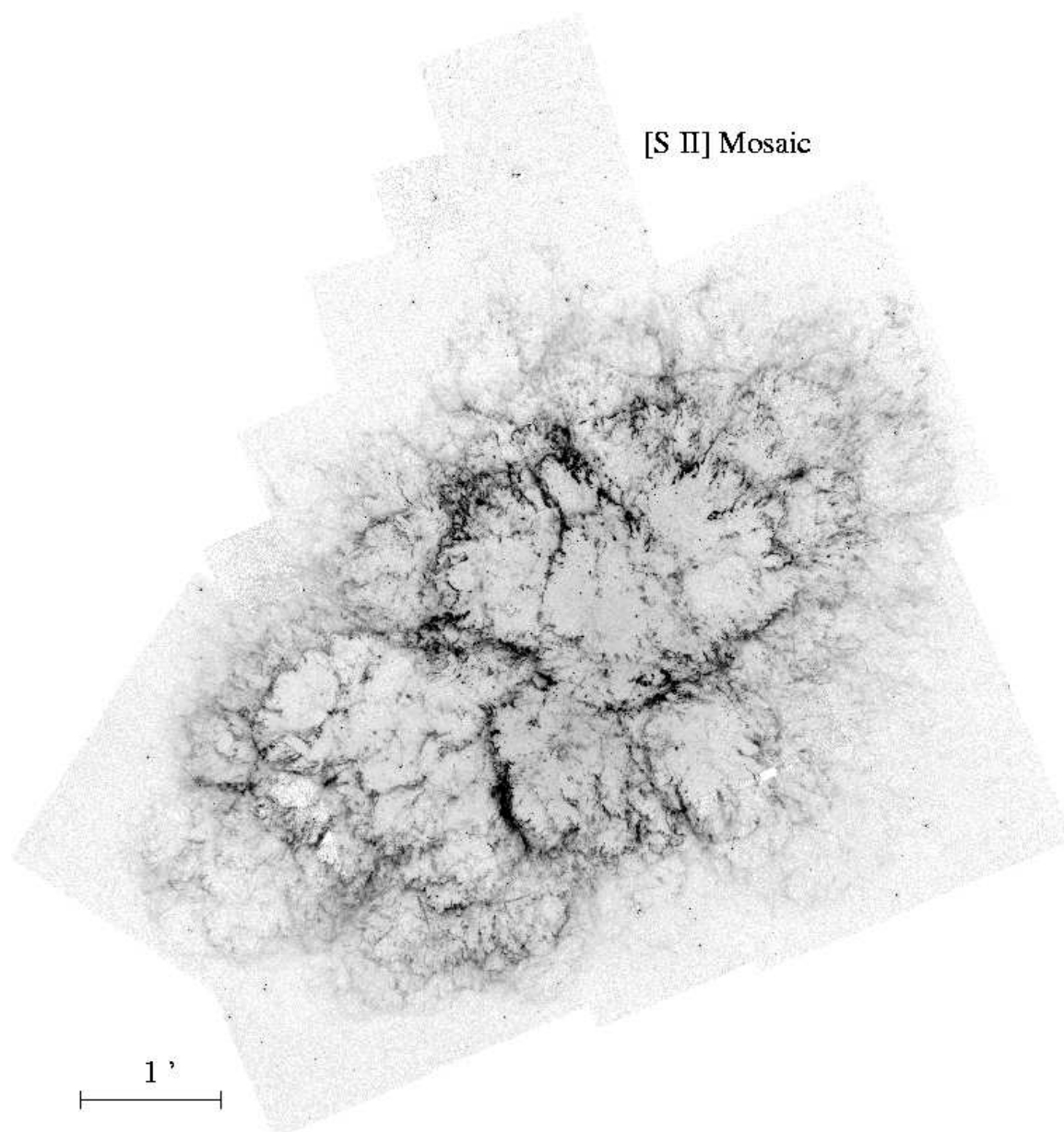


Figure 9. The [S II] *HST* mosaic. North is up and East is to the left.

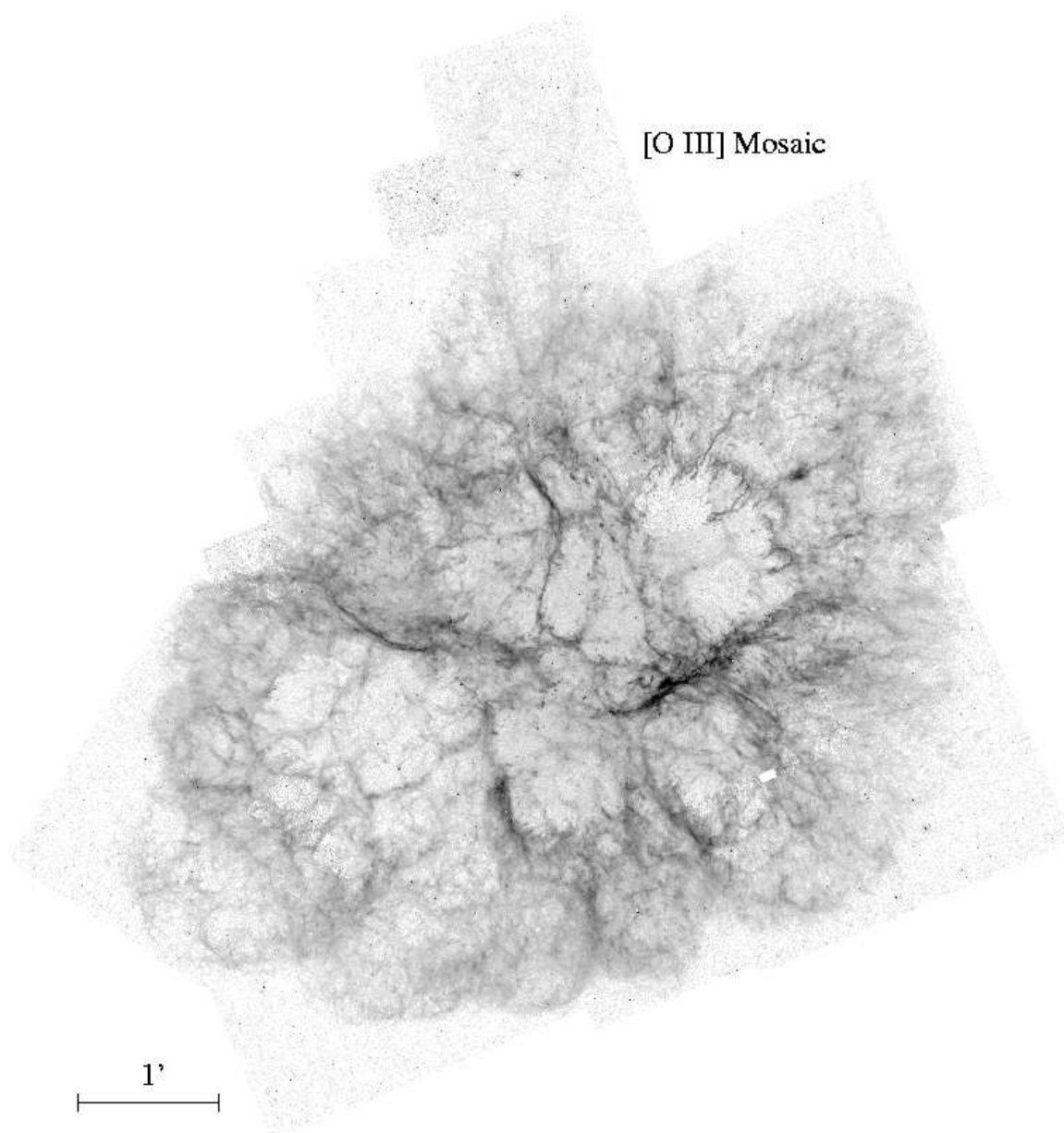


Figure 10. The [O III] *HST* mosaic. North is up and East is to the left.

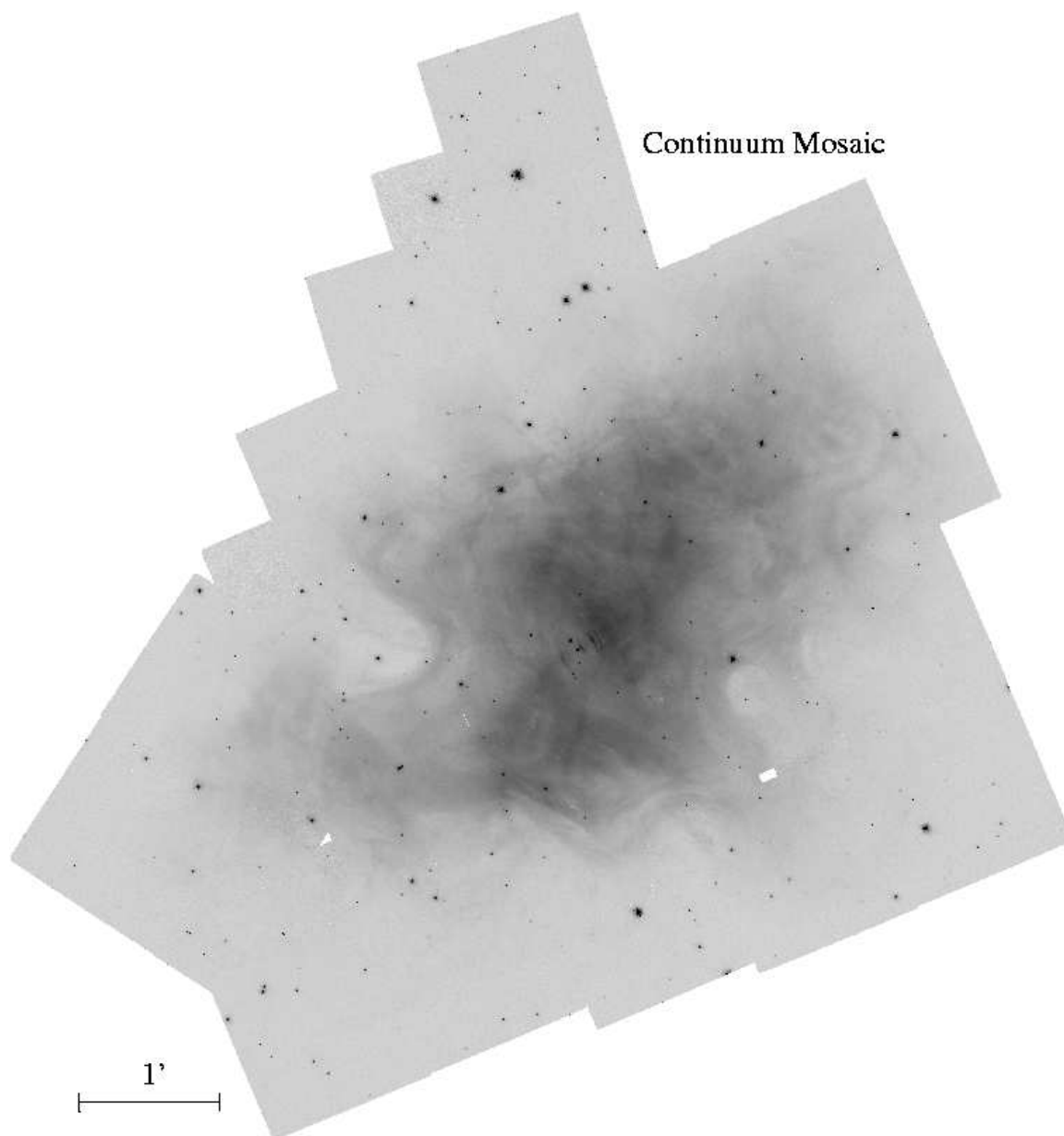


Figure 11. The Continuum *HST* mosaic. North is up and East is to the left.

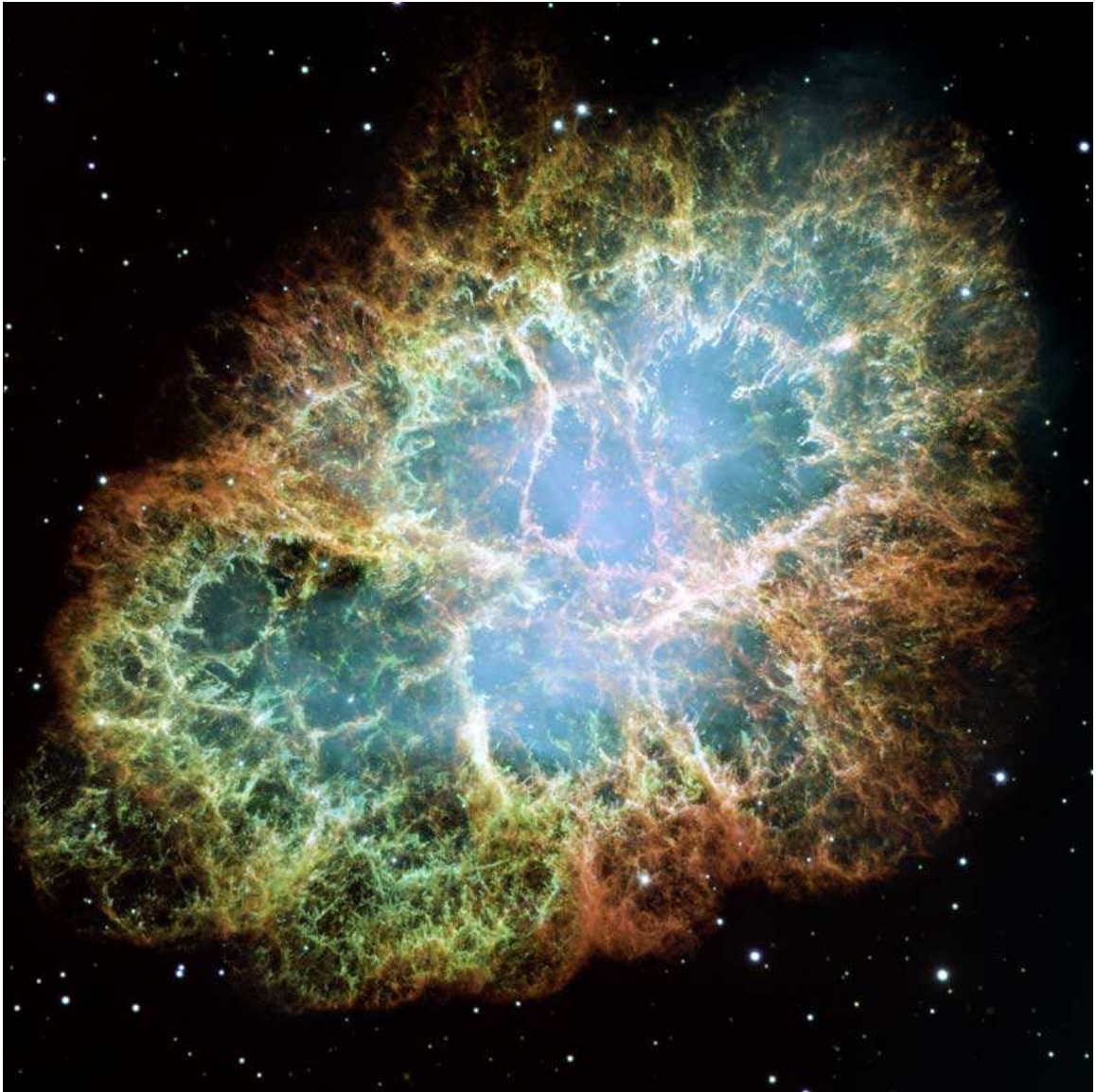


Figure 12. The composite of all four *HST* filter *WFPC*-2 mosaics of the Crab Nebula. [O III] $\lambda 5007$ is shown in red, [S II] $\lambda\lambda 6717,6731$ in green, and the [O I] $\lambda 6300$ and continuum are blue. North is up and East is to the left.

Table 3
HST Filter bandpass properties

Filter	$\Delta\lambda$	Line ID	Velocity Range
	\AA		(km s^{-1})
F673N	6709-6756	[S II] $\lambda 6717$	-306 to +1740
		[S II] $\lambda 6731$	-980 to +1110
F502N	4999-5026	[O III] $\lambda 5007$	-480 to +1140
F631N	6291-6321	[O I] $\lambda 6300$	-429 to +1000

The *HST* mosaics were converted to flux values in units of $\text{erg cm}^{-2} \text{s}^{-1} \text{\AA}^{-1}$ by using the pipeline calibration in the *HST* manual ($F_\lambda = (\text{PHOTFLAM})(\text{DN})(t_{\text{exp}}^{-1})$, where PHOTFLAM is taken from the *HST* image header, DN is the data number of a given pixel, and t_{exp} is the time of exposure). Since field 5 was chosen as the standard for all of the mosaics, the relevant values for this field were used. A value of 0.5363 was added to the [O III] image to normalize the flux of the sky background to what is measured in the [S II] and [O I] image. As an example, for the [O III] image we used $\text{PHOTFLAM} = 3.01015 \times 10^{-16} \text{ erg cm}^{-2} \text{s}^{-1} \text{\AA}^{-1}$ and an exposure time of 2600 seconds. After the flux conversion was applied, $\Delta\lambda$ (the wavelength range of the filter coverage, 4999-5026 \AA for [O III]) was multiplied by the image to give pixel values in units of $\text{erg cm}^{-2} \text{s}^{-1}$. The same procedure was followed for the other two line images.

Table 4
 Comparison of Fluxes Between Calibrated *HST* Images
 and Observed Spectra

Position	$f_{HST}[O\ I]$	$f_{GB}[O\ I]$	$f_{HST}[S\ II]$	$f_{GB}[S\ II]$	$f_{HST}[O\ III]$	$f_{GB}[O\ III]$
1	1.39	1.2 ± 0.37	5.48	9.5 ± 1.9	3.88	27 ± 5.4
2	1.21	0.77 ± 0.23	10.5	11 ± 2.2	9.48	11 ± 2.3
3	1.05	0.94 ± 0.28	5.15	4.8 ± 0.95	2.76	3.1 ± 0.62
4	1.19	0.84 ± 0.25	7.75	4.7 ± 0.93	2.33	2.1 ± 0.42
5	3.37	2.6 ± 0.79	15.4	17 ± 3.3	9.80	15 ± 3.0
6	3.22	0.86 ± 0.26	1.79	4.6 ± 0.93	1.26	2.0 ± 0.4
7	2.82	1.3 ± 0.39	7.04	7.7 ± 1.5	3.58	6.7 ± 1.3
8	4.73	5.3 ± 1.1	17.7	21 ± 4.1	15.2	24 ± 4.8
10	8.90	4.2 ± 1.3	63.3	49 ± 10	14.8	30 ± 6.0

The flux calibrations above were compared for accuracy against published spectra by Fesen et al. (1997); however, this comparison is difficult due to positional errors based on locating the ground-based spectra location, the shape of the apertures used, and the expansion of the filaments since the spectra were taken. In addition, the ground-based spectroscopic studies had a much lower resolution than the 0.1" *HST* resolution and the intensities of the emission lines can vary dramatically over very small spatial scales. The *HST* images were made to have the resolution of the Fesen et al. (1997) ground-based observations to make the comparison. The values of flux

measured in the *HST* image (f_{HST}) versus the values quoted from Fesen et al. (1997) (f_{GB} , with associated errors) are listed in Table 4. The position value given is the position and coordinates used in the Fesen et al. (1997) paper.

The images were corrected for reddening due to interstellar dust by using the standard interstellar extinction curve given in Table 7.1 of Osterbrock (1989). The values from the table were used to interpolate the amount of relative extinction, f_λ for the specific wavelengths used in these observations assuming $R = 3.1$. The calculated relative extinction was used to determine the value of extinction in magnitudes using $A_\lambda = -2.5(c)(f_\lambda)$, where c is a constant. $E(B-V) \approx 0.77c$ for the standard reddening curve. The constant c is approximately 0.68 if we use $E(B-V) = 0.52$ for the Crab (Sollerman et al. 2000). The magnitude of extinction was converted to units of flux using $F_\lambda = 10^{-0.4A_\lambda}$. We found that that [O III] was reddened by 5.707 $\text{erg cm}^{-2} \text{s}^{-1}$. The average of the $\lambda\lambda 6717, 6731$ doublet was used for the reddening of [S II], and that value was 3.43 $\text{erg cm}^{-2} \text{s}^{-1}$. The reddening for [O I] was 3.79 $\text{erg cm}^{-2} \text{s}^{-1}$. The flux calibrated images were multiplied by these extinction values to correct the *HST* images for interstellar reddening along the line of sight to the Crab Nebula.

2.3. Overview of *HST* Observations

The relevance of having the mosaic in these three emission lines is that it provides a unique opportunity to study the ionization structure of the filaments because the [O III] traces high-ionization emission, [S II] traces intermediate-ionization emission, and [O I] traces the low-ionization emission. A visual inspection of the three line emission mosaics shows that there are fundamental differences between them,

shown in Figures 8, 9, and 10, which show [O I], [S II], and [O III], respectively. The [O III] observations show that this emission is the most diffuse, or least clumpy, of the three emission lines. The [O III] emission appears connected throughout the nebula, forming arcs and long continuous filaments. The long, linear filaments across the face of the nebula are likely also arcuate in shape but are viewed face-on rather than from the side. [O III] is the dominant emission at the very edge of the nebula and it marks the cooling region behind the shock front caused by the expanding synchrotron nebula (Sankrit & Hester 1997). For this reason, the [O III] extends the farthest from the center of the nebula and the major axis of the nebula is about 4.2 pc in [O III] emission. Most of the [O III] emission at the edge of the nebula has a cloud-like surface with a well-defined and connected edge, however in the NW this cloud-structure is absent and the filaments do not look as though they are connected. The gas that is in contact with the synchrotron nebula (at the contact-discontinuity) is also subject to photoionization and [O III] emission is caused in this way in addition to cooling behind the shock. Notably, the “jet” or “chimney” discovered by van den Bergh (1970) and noted by many others (Chevalier & Gull 1975; Wyckoff et al. 1976; Fesen & Gull 1986; Davidson & Humphreys 1976) is seen protruding from the north of the nebula in [O III] emission despite having a very low surface brightness. This structure appears connected to the surrounding [O III] emission and has been suggested to have formed by the shock front moving into very low density ejecta in the north (Sankrit & Hester 1997).

The [S II] emission, an intermediate emission line, does not extend as far from

the center of the nebula as the [O III] emission. The measured major axis of the nebula in [S II] emission is about 4.1 pc. The [S II] emission appears to have a diffuse component at the edge of the nebula but it does not appear connected like the [O III] emission does; it is broken up into diffuse clumps. Still, the diffuse component may be due to cooling ejecta behind the shock front. Moving inwards toward the center of the nebula, the [S II] emission arises from more compact and well-defined structures, much moreso than the [O III] emission in the interior parts of the remnant. The compact [S II] emission is likely contained in filaments that have already cooled radiatively and are being photoionized. The “chimney” is not visible in [S II] emission.

The [O I] emission has virtually no diffuse component at all, but appears as clumps of emission on small scales. The edge of the [O I] emission is very hard to define and does not appear continuous like the [O III] shell. The spatial extent of [O I] is the smallest of the three, only 3.9 pc. The clumpy nature of the emission is indicative of the gas being contained in dense regions in the filaments, where it is sheilded from the synchrotron radiation (Sankrit et al. 1998); this gas is contained within a thick, outer layer of gas that absorbs the photons and becomes ionized, leaving the neutral oxygen at the center. The [O I] emission follows the shape of the [O III] and [S II] emission because it is contained in the densest parts of those same filaments. Often the [O I] emission is found in regions where the gas is R-T unstable and therefore this emission is prominent in all the R-T fingers in the nebula.

The long bands of bright emission apparent crossing the center of the nebula are appear strong in all three emission lines, perhaps because we are looking through

more material than we see at the edge. We note that the gas at the center of the nebula has the highest radial velocity. Therefore what appear to be voids in the line emission in the center of the nebula are actually places where large Doppler-shifts may cause shifting of the outside of the bandpass filters. This is most significant for the [O III] and [O I] lines (Table 3).

The continuum mosaic of the Crab Nebula shows the synchrotron nebula and also locations where there is dust. There are regions where dark clumps appear surrounded by bright emission; these are regions where dust has absorbed synchrotron emission that is behind the dust along our line of sight. These dust absorption features have been noted in previous ground-based imaging (Fesen & Blair 1990; Hester et al. 1990), but *HST* images of the continuum are the first to actually resolve individual dust clumps with sizes less than $2''$, and such images have shown that they coincide with the line emission. The dust we observe must either reside on the near-side of the remnant or in filaments that are very nearly edge on. We can not observe dust within ejecta on the far-side of the remnant or dust in filaments where the synchrotron emission is weak because the extinction would be at levels too low to be noticed. For those reasons, we estimate that the areas of extinction we see in the continuum image represents about half of the dust contained in the Crab Nebula filaments.

2.4. Supporting Observations

2.4.1. *Fabry-Perot Data*

Fabry-Perot (F-P) data from Lawrence et al. (1995) were used extensively in this research for the purpose of determining the locations of filaments in the nebula,

especially to determine whether specific filaments were on the front face of the nebula or on the backside. The Fabry-Perot data set was taken using [O III] $\lambda 5007 \text{ \AA}$ emission exposed for 300 s at the 1.3 m *McGraw – Hill* telescope in 1989. The bandpass of the [O III] filter had a FWHM of 5.3 \AA , which corresponds to a velocity width of 320 km s^{-1} . The velocity range of the observations was for radial velocities between -1800 km s^{-1} and $+1800 \text{ km s}^{-1}$ with respect to $\lambda = 5007 \text{ \AA}$. The filaments in the Crab Nebula have a radial velocity range of up to roughly 1500 km s^{-1} and therefore should all be measured in the data. The observations were spread by 130 km s^{-1} increments with a resolution 260 km s^{-1} , meaning that two distinct emission line features would need to be separated by a minimum of 260 km s^{-1} in order to be independently resolved. The uncertainty in the velocity is 100 km s^{-1} . The [O III] filaments were resolved up to $0.5''$. This F-P data set is the most comprehensive study of the velocity structure of the entire Crab Nebula and was instrumental in this research.

The F-P data set confirmed that most of the [O III] emission comes from a shell that surrounds the synchrotron nebula, evidenced by the zero-velocity emission coming from the periphery of the nebula while the emission with the highest radial velocities is concentrated near the center. Lawrence et al. (1995) determined that the inner synchrotron nebula appears as an ellipse with dimensions of roughly $4' \times 3'$ with the major axis tilted about 50° west of north. The [O III] emission has the same major axis angle. Interestingly, the highest radial velocities (both red- and blue-shifted) are found in the northwest part of the nebula. The most surprising result

of this analysis was that when the data are viewed along the major axis, there is a central void through the entire nebula as though one were looking through an open-ended barrel. The velocity offsets of the axis defined by these holes are -900 km s^{-1} in the SE and $+900 \text{ km s}^{-1}$ in the NW. The estimated positioning of the nebula along our line of sight is 55° to the west of north and about 25° into the plane of the sky with the NW being tilted away from earth. This projection is nearly coincident with the proper motion of the pulsar (and the jets of the pulsar), meaning that they both reside near the plane in which the filaments appear to only have a transverse velocity from our vantage point on Earth (radial velocity = 0).

The Fabry-Perot data set was essential in this work for determining the physical location in 3-dimensional space of the filaments. We used the 3-D information to model the Crab Nebula as a prolate ellipsoid and to estimate the distance of the shock at the edge of the nebula from the pulsar and the expansion center. Another useful means for the F-P data was that it gave us a way to determine which filaments lie on the front side of the nebula and which filaments lie on the back side of the remnant. This was important in our studies of dust in the Crab Nebula in particular, because the dust we see in our continuum image (Chapter 8) is visible by extinction of the synchrotron emission that lies behind the dust. We can only see dust in this way if it resides on the front side of the remnant and therefore it is essential to know which filaments lie on the front side if we want to know the percentage of the filaments contain dust. Although the spatial resolution of the F-P observations is much coarser than the *HST* images, the filaments are resolved (but small R-T fingers are not).

Large-scale filamentary structures could easily be correlated between the *HST* and F-P data sets and for those filaments we knew from their radial velocity if they were on the front side or on the back side of the remnant.

CHAPTER 3

The Variation of Pre-Shock Ejecta Density

There have been several studies of the interstellar environment surrounding the Crab Nebula using H I observations. Wallace et al. (1999) conducted the highest resolution ($9'$) H I maps using the Effelsberg 100 meter radio telescope. They also used the Dominion Radio Astrophysical Observatory Synthesis Telescope to obtain $1' \times 3'$ resolution images in the Crab Nebula region to determine if the remnant exists in a low density environment. They combined their maps with velocity constraints to infer that there is a bubble, or a very low density environment, surrounding the Crab Nebula. The bubble is about 3.5 deg in diameter (about 120 pc) and is expanding with a velocity of $\approx 6.5 \text{ km s}^{-1}$. The kinematic age for the bubble is 8×10^6 years, more than 1000 times the age of the Crab Nebula. The Crab is located about 17 pc off-center of the bubble and Wallace et al. (1999) conclude that there is no strong indication of any interaction between the Crab Nebula and the surrounding interstellar environment.

There is no direct explanation for the why the Crab exists in such a low density environment. Possible explanations include stellar winds that forced the surrounding interstellar medium out, or the occurrence of previous supernovae clearing out the area prior to the Crab supernova event (Romani et al. 1990). The significance of the bubble is two-fold. First, the low-density environment surrounding the Crab Nebula provides an explanation for why the outermost blast wave has never been detected – the amount of shocked ISM would have line intensities too low to be detected (Fesen et al. 1997). The second important implication is that the ejecta from the explosion would expand freely in all directions. For this reason, we assume from this point

forward that the ejecta were expelled in a spherical distribution during the explosion. It is also reasonable to assume that since the density gradient of a star is negative the ejecta has a decreasing density profile with distance from the expansion center. The density of the ejecta follows $\rho \propto R^{-n}$, where R is the distance from the center of the star and $n > 0$. We must speak of the angle-averaged density, though, because the ejecta do not explode isotropically. Numerical studies indicate that Rayleigh-Taylor (R-T) and Richtmeyer-Meshkov instabilities occur at the interface between the Si/O and (C+O)/He pre-supernova shells, which cause the ejecta to form metal-rich clumps of gas within a few minutes of the explosion (Kifonidis et al. 2003).

3.1. The Effect of the Nebula's Geometry on Ejecta Density

In Chapter 1 we discussed the work by Kaplan et al. (2008) who measured the transverse velocity of the Crab Pulsar to be about 120 km s^{-1} in the northwest direction, and therefore has traveled approximately 0.12 pc since the time of the explosion. The pulsar has an apparent symmetry axis that runs southeast to northwest and is inclined about 33° into the plane of the sky (Hester et al. 1995), and this angle is very well correlated with the overall three-dimensional shape of the nebula according to velocity studies (Lawrence et al. 1995). Hester et al. (1995) used *HST* and the Röntgen Satellite (*ROSAT*) images to determine that there are two persistent knots present in the southeast direction of the pulsar at distances of $0.65''$ and $3.8''$. The knot that is closest to the pulsar was interpreted by Hester et al. (1995) to be a shock in the pulsar wind. They also found that there is a jet of X-ray emission that lies along a line that is tilted about 30° in the northwest direction. The bulk of the

pulsar's energy being distributed in the NW-SE direction in the form of jets, serve to elongate the synchrotron nebula in the SE-NW direction and cause it to have the elliptical shape that we see in images of the Crab Nebula.

The transverse velocity of the Crab pulsar toward the NW in addition to the energy distribution of the pulsar in the NW-SE direction in the form of jets (due to the toroidal magnetic field) have important implications on the overall evolution of the remnant. As mentioned previously, the Crab supernova explosion occurred in a bubble of low-density ISM that has a radius of about 90 pc; we may assume the ejecta are freely expanding in a spherical distribution away from the explosion center (located about 0.12 pc to the SE of the current pulsar location). Although we can not observe the freely expanding ejecta directly, the continuing existence of the filaments surrounding the synchrotron nebula provides evidence that the freely expanding remnant exists (Sankrit & Hester 1997). [C IV] measurements of the radial velocity of filaments indicate that there is gas moving at speeds of at least $\pm 2500 \text{ km s}^{-1}$ (Sollerman et al. 2000), while the fastest moving, visible, filaments are moving at $\pm 1500 \text{ km s}^{-1}$. Even though the freely expanding ejecta may be spherically distributed around the explosion center, the filaments (made of cooled, shocked ejecta) follow the elliptical shape of the synchrotron nebula that is in turn driven by, and assumes the morphology of, the pulsar's energy.

To measure the spatial extent of the synchrotron nebula, we used the *VLA* radio data from Bietenholz & Kronberg (1990) because it is the farthest extending synchrotron emission from the pulsar and therefore most closely represents the loca-

tion of the shock front. The [O III] *HST* mosaic presented in this dissertation was used to determine the distribution of the ejecta because at the edge of the nebula the [O III] emission arises from gas that is cooling immediately behind the shock (Sankrit & Hester 1997). In both the *VLA* and *HST* data sets, we mapped the x-y coordinates of the outer perimeter of the emission by hand. These x-y coordinates were used in the program *mpfitellipse*, a procedure developed by Craig Markwardt (NASA/GSFC), to fit a closed elliptical curve to both the radio and the [O III] line emission. The program calculates the center and dimensions of the ellipse (in the plane of the sky) as well as a total χ^2 for the fit. The program also provides the number of points used (N) and the number of free parameters (m). These values were used to calculate the reduced chi squared determined by $\chi^2_\nu = \chi/(N - m)$. Figure 13 shows the mapped outer edges and best fit ellipse to the synchrotron nebula (red, $\chi^2_\nu = 13/(882 - 877) = 2.6$), the mapped edge and corresponding best-fit ellipse to the [O III] emission (green, $\chi^2_\nu = 4.6/(327 - 322) = 0.92$), the current location of the pulsar, and the expansion center determined by Kaplan et al. (2008). The center of the ellipses are represented by a red triangle for the synchrotron nebula and a green square for the [O III] emission. Although both of the ellipses are near the pulsar, it is clear that they are not coincident. According to these results, the synchrotron nebula emission extends farther from the pulsar in the NW direction than in the SE direction, which is not the case for the line emission. In other words, the filaments are no longer forming in the NW and the synchrotron nebula has been able to expand outward more in this direction. This has been noted from earlier observations by

Velusamy (1984) and Sankrit & Hester (1997) and it is also seen in our *HST* images (Figure 12).

3.2. Constructing a 3-D Ellipsoid to Model the Crab Nebula

A major goal of this dissertation is to apply the model by Jun (1998) to the Crab Nebula and determine how the ejecta density, shock speeds and development of R-T instabilities differ between the northwest and southeast ends. To quantify these parameters, it is necessary to estimate the distance from the expansion center to the location of the shock. Although we can not see the shock directly, it can be assumed that it is approximately at the edge of the synchrotron nebula as seen in *VLA* radio data of the Crab (Bietenholz & Kronberg 1990). Rather than simply measuring distances to the edge of the nebula using the distance we measure on the sky in the *HST* and *VLA* images, we constructed a three-dimensional model of the Crab Nebula. This was done by incorporating the results of Fabry-Perot (F-P) data and analysis by Lawrence et al. (1995). Their F-P data set revealed the three-dimensional structure of the Crab Nebula by observing the Crab at specific radial velocities and then converting the radial velocities of the filaments into positions along the line of sight. These studies indicated that the Crab Nebula is a prolate ellipsoid with the major axis tilted along the SE-NW direction at an angle of about 60° in the plane of the sky (east of north) and about 30° into the plane of the sky (in excellent agreement with the pulsar jets, (Hester et al. 1995)) such that the NW portion of the nebula is farther away from earth than the SE side.

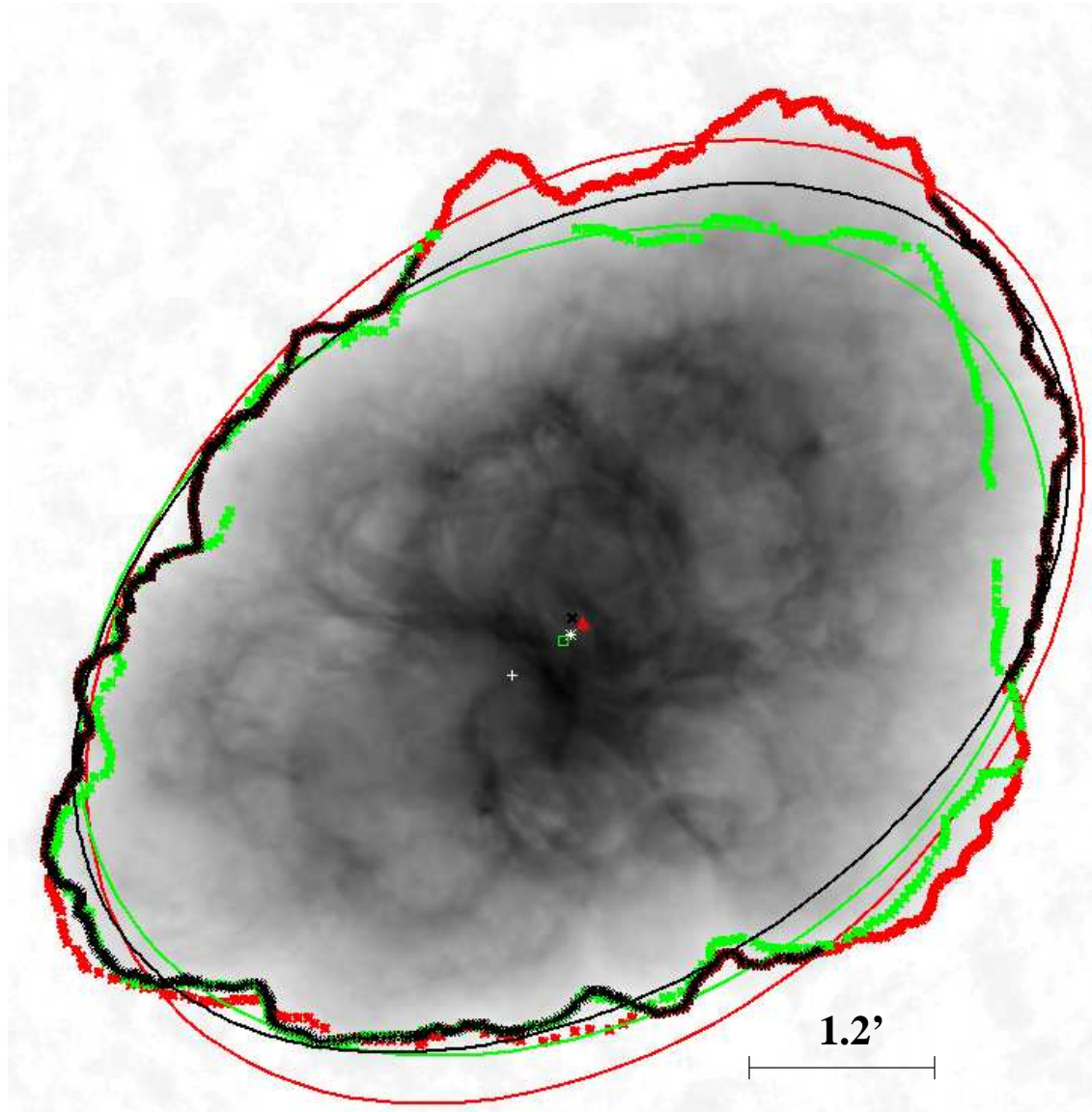


Figure 13. The *VLA* radio image from Bietenholz & Kronberg (1990). Overlaid on the image are the best-fit ellipses, determined using the program *mpfitellipse*, corresponding to the outer radio edge of the synchrotron nebula (red) and the [O III] emission (green). The black ellipse represents the best-fit ellipse using only regions where the edges of [O III] and radio emission coincide. The center of each ellipse is represented by a symbol of the same color. The pulsar is located at the white \times , and the explosion center is located at the white $+$.

Our goal was to use the angles discussed above to create a 3-D prolate ellipsoid that conforms to the shape of the radio emission we see from Earth (Bietenholz & Kronberg 1990). To constrain the outer boundary of the ellipsoid, we fit an ellipse to the portion of the Crab Nebula where the [O III] edge and the synchrotron nebula boundary are nearly coincident. Apparent in Figure 13, the ellipses fit using the [O III] boundary, the synchrotron nebula boundary, and the region where just the [O III] and synchrotron nebula coincide, are all very similar. We could choose any of these three ellipses as the boundary, but we chose to use the ellipse created by using the areas where the [O III] and synchrotron nebula coincide because that ellipse seemed to be the best fit to the edge of the nebula in the NW and the SE, which are of particular interest to this work. Figure 13 shows the locations used for the fit (the black boundary), the resulting ellipse in black and the center of that ellipse (black \mathbf{x}). The fit has a $\chi^2_{\nu} = 4.5/(724 - 719) = 0.9$, which is the best fit out of the three ellipses. At the SE edge, the ellipse has a maximum deviation from the mapped edge of the nebula of about 0.14 pc as measured on the plane of the sky and in the NW the edge of the ellipse is coincident with the *VLA* radio edge. The 2-D ellipse was used to provide the boundary conditions for the 3-D ellipsoid, meaning that we used the center of the 2-D ellipse to represent the center of the 3-D ellipsoid and also constrained the outer edge of the rotated ellipsoid to match the boundary of the 2-D ellipse.

The 3-D prolate ellipsoid was created by constructing a series of longitude and latitude lines that curved according to equation for a prolate ellipsoid: $(x^2/a^2 +$

$y^2/b^2 + z^2/c^2 = 1$ and $a = b < c$). We find that the shape of the Crab Nebula is well approximated by a prolate ellipsoid with a major axis ($2c$) equal to 4.57 pc and minor axes ($2a$ and $2b$) equal to 2.9 pc. First we created an array of angles between 0 and 2π (θ) and another array of angles between 0 and π (α). Using spherical coordinates, x, y and z values were calculated using $x = a \sin(\theta) \cos(\alpha)$, $y = b \sin(\theta) \sin(\alpha)$ and $z = c \cos(\theta)$. The y-z plane represents the plane of the sky and the x direction is perpendicular to the plane of the sky. The ellipsoid was constructed with its major axis in the N-S direction. Then we rotated the ellipsoid in the plane of the sky using the transformation matrix

$$\begin{bmatrix} x' \\ y' \\ z' \end{bmatrix} = \begin{bmatrix} 1 & 0 & 0 \\ 0 & \cos \phi & \sin \phi \\ 0 & -\sin \phi & \cos \phi \end{bmatrix}$$

where $\phi = 51.5^\circ$ was used because this provided the best match to the ellipse generated from *mpfitellipse* and it was consistent with the Lawrence et al. (1995) results. Next, we rotated the ellipsoid into the plane of the sky by the amount $\beta = 30^\circ$ using a similar matrix:

$$\begin{bmatrix} x'' \\ y'' \\ z'' \end{bmatrix} = \begin{bmatrix} \cos \beta & 0 & -\sin \beta \\ 0 & 1 & 0 \\ \sin \beta & 0 & \cos \beta \end{bmatrix}.$$

These rotations are consistent with what Lawrence et al. (1995) estimated the tilt of the nebula is from the F-P studies and it is also consistent with the alignment of the pulsar (Hester et al. 1995). These angles of rotation and dimensions of the ellipse were determined by plotting the 2-D ellipse boundary over the 3-D ellipsoid

so that after the rotations the ellipsoid had dimensions that were coincident with the boundary of the 2-D ellipse. The 3-D ellipsoid is shown overlain on the *VLA* radio data in Figure 14.

Having constructed a 3-D ellipsoid that has the approximate shape of the nebula, we next used the x , y , z locations at the edges to determine 3-D distances from both the pulsar and the expansion center (Kaplan et al. 2008). The major axis was constructed by numerically creating a line and applying the same 3-D transformation matrices to the line as we applied to the ellipsoid. We needed to know the angle that the rotated axis made along our line of sight to earth, so the line was then projected onto the 2-D plane of the sky. We find that the major axis of our ellipsoid would appear to be tilted at about 55° east of north, which is in excellent agreement with the estimates given by Lawrence et al. (1995). Based on the location of the major axis of the 3-D ellipsoid after these rotations were applied, neither the pulsar nor expansion center were exactly on the calculated major axis but both were consistent with it and within the uncertainties of the 2D ellipse construction. The 2D ellipse varied as much as 0.14 pc from the farthest synchrotron emission (this maximum value occurred in the SE). In order to simplify our distance calculations, we assumed that the pulsar and the expansion centers lie along the major axis of the ellipsoid. We projected them onto the axis by using positional information from the image (pixel locations) and basic geometry to perform the projection (see Figure 15). We measured the $\Delta x = x_c - x$ and $\Delta y = y_c - y$, where x_c and y_c are the coordinates for the center of the ellipsoid, and x and y are the coordinates of either the pulsar or the expansion center.

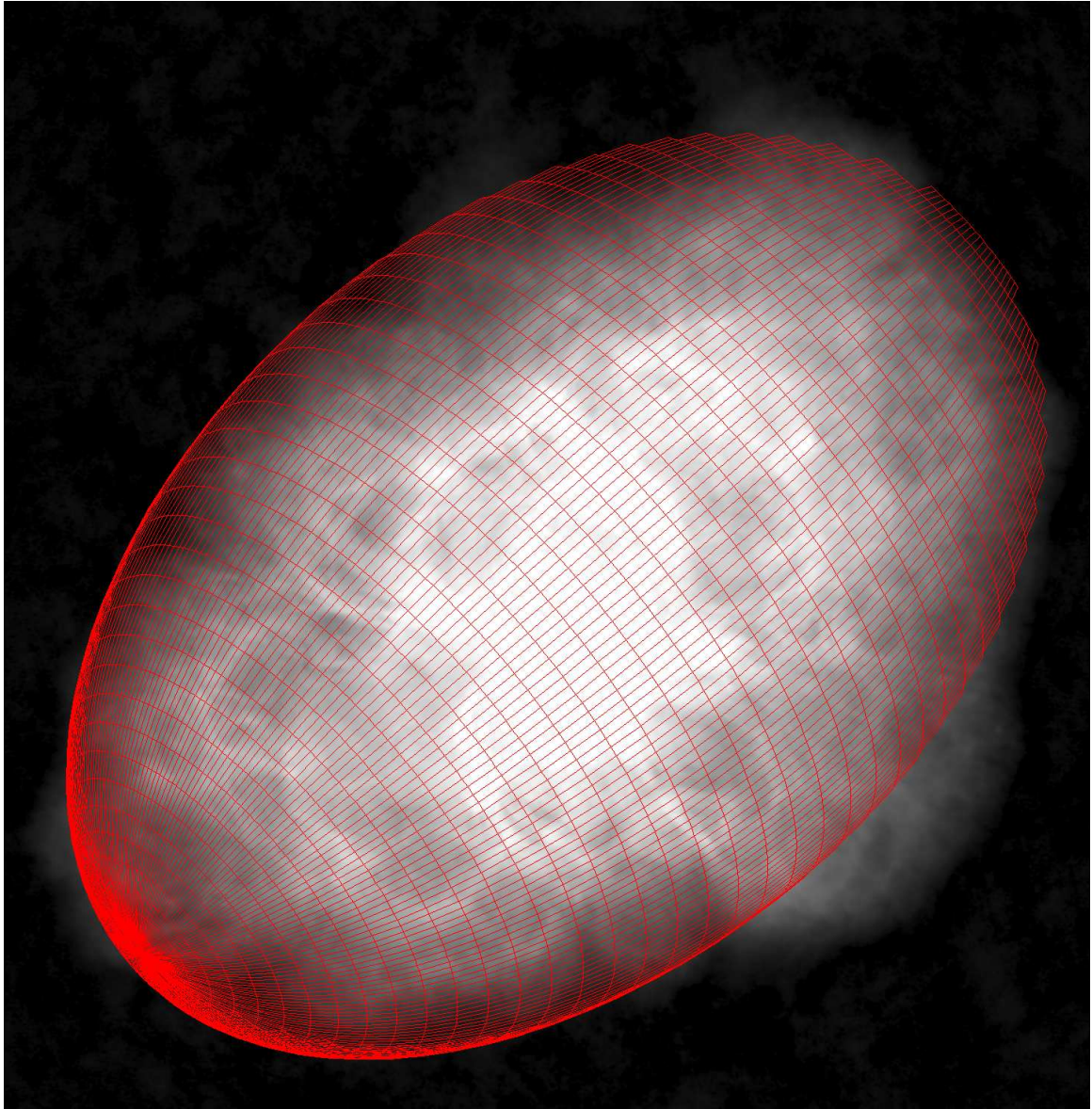


Figure 14. The best-fit three-dimensional ellipsoid created using positional values based on Fabry-Perot data of the Crab Nebula. The ellipsoid is tilted 51.5 degrees in the plane of the sky (West of North) and 30 degrees into the plane of the sky.

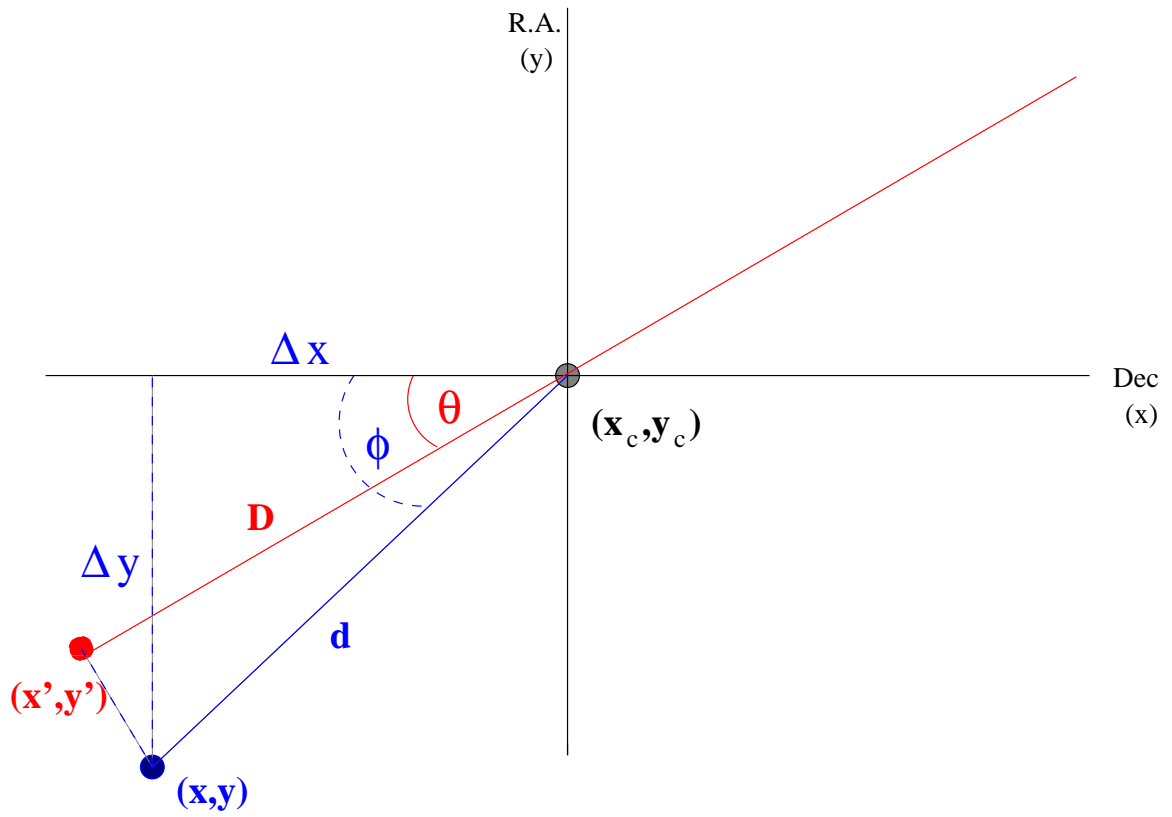


Figure 15. The angles and positional information used to project the location of the pulsar onto the major axis of our 3-D ellipsoid in order to calculate 3-D distances to the shock front.

The distance from the center of the ellipsoid to the actual position of the pulsar (or expansion center), d , follows from $d = [(\Delta y)^2 + (\Delta x)^2]^{1/2}$. The angle between the line of declination of the pulsar (or explosion center) and the major axis of the ellipsoid, θ , was determined by projecting the rotated major axis onto the plane of the sky and is equal to 38.5° (Figure 15). The angle between the line of declination of the pulsar (or expansion center) and the line of sight projection of the pulsar (or expansion center) is $\phi = \tan^{-1}(\Delta y/\Delta x)$. The distance from the center of the ellipsoid to the projected positions onto the major axis of the ellipsoid is $D = d \cos(\phi - \theta)$. Once this distance is known, the projected coordinates are simply $x' = D \sin \theta$ and $y' = D \cos \theta$. The z' position is calculated from $z' = D/\cos \zeta$ where $\zeta = 30^\circ$, the tilt of the nebula into the sky. In the plane of the sky (2D), the distance the pulsar (or expansion center) was moved is $r^2 = [(x - x')^2 + (y - y')^2]^{1/2}$. The pulsar was projected a distance of $r_p = 0.05$ pc from its actual position and the expansion center was projected a distance of $r_e = 0.03$ pc. The error of this projection can be calculated as follows: $\delta D = (D^2 + r^2) - D = D[(1 + (r^2/D^2))^{1/2} - 1]$ and because we are working with small angles, this can be approximated by $\delta D/D \approx 1 + 1/2(r^2/D^2) - 1 = (r^2/2D^2)$. We find that $\delta D/D = 0.78$ for the pulsar and $\delta D/D = 0.004$ for the expansion center. These errors will have no bearing on our subsequent conclusions because the distances of the projections are about 0.1 % of the distances to the edge of the nebula.

Distances from the pulsar and the expansion center to several locations around the perimeter were determined by using the x , y , z positions at the edge of the radio emission (the approximate location of the shock front) determined from the

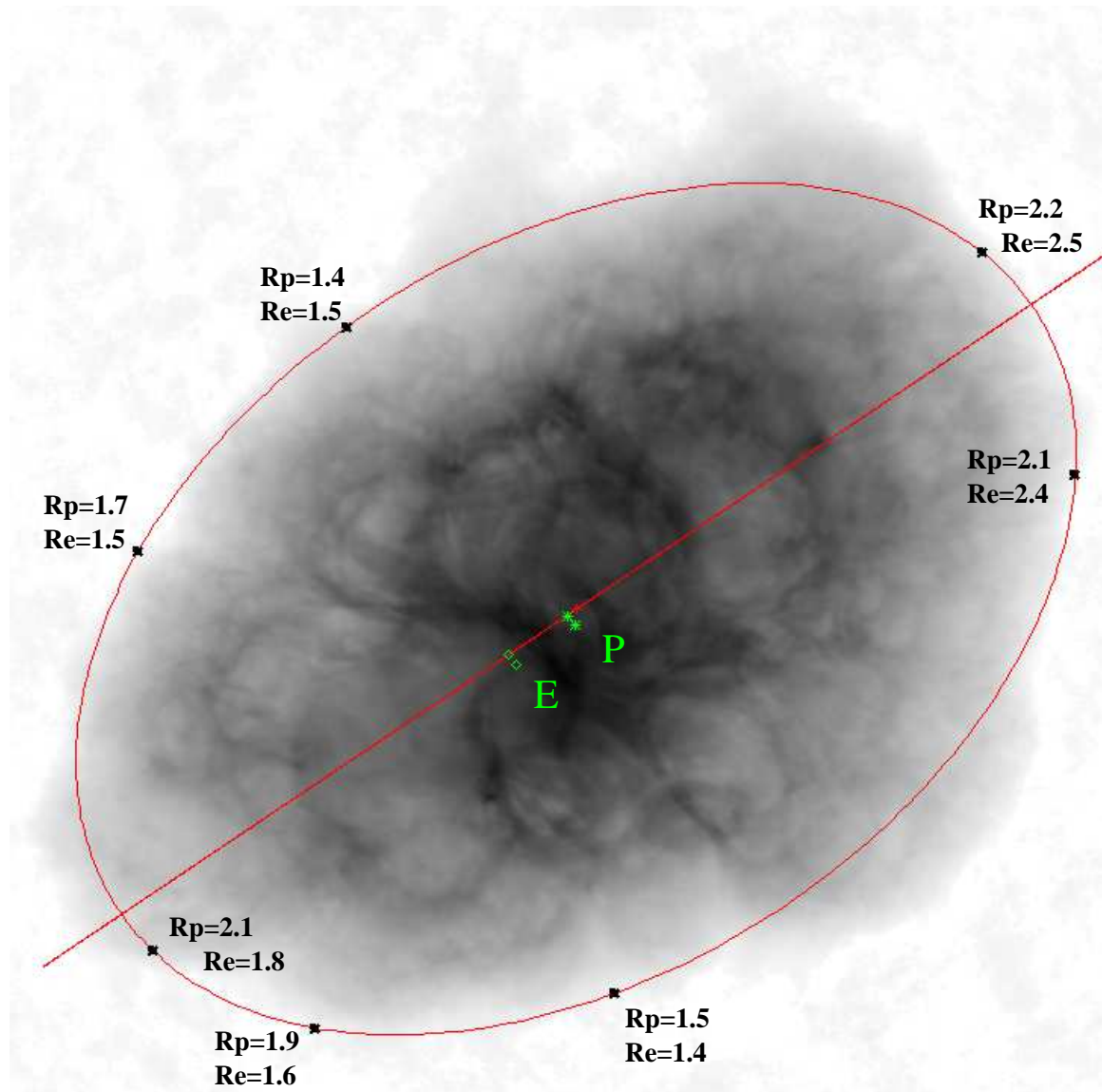


Figure 16. Points around the perimeter of the Crab Nebula where the distance was estimated using the 3-D distances (in pc) from our prolate ellipsoid model and 3-D projected locations of the pulsar and the expansion center. The red line is the major axis of the ellipsoid that was constrained to lie within the boundary of the red ellipse. P marks the position of the pulsar and E marks the expansion center as determined by Kaplan et al. (2008), both of which are shown as they appear on the sky and after applying our projections onto the ellipsoid major axis. R_p is the distance from the pulsar (pc) and R_e is the distance from the expansion center (pc) at the position of the corresponding black \times .

3-D ellipsoid and the equation $r = [(x - x')^2 + (y - y')^2 + (z - z')^2]^{1/2}$, where x' , y' and z' are the projected positions of either the pulsar (Rp) or the expansion center (Re). The locations and values of the distance estimates were chosen to be places where edge of the emission appeared to be well correlated with the edge of the ellipsoid. These positions in addition to the actual and projected positions of the pulsar and expansion center are shown in Figure 16. In Figure 16, the red boundary represents the 2-D ellipse boundary and the 3-D ellipsoid outer edge (they are coincident as discussed above). The red line is the major axis of the ellipsoid as it would appear when projected onto the plane of the sky.

3.3. The Pre-shock Ejecta Density is Asymmetrical

Now that we have estimated the three-dimensional distances to the edge of the shock, we may apply these distances to the model by Jun (1998) to estimate the variation in ejecta density between the NW and SE sides of the remnant. We must use an estimate that lies on the edge of the nebula along our line of sight, and we note that the distances that we have calculated are likely not the farthest distances on either side, due to the tilt of the nebula (Figure 14).

The ratio in the estimated distances between the NW and SE sides of the remnant as a function of distance from the explosion center is:

$$\frac{r_{\text{NW}}}{r_{\text{SE}}} = \frac{2.5}{1.8} = 1.4 \quad (3.1)$$

This ratio is likely an over-estimate due to us not using the farthest point in the SE due to the ellipsoid boundary. However, even with a 0.14 pc error in distance, the ratio would change only by about 8% (± 0.1). If the density of the ejecta is

distributed symmetrically around the expansion center and decreases with distance as we assume, then the pre-shock ejecta that the shock is encountering in the NW would be less dense than the pre-shock ejecta the shock is encountering in the SE.

The Jun (1998) model assumes that the ejecta is distributed around the pulsar rather than the expansion center. If this were the case, then since

$$\frac{r_{\text{NW}}}{r_{\text{SE}}} = \frac{2.2}{2.1} \approx 1, \quad (3.2)$$

we would not expect the pre-shock ejecta density to be very different in the NW than the SE.

The distribution of the ejecta plays a significant role in the evolution of the nebula. Intuitively, the shock front will move slower when it is encountering denser ejecta than when the ejecta is less dense. Faster moving shocks heat the post-shock gas to higher temperatures and the post-shock gas takes longer to cool through radiation. The formation of filaments requires the pre-shock ejecta density be high enough that the shocked gas can cool radiatively on small timescales. Otherwise, the synchrotron nebula can expand beyond the shocked gas because it is no longer confined. We have already shown that the synchrotron nebula does extend beyond the filaments in the NW but filaments are continuing to form in the SE (Figure 12). We suggest this is directly due to the ejecta being distributed around the expansion center, not the pulsar, and the shock moving into less dense ejecta in the NW than in the SE.

3.4. Results

Our 3-D distance calculations of the shock front using a model of the Crab Nebula as a prolate ellipsoid, in conjunction with the *HST* observations of the Crab

that show the expansion of the synchrotron nebula beyond the filaments in the NW but constrained by filaments in the SE, provides theoretical and observational evidence that there is an asymmetry present between the NW and SE ends with regards to the pre-shock ejecta density. The asymmetry can be understood as arising from the synchrotron nebula being centered around the pulsar, and the density distribution of the ejecta being centered on the expansion center. The pulsar's transverse velocity toward the NW at a velocity of about 120 km s^{-1} has caused the synchrotron nebula to be carried along with it. The synchrotron nebula has expanded in time due to a constant energy input from the pulsar, and has expanded rather symmetrically about the pulsar's location in time. The synchrotron nebula is farther from the explosion center in the NW direction than it is in the SE direction. At the same time, the ejecta from the explosion have been freely expanding outward from the explosion center. The shock encounters the freely expanding ejecta at roughly the location of the edge of the synchrotron nebula. Assuming that the density of the ejecta falls off according to $\rho \propto r^{-n}$, this would indicate that the shock is encountering less dense ejecta in the NW than in the SE. (The shock would have already progressed through the ejecta with the same pre-shock ejecta density as what the shock is encountering now in the SE). A lower ejecta density would lead to higher shock speeds and longer cooling times in the NW, and there is observational evidence that this is the case because the synchrotron nebula has expanded beyond the filaments in the NW direction.

In Chapter 4, we will discuss the variations in shock speeds between the NW

and SE ends of the nebula. The speed of the shock affects the cooling time of the shocked gas and the formation of filaments. These parameters are important for applying the model by Jun (1998) to the Crab Nebula as we understand it.

CHAPTER 4

Varying Shock Speeds Around the Perimeter of the Crab

Sankrit & Hester (1997) used the line intensities of the filamentary structure in the Crab Nebula to create a model that convincingly shows that a shock wave is propagating outward from the synchrotron nebula into freely expanding ejecta. The shock wave is due to the large pressure differential between the synchrotron nebula (expanding due to the constant input of energy from the pulsar) and the overlying ejecta expelled during the supernova explosion that constrains the synchrotron nebula's expansion. The shock is propagating just beyond the bounds of the visible line emission into freely expanding ejecta. The ejecta is being carried by the momentum of the original explosion. The model by Sankrit & Hester (1997) estimates that the average pre-shock ejecta density is less than $\rho/m_H \approx 15 \text{ cm}^{-3}$. At these densities and shock speeds of about 150 km s^{-1} , the ejecta becomes heated to very high temperatures (10^4 K) and then the gas cools radiatively mostly in the form of magnetic-dipole transitions (forbidden line emission). The cooled, shocked ejecta form dense structures which are referred to as filaments and which are visible via line emission in the Crab Nebula. These filaments literally rest on the surface of the synchrotron nebula, forming a shell or "skin". The continued existence of filaments indicates that gas is constantly being added to the skin; otherwise, the synchrotron nebula would have easily broken through the filamentary cage that instead has been shown to exist for as long as we have observed the Crab.

4.1. Shock Properties as a Function of Preshock Ejecta Density

The extremely high sound speed in the relativistic plasma ($c_s = c/\sqrt{3} \approx 1.7 \times 10^{10} \text{ cm s}^{-1}$, (Gaensler & Slane 2006)) ensures that the pressure inside the

synchrotron nebula can be assumed equal everywhere - any pressure differences that may develop are quickly smoothed out on timescales of at most 30 years (Hester et al. 1996). The pressure in the Crab Nebula can be calculated from the magnetic pressure, $P_{\text{syn}} = B^2/8\pi$. Using the canonical minimum energy equipartition field strength for the Crab synchrotron nebula, 300 μG (Trimble 1982), then $P_{\text{syn}} = 3.5 \times 10^{-9}$ erg cm^{-3} (Sankrit & Hester 1997). The interior pressure leads to a strong shock which has a speed determined from $P_{\text{syn}} = \rho v_s^2$. If the pressure of the synchrotron nebula is the same between the NW and SE sides of the nebula, then the shock speed is contingent upon the density of the supernova ejecta that the synchrotron nebula is expanding into. Lower preshock ejecta densities will lead to faster shock velocities. As discussed in Chapter 3, the pre-shock ejecta density that the shock is propagating into is less in the NW than it is in the SE; we suggest this variation causes a dramatic effect on the shock properties between these two sides.

The Rankine-Hugoniot jump conditions for a strong shock front where the shock speed is much greater than the speed of the pre-shock gas, without taking into account magnetic fields, are

$$\rho_o v_o = \rho_1 v_1 \text{ (Conservation of Mass Flux)} \quad (4.1)$$

$$P_o + \rho_o v_o^2 = P_1 + \rho_1 v_1^2 \text{ (Conservation of Momentum Flux)} \quad (4.2)$$

$$\frac{1}{2}v_o^2 + \frac{1}{1-\gamma} \frac{P_o}{\rho_o} = \frac{1}{2}v_1^2 + \frac{1}{1-\gamma} \frac{P_1}{\rho_1} \text{ (Conservation of Energy Flux)} \quad (4.3)$$

$$\cdot \quad (4.4)$$

These equations show the relationship between the pre-shock (subscript 0) and post-shock (subscript 1) conditions. All shocks are considered “strong” just behind the

shock front, which is what we are considering here. For strong shock, the gas pressure in the preshock gas is considered negligible to the ram pressure ($P_o \approx 0$). The law of conservation of energy requires that the kinetic energy lost in the shock is converted to thermal energy in the plasma; the postshock gas reaches very high temperatures and does not cool quickly. The assumption of a strong shock allows us to substitute $P_o = 0$ in the above equations and combining:

$$\frac{\gamma + 1}{\gamma - 1}\beta^2 - \frac{2\beta}{\gamma - 1}(M^{-2} + \gamma) + \frac{2M^{-2}}{\gamma - 1} + 1 = 0 \quad (4.5)$$

where γ is the degrees of freedom of the atom, $\beta = v_1/v_o$ and M is the Mach number of the shock, equivalent to v_o^2/c_s^2 . The adiabatic sound speed of the gas is defined as $c_s = \gamma P_o/\rho_o$. Strong shocks have velocities that are greater than the sound speed of the gas ($M \gg 1$, $M^{-2} \approx 0$) and since the shock is stationary in the frame of reference $v_o \equiv v_s$. For a monotonic gas with $\gamma = 5/3$, the solutions to these conditions are:

$$v_1 = \frac{v_s}{4} \quad (4.6)$$

$$\rho_1 = 4\rho_o \quad (4.7)$$

$$P_1 = \frac{3}{4}\rho_o v_s^2. \quad (4.8)$$

These equations imply that with a constant input of energy into the synchrotron nebula from the spin-down luminosity of the pulsar, a relatively constant pressure at the nebula's perimeter, and a decreasing density gradient with distance from the explosion center, the shock propagating outward from the synchrotron nebula should be speeding up as time goes on. This realization is quite important to understand if one is trying to explain the differences in the filamentary properties around the perimeter of the nebula.

The internal energy of the postshock gas is $\epsilon = 3P_1/2\rho_1$ and, using the results above for a strong shock, this equates to $9v_s^2/32$. Substituting this into the equation of state, $P = nkT$, where $n = \rho/\mu m_H$, we can determine the temperature in the post-shock gas from the following:

$$T_1 = \frac{3\mu m_H v_s^2}{16k}. \quad (4.9)$$

Further, if we assume that the gas behind the shock is fully ionized, then

$$T_1 \approx 1.5 \times 10^5 \left(\frac{v_s}{100 \text{ km s}^{-1}} \right)^2 \text{ K}. \quad (4.10)$$

The importance of the above equation is that faster shocks will result in higher post-shock gas temperatures. Higher gas temperatures inevitably lead to longer cooling times, with the relationship of cooling time to temperature being

$$t_{\text{cool}} = \frac{3(n_e + n)kT_f}{2n^2\Lambda(T_f, Z_A)}, \quad (4.11)$$

where n_e is the number density of electrons, n is the total ion number density, and $\Lambda(T_f, Z_A)$ is the cooling function. A plot of the cooling function and the temperature of the gas is shown in Figure 17. The column density of the gas also increases in proportion to the cooling time and shock speed ($N_d = \rho_0 v_s t_{\text{cool}}$), such that a longer cooling time and a faster shock will lead to a larger column density of gas in the cooling region. At a certain cut-off velocity, the gas can no longer cool radiatively on short timescales, and the shock transitions to being effectively adiabatic (or non-radiative). In this case the gas behind the shock takes a much longer time to cool. The shock models by Sankrit & Hester (1997) showed that if the shock produced by the synchrotron nebula reaches about 200 km s^{-1} , the post-shock temperatures are

so high that the gas does not have time to cool within the age of the remnant. The estimated pre-shock ejecta density at that shock speed is $\rho/m_{\text{H}} < 10 \text{ cm}^{-3}$.

Sankrit & Hester (1997) explained that once the shock transitions to a non-radiative shock, the post-shock gas temperatures are so high that the filaments no longer form. Velusamy (1984) first noted that the synchrotron nebula has expanded beyond the filaments in the northwest region of the nebula. Figure 2 shows the [O III] line emission overlaid onto *VLA* radio data of the synchrotron nebula and it is clearly seen that the synchrotron nebula extends beyond the [O III] emission in the NW while the rest of the perimeter has a coincidence between the [O III] edge and the radio edge. Sankrit & Hester (1997) attribute the breakthrough of the synchrotron nebula in the NW to a higher shock speed (lower pre-shock ejecta density) in this area compared to the rest of the perimeter. The 3-dimensional ellipsoid presented in Chapter 3 provides an indication that the shock is encountering less dense ejecta in the northwest than at other areas around the perimeter due to the shock being farthest from the explosion center in the northwest.

4.2. Observational Support of Varying Shock Speed

The observations presented here can be used to determine if the shock speed varies by observing differences in the filamentary properties around the perimeter of the Crab Nebula. For example, in regions where the shock is propagating the fastest, we would not expect filaments to form as readily as they do where the shock speed is lower. Also, regions with high shock speeds would have less low-ionization line emission, due to both the high temperatures and lower post-shock densities. The

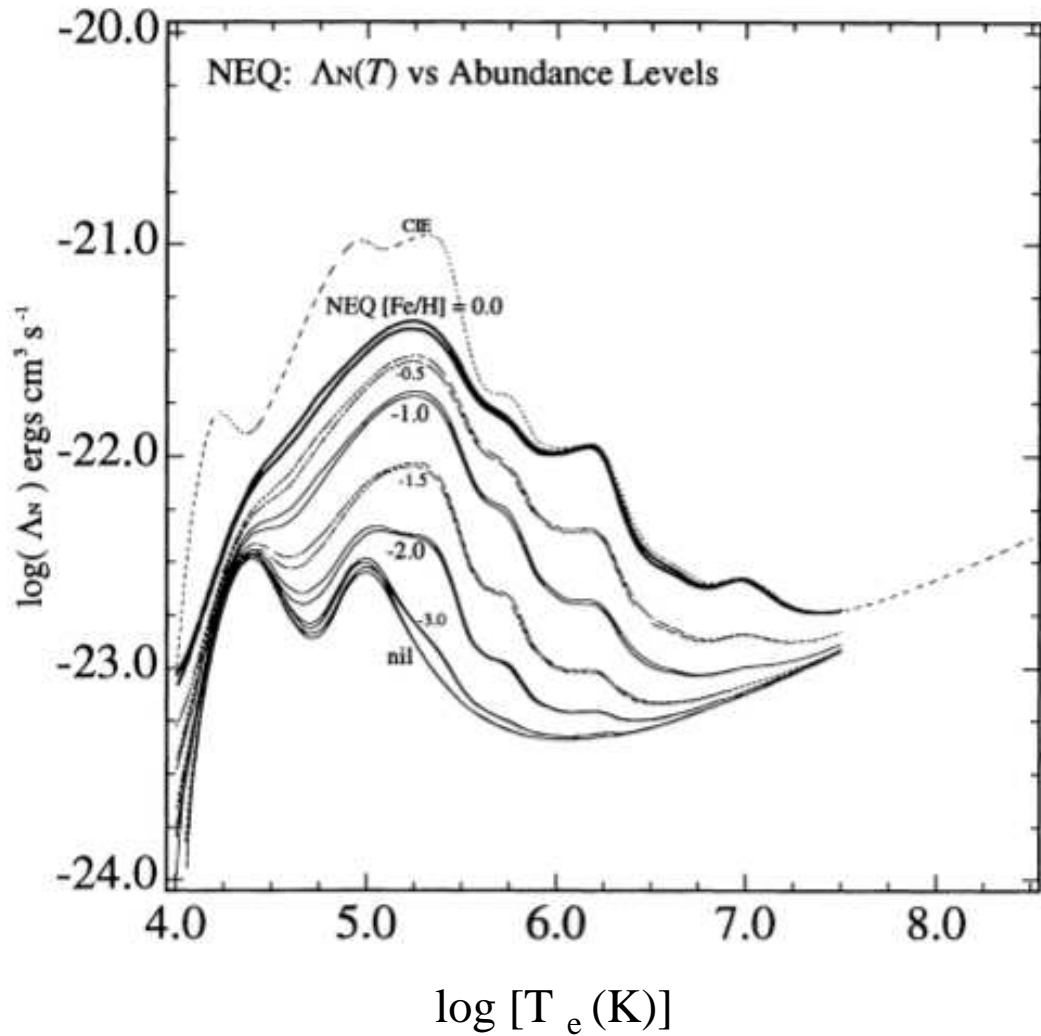


Figure 17. A graph showing the cooling function, Λ , as a function of effective temperature taken from Sutherland & Dopita (2003). The NEQ curves represent non-equilibrium cooling for gases of different metallicities and the dashed, CIE curve is the case of solar-metallicity gas in a state of collisional-ionization equilibrium.

HST line images were used to examine the emission and ionizational properties in the NW and SE regions near the location of the shock.

4.2.1. *Containment of the Synchrotron Nebula*

In regions where filaments form readily, or the shock speed is less than ≈ 195 km s⁻¹, the synchrotron nebula will be well contained because the filaments prevent it from expanding (Sankrit & Hester 1997). In contrast, regions with a high shock speed will not readily form filaments and the synchrotron nebula would be able to “break through” and expand outward unimpeded. We now examine the properties of the contact-discontinuity at high-resolution by using our [O III] line emission image and a *VLA* radio image of the Crab, which closely marks the location of the shock. Regions showing a strong coincidence between the boundary of [O III] and radio emission could be said to be forming filaments fast enough that the synchrotron nebula is well contained.

Figure 18 shows a high resolution *HST* [O III] image and a *VLA* radio image of the NW region of the Crab. Each tickmark represents 10'' (≈ 0.1 pc). It is clear from this figure that in the NW the synchrotron nebula has surpassed the distance of the [O III] emission by roughly 10'', indicating that the filaments are no longer forming here. Further evidence that the filaments are no longer forming is that the edge to the [O III] emission in this area arises from seemingly random clumps that are unconnected rather than coming from long, connected structures.

Regions where the edge of the nebula is closest to the explosion center (and pulsar) must have had slower shock speeds than regions where the edge of the visible

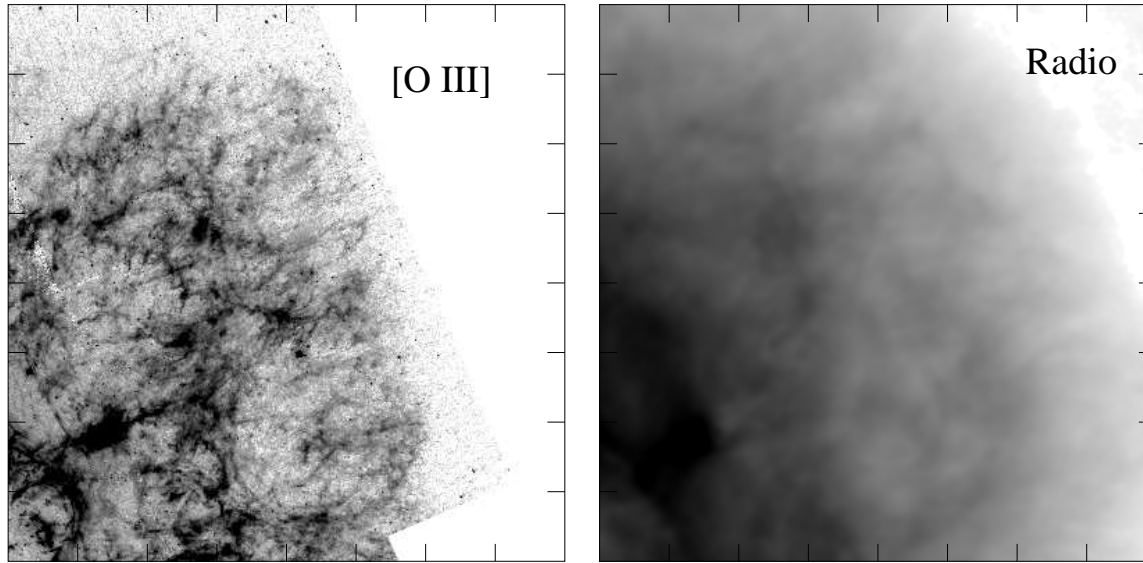


Figure 18. A comparison of the shock edge in the NW, shown in a *VLA* radio image (right) and the cooling region there, shown in [O III] (left). Each tick mark represents $15''$ (or about 0.15 pc.)

nebula is farther from the center. Since the nebula is in the form of an ellipsoid, the edge of the nebula along the semi-major axis of the nebula that is near due north and south remain the closest to the actual explosion center (see Figure 16). We expect the lowest shock velocities in these areas and filaments should form quickly behind the shock front. Figure 19 provides a high resolution *HST* [O III] image and a *VLA* radio image taken from the south edge of the Crab (where the edge is about 1.4 pc away from the explosion center). The [O III] emission has a clear, well-bounded edge and the filaments appear to be long, connected and continuous structures. The [O III] emission edge is almost exactly coincident with the radio edge, suggesting that the synchrotron nebula is well bounded by the filaments in this region. These observations support the idea that in the south the filaments are actively forming from cooled, post-shock gas that is continually collecting on the synchrotron nebula's surface providing resistance against expansion.

Figure 20 shows a high resolution *HST* [O III] image and a *VLA* radio image of the SE edge of the Crab. According to our three-dimensional model, this area of the nebula is the second farthest point from the explosion center (see Figure 16) and therefore we would expect that the shock here would represent an intermediate case between what we find in the NW (farthest from the explosion center) and the north/south regions (closest to the explosion center). The synchrotron nebula in the SE is seen within the boundary of the [O III] edge. We note that although filaments still continue to form, the shock may be reaching velocities high enough that the soon the post-shock gas will be too hot to form filaments. This is based on the filaments not

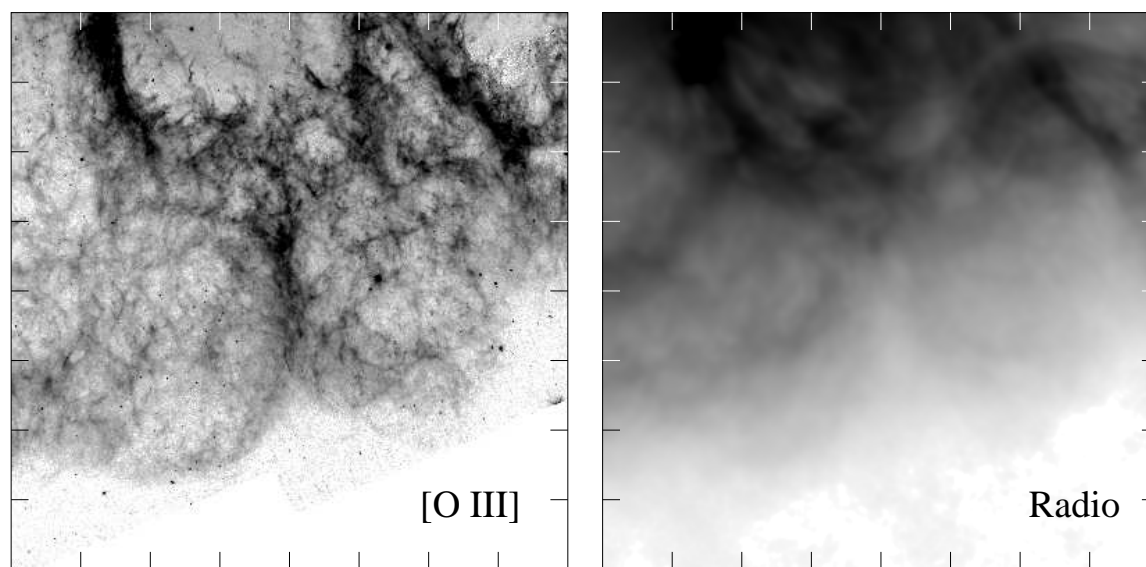


Figure 19. A comparison of the shock edge in the south, shown in a *VLA* radio image (right) and the cooling region there, shown in [O III](left). Each tick mark represents $15''$ (or about 0.15 pc.)

appearing to form a continuous edge as they do in the south, but rather appearing to break up. If this is the case, then the synchrotron nebula will begin pushing through these weak filaments to the point where it can break out and expand without the constraints of the dense filaments. The SE portion does, in fact, have the properties we would expect for a shock speed that is in between what we expect in the NW and south, and therefore we are confident that our three-dimensional distance model gives a representative distance estimate around the perimeter and hence a representative estimate for the differences in density and shock speeds around the perimeter of the Crab.

4.2.2. *An Asymmetry in the Ionization Structure of the Filaments*

Line profiles taken at the edge of the nebula all around the perimeter show a range of ionization states that can be attributed to variations in shock speeds. We chose to look at the edge of the nebula because the radial velocities are the lowest (expansion is mostly in the plane of the sky) and therefore the emission is well sampled by the *HST* filter bandpasses. Figure 21 shows locations where we measured line intensities of all three emission lines ([O III], [S II], and [O I]) to study their properties at the edge. The associated line profiles are in Figures 22 and 23, where distance = 0 represents the location of the profile on the outside of the nebula and larger distances are closer to the center of the nebula. The measured intensities are integrated totals along the width of the profiles using the flux calibrated *HST* images.

The regions where we believe the shock is propagating slow enough to form filaments— such as locations 1, 2, 5, and 6— show [O III] emission that has a steep

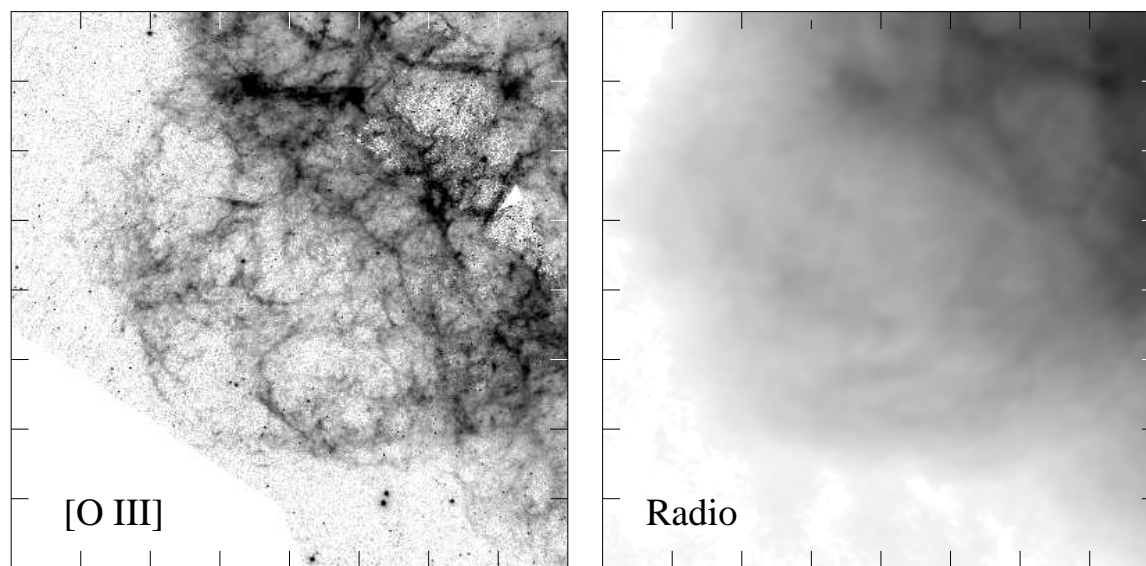


Figure 20. A comparison of the shock edge in the SE, shown in a *VLA* radio image (right) and the cooling region there, shown in [O III] (left). Each tick mark represents $15''$ or about 0.15 pc.

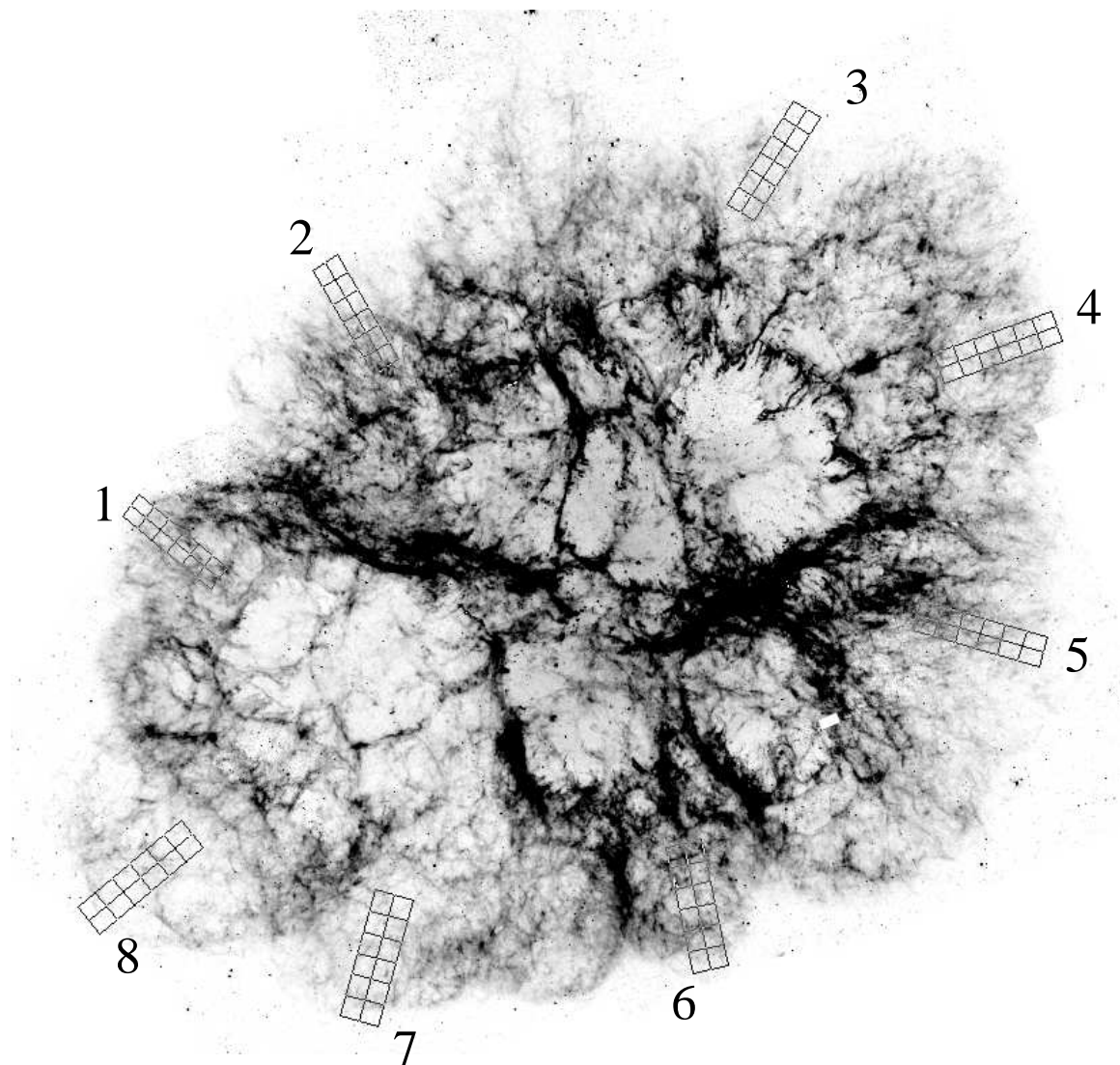


Figure 21. Locations where the line profiles shown in Figure 22 and Figure 23 were taken

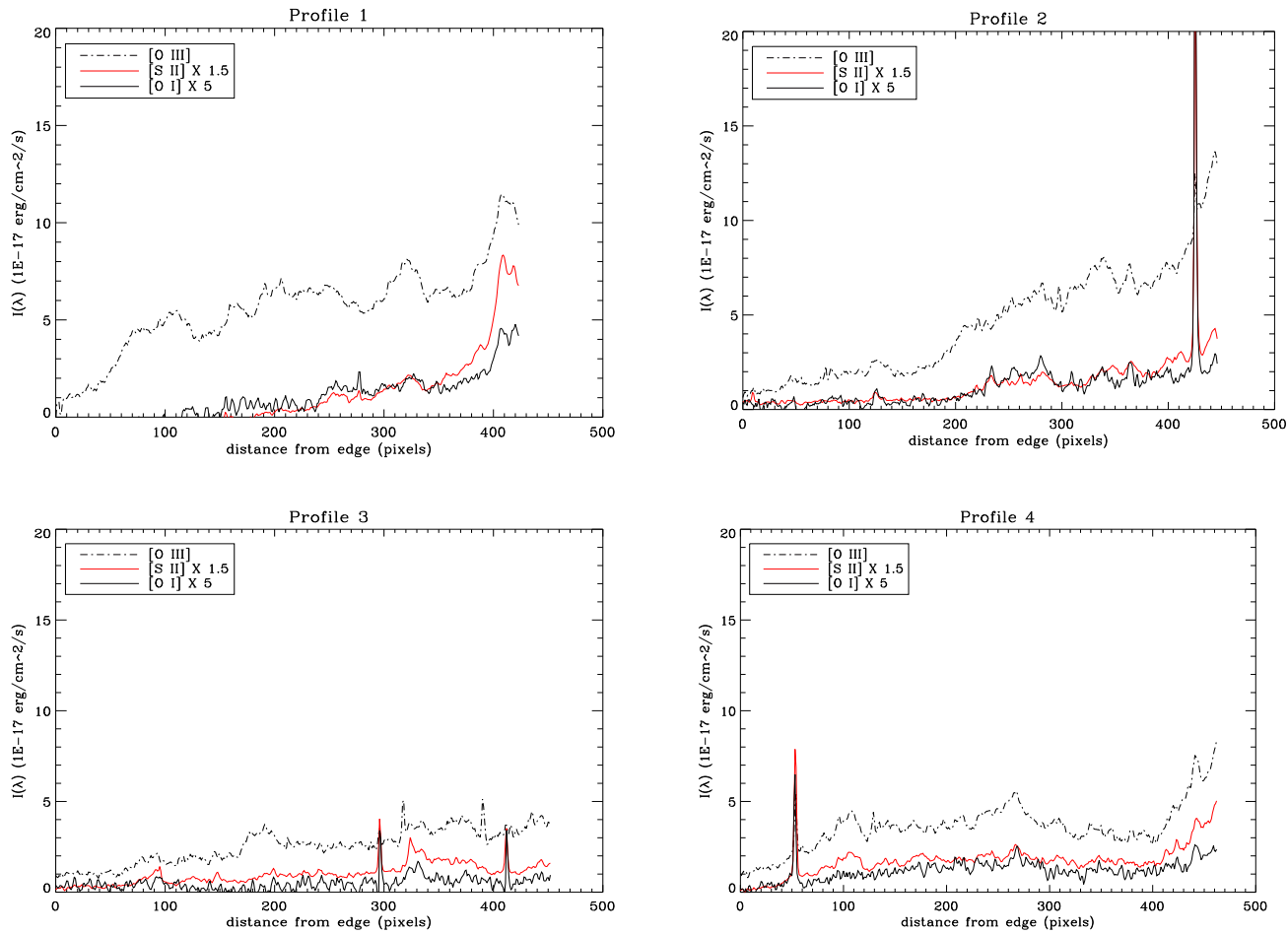


Figure 22. Line profiles taken at the corresponding locations in Figure 21 that show the emission line structure at the edge of the Crab Nebula with higher distances meaning that the emission is closer to the center of the nebula. Filaments are forming in regions where there are peaks in all three emission lines.

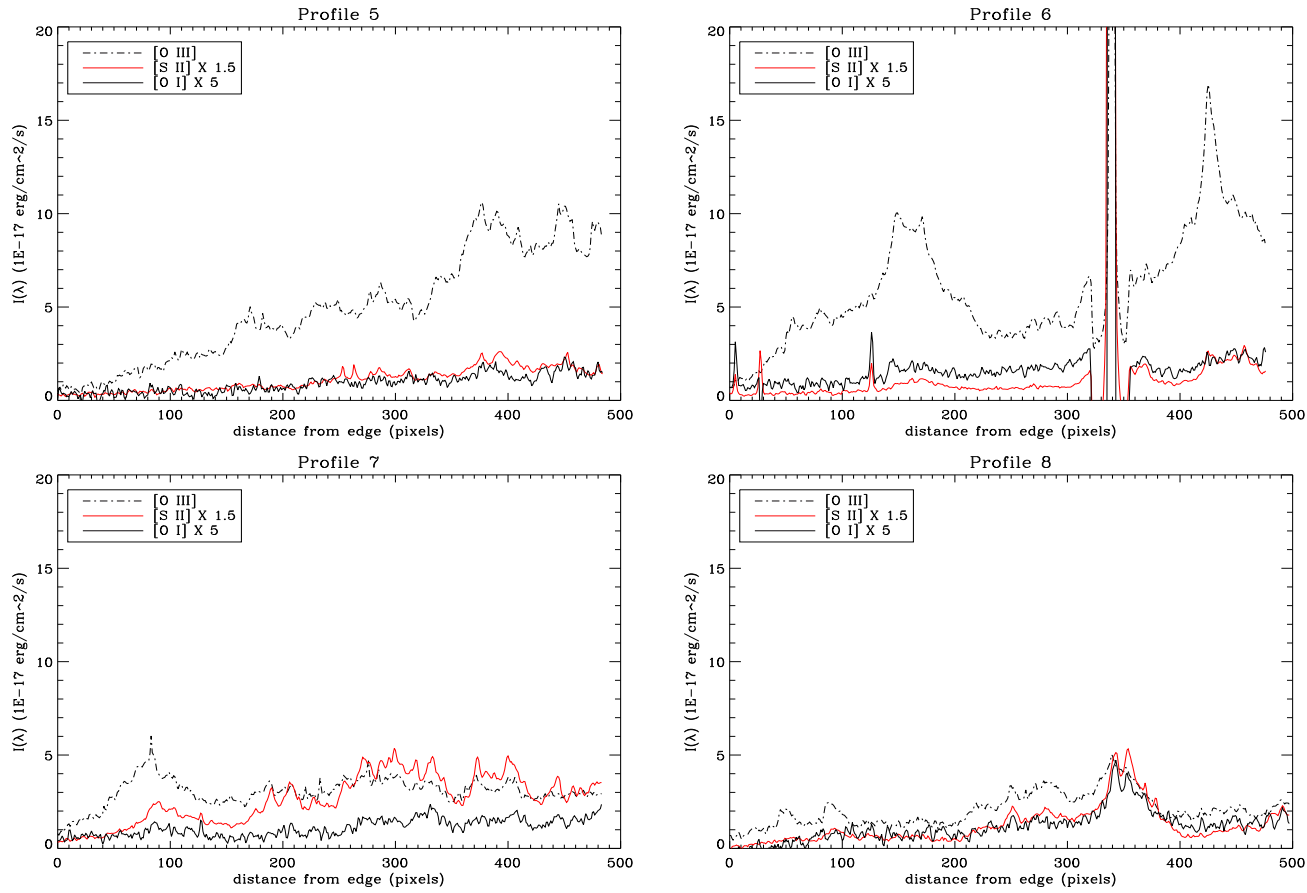


Figure 23. Line profiles taken at the corresponding locations in Figure 21 that show the emission line structure at the edge of the Crab Nebula with higher distances meaning that the emission is closer to the center of the nebula. Filaments are forming in regions where there are peaks in all three emission lines.

rise in intensity at the edge. [S II] and [O I] emission can be found successively farther in from the edge than the [O III]. In transitional regions, such as locations 7 and 8, the [O III] emission does rise (indicating that gas is cooling behind the shock), but the line intensity is less than what is found in the radiative regions. [S II] and [O I] appear farther in from the edge than [O III] and have lower line intensities than in regions where the shock is expected to have a lower velocity. We attribute the lower intensities of all three emission lines to the post-shock gas having lower densities and higher temperatures at locations 7 and 8 than in regions 1, 2, 5 or 6. Finally, in regions where the shock is propagating at speeds too high to form filaments in the cooling region, namely locations 3 and 4 in the northwest, we see the lowest [O III] line intensities and virtually no [S II] or [O I] emission. The lack of any intermediate-ionization lines or ground-state oxygen is due to the high post-shock temperatures. Radiative cooling compresses the gas, therefore gas can not cool quickly does not reach the densities necessary for these ionic species to exist. We suggest that the high post-shock temperatures are due to high shock speeds, which in turn occur when the shock is propagating into freely expanding ejecta with a lower density than the regions where the filaments form efficiently under the assumption that the pressure is the same everywhere around the perimeter.

4.3. Results

The observations of the Crab Nebula discussed here indicate that the shock speed varies around the perimeter of the nebula. This has led to a NW-SE asymmetry in the formation of filaments and the ionization properties of the post-shock gas.

We suggest these differences are attributed to variations in pre-shock ejecta density (Chapter 3). Since the pressure of the synchrotron nebula should be very similar between the NW and SE sides of the nebula due to the high sound speed of the relativistic plasma, it is the pre-shock ejecta density that determines the effective speed of the shock. We have shown with our 3-D model of the Crab that the density of the pre-shock ejecta in the NW is less than the pre-shock ejecta density in the SE because the ejecta density has a power-law fall-off that scales with distance from the expansion center, whereas the synchrotron nebula is more closely centered around the location of the pulsar. The NW transverse velocity of the pulsar has caused the synchrotron nebula to expand farther in the NW direction than the SE direction (with respect to the explosion center) and has caused an asymmetry to develop in the shock speed. In the NW, the shock is moving into less dense ejecta and therefore propagates faster in the NW than it does in the SE. We have provided evidence of this statement using the *HST* line emission mosaics and a *VLA* radio image (Bietenholz & Kronberg 1990) which show that the shock forms filaments readily around most of the nebula as the post-shock gas cools quickly via magnetic-dipole (forbidden) radiation. The density of the post-shock gas climbs and allows dense filaments to form, evident by the presence of intermediate- and low-ionization emission lines (Profiles 1, 2, 7 and 8 in Figures 22-23), which are indicative of shielding from the high-energy photons emitted via synchrotron emission.

In the SE, we believe the shock may be reaching the velocity at which the filaments cease forming. This statement is based on the observations that show a

clumpier, non-connected [O III] boundary and a larger gap between the [O III] and [S II] edge. The filaments show less intense line emission than in the south, indicating slower cooling times and, as a result, less dense filaments. Also, the synchrotron nebula is seen just beyond the edge of the [O III] emission and is likely breaking free of the confinement. This is explained by the results from Chapter 3; the SE region is the second farthest location from the expansion center therefore we would expect this to be the region of next-to-lowest density and next-to-highest shock speeds, after the NW.

The NW emission clearly shows that the synchrotron nebula extends well beyond the bounds of [O III] line emission (Figure 18). The post-shock gas in the NW has a very long cooling time, likely longer than the age of the remnant, and filament formation has ceased completely. Also, the [O III] line intensity of [O III] is much lower here than in any other region, indicating that the post-shock density is lower and/or the temperatures are much higher. There is no intermediate- or low-ionization gas at the edge of the nebula in the NW at all, supporting the idea that the post-shock temperatures are high and that filaments can not form dense structure that provide the shielding necessary for [O I] emission.

The distances from our 3-D model of the Crab, combined with our observational analysis, indicate that filaments can form when the shock is within about 1.6 - 1.7 pc of the explosion center. At larger distances, the ejecta densities become low enough and the shock becomes fast enough that the cooling times increase dramatically, and the filaments can no longer form. If no filaments form, the synchrotron nebula breaks

free. A precise distance where this transition would take place cannot be determined from our ellipsoid due to estimations in the boundary, axial tilts, and because it is likely impossible that the explosion produced a spherical shell of ejecta density with an identical density fall-off around the perimeter. However, the observations showing the coincidence of the [O III] edge and the radio edge indicate that the distance at the very tip of the SE edge may be at the threshold of filament formation. Our ellipsoidal model estimates the SE edge is about 2 pc away from the explosion center.

The main result of this analysis is that, collectively, the *HST* observations indicate that the shock is moving slower the closer it is to the explosion center. The pre-shock ejecta density decreases with distance from the explosion center, and since the pressure of synchrotron nebula that is driving the shock is relatively constant, then the shock must speed up as it propagates outward. The NW transverse velocity of the pulsar also plays a crucial role, because this motion has caused the nebula to expand farther from the explosion center in this direction. This means that the shock is currently propagating fastest in the NW. Since the nebula is modeled by an ellipsoid, the SE part of the nebula is the second farthest region and has the next highest shock speeds. The areas in between have the slowest shock speeds. The formation of filaments and their physical properties are important because the density of the gas contained in the filaments is what controls the development of Rayleigh-Taylor instabilities, which will be discussed in Chapters 5 and 6.

CHAPTER 5

A Theoretical Model for the NW-SE Asymmetry

As a means of providing context for our observations, and to interpret them, we want a theoretical model that predicts the physical conditions that we observe in *HST* observations of the Crab Nebula. Specifically, we would like to predict the time at which the R-T instability became dominant in the filaments and also the expected expansion rate for the shock front in both the NW and SE sides. As concluded in Chapters 3 and 4, the transverse velocity of the pulsar has caused the shock speeds to encounter lower density ejecta in the NW than in the SE. Due to the high sound speed of the synchrotron nebula plasma, the pressure around the edge is roughly the same everywhere, and therefore the shock speed is dependent on the pre-shock ejecta density according to $v_s \propto 1/\rho$. Higher shock speeds lead to higher post-shock temperatures of the ejecta which, in turn, affects the formation of filaments. H96 determined that it is the density of the filaments that dominates the formation of R-T fingers. We expect that we may predict that the effects of ejecta density variation with respect to the current pulsar location cause of the NW-SE asymmetry observed in the lengths and development of R-T fingers.

5.1. Existing Numerical Model of PWN and Ejecta

Jun (1998) has developed a model of the development of R-T fingers much like what we need to carry out the analysis discussed above. The model included a pulsar wind, freely expanding supernova ejecta, a supernova blast wave and a reverse shock. First, he determined the self-similar solution for a pulsar wind that is expanding into ejecta that has a density that decreases with radius, ($\rho \propto r^{-n}$) and a decreasing pulsar luminosity ($L \propto t^{-l}$). The expansion law for pulsar-wind bubble was determined

using the formula $r \propto t^{(6-n-l)/(5-n)}$, where n and l are the power-law indices for the expansion and luminosity, respectively.

Jun (1998) used the one-dimensional fluid equations (spherical coordinates) to determine the self-similar solution. Those equations are

$$\frac{\partial \rho}{\partial t} + v \frac{\partial \rho}{\partial r} + \rho \frac{\partial v}{\partial r} + \frac{2\rho v}{r} = 0 \quad (5.1)$$

$$\frac{\partial v}{\partial t} + v \frac{\partial v}{\partial r} + \frac{1}{\rho} \frac{\partial p}{\partial r} = 0 \quad (5.2)$$

$$\frac{\partial p}{\partial t} + v \frac{\partial p}{\partial r} + \gamma p \frac{\partial v}{\partial r} + \frac{2\gamma p v}{r} = 0 \quad (5.3)$$

where ρ is density, v is the outward radial velocity, t is the time since the supernova explosion, r is distance from the pulsar to the shock front, p is pressure in the pulsar wind, and γ is the adiabatic index of the pulsar wind plasma. In order to transform these equations into ordinary differential equations, Jun (1998) defined the following similarity variables:

$$\xi = \frac{r}{At^a} \quad (5.4)$$

$$\rho = t^{b-na} D(\xi) \quad (5.5)$$

$$v = aAt^{a-1} V(\xi) \quad (5.6)$$

$$p = a^2 A^2 t^{b-na+2a-2} P(\xi) \quad (5.7)$$

where A is a constant and a is the expansion parameter, $a = (6 - n - l)/(5 - n) = 1 + (1 - l)/(5 - n)$. In the equation for pressure above, b is an expansion factor defined by $b = n - 3$.

Since the ejecta surrounding the pulsar bubble is assumed to be expanding in time, no deceleration of the pulsar bubble is allowed. The acceleration (α) can be

determined from:

$$\alpha = \left. \frac{\partial v}{\partial t} \right|_{\xi=1} = a(a-1)At^{a-2}v(\xi) \quad (5.8)$$

and it is clear that the acceleration is positive for $a > 1$. Assuming a constant luminosity in time ($l = 0$), then $a = 1$ when $n = 3$, so that for acceleration to take place $n < 3$.

The fluid equations and similarity variables combine to yield the ordinary differential equations below:

$$\left(\frac{b}{a} - n + \frac{2V}{\xi} \right) D + (V + \xi) \frac{dD}{d\xi} + D \frac{dV}{d\xi} = 0 \quad (5.9)$$

$$\frac{(a-1)}{a} V + (V - \xi) \frac{dV}{d\xi} + \frac{1}{D} \frac{dP}{d\xi} = 0 \quad (5.10)$$

$$\left(\frac{b-2}{a} - n + 2 + \frac{2V\gamma}{\xi} \right) P + (V - \xi) \frac{dP}{d\xi} + P\gamma \frac{dV}{d\xi} = 0. \quad (5.11)$$

Jun (1998) integrated these differential equations from the shock front at the edge of the synchrotron bubble ($\xi = 1$) to the contact discontinuity by imposing the boundary conditions below:

$$D(1) = \frac{\gamma + 1}{\gamma - 1} \quad (5.12)$$

$$V(1) = 1 + \frac{\gamma - 1}{\gamma + 1}(c - 1) \quad (5.13)$$

$$P(1) = \frac{2}{\gamma + 1}(1 - c)^2 \quad (5.14)$$

where D, V and P are the density, volume and gas pressure, respectively. A value of $c = 0$ represents a shock moving into stationary medium, but generally $c = 1/a > 0$ [$a = (6 - n - l)/(5 - n)$], representing a shock propagating into expanding ejecta. The adiabatic index was taken to represent an ideal gas ($\gamma = 5/3$) because the shocked

ejecta (which exist in the region between the contact discontinuity and the forward moving shock) are fully dissociated, but not relativistic.

Jun (1998) used this self-similar solution to determine if the contact discontinuity would be subject to R-T instabilities. R-T instabilities require that there be a density difference between two fluids in contact, and an acceleration. The lighter fluid must be on the “bottom” side of the effective gravity vector (which points in the opposite direction of the acceleration). More precisely, the growth rate of the R-T instability is given by

$$\eta^2 = \frac{P}{\rho} \frac{\partial \ln P}{\partial \ln r} \frac{\partial \ln \rho}{\partial \ln r}, \quad (5.15)$$

which is real and positive only if $\partial \rho / \partial r$ and $\partial P / \partial r$ have opposite signs. The contact-discontinuity between the PWN and the shocked ejecta satisfy this condition; the shocked ejecta at the contact-discontinuity is much denser than the relativistic bubble that is accelerating it (Hester et al. 1996). We have shown above that acceleration of the pulsar bubble only occurs for values of $a > 1$, meaning the following must be true: $(6 - n - l) > (5 - n)$, or $l < 1$ ($L \propto t^{-l}$). When these criteria are met, the model predicted the formation of R-T fingers much like what we see in the Crab Nebula.

The model by Jun (1998) shows that as a_s , the expansion index of the shock front, increases beyond 1.0, the shell of shocked ejecta becomes thicker. In the self-similar solution, Jun (1998) modeled the additional effect of radiative cooling ($\gamma = 1.1$) and found that the thickness of the shocked ejecta was thinner, but an order of magnitude denser, than in the adiabatic case. This result suggests that in regions of the Crab Nebula where shock speeds are slower and the gas can cool on

timescales much shorter than the expansion time of the synchrotron nebula, we should see thinner and denser filaments. We will examine and discuss what our observations show in terms of the thickness and density of the Crab Nebula filaments in Chapter 6.

Jun (1998) also used two-dimensional analytical and numerical simulations to study the dynamical interaction between the pulsar wind and the ejecta. This model included the pulsar wind, the layer of shocked ejecta between the contact discontinuity and the shock (filaments), the freely expanding ejecta, and a reverse shock. He began the simulation early in the Crab Nebula's history by assuming a constant luminosity for the pulsar ($l = 0$, $L \propto t^{-l}$) where $L = 2\pi r^2(\rho v^3/2) = 1.0 \times 10^{40}$ erg s⁻¹ where r , ρ and v are the initial values of distance from the pulsar, local density and local velocity at one instant. The assumed luminosity is high compared to the current measured luminosity of the pulsar (1.0×10^{38} erg s⁻¹), but is consistent with the average luminosity being $\approx 1.2 \times 10^{39}$ erg s⁻¹ over the lifetime of the remnant as inferred from the observed decrease in luminosity with time ($L_{\text{spin}} \approx 5 \times 10^{38}$ erg s⁻¹) (Hester 2008). Jun (1998) assumed $r = 0.1$ pc and a gas density for the wind equal to 1.67×10^{-24} g cm⁻³, implying an initial pulsar wind velocity of $v \approx 22,000$ km s⁻¹. Initially, the ejecta was constrained to have a velocity of 500 km s⁻¹ at a distance of 0.1 pc, with velocities at different locations scaling linearly with distance from the pulsar (homologous expansion). This model assumed a constant pre-shock ejecta density (1.67×10^{-22} g cm⁻³) at all r ; however the ejecta density effectively decreases in time due to expansion.

The one-dimensional simulations by Jun (1998) correctly predict a wind termination shock near the pulsar, a contact discontinuity between the pulsar wind bubble and the shocked ejecta, and a forward shock driven by the pulsar bubble. Initially, the shock velocity is much greater than the velocity of the expanding ejecta (see initial conditions above). This was termed the “stationary medium stage” by Weaver et al. (1977) because the velocity of the ejecta can be neglected. In this stage, $r_{\text{shock}} \propto t^{3/5}$. As time goes on and the shock encounters more and more ejecta, the shock velocity decreases. The simulations show that once the shock velocity becomes comparable to the velocity of the freely expanding ejecta, the effect of decreasing ejecta density becomes important and the shock accelerates ($a > 1$). At this time the nebula enters what Weaver et al. (1977) called the “moving medium phase” and the contact discontinuity becomes very distorted due to the growth of R-T fingers. As the shock continues to accelerate, the thickness of the filaments increase and the R-T fingers continue to grow as the gas from the post-shock flow pours into the fingers along the effective gravity vector (toward the direction of the pulsar). The filamentary gas flowing into the fingers compresses the gas at the tips and they become more and more dense in time. The Jun (1998) models indicate that R-T fingers begin growing within a few hundred years of the explosion but that period of fastest growth occurs between $t = 1000 - 2000$ years; during this time, the tips of the fingers reach densities that are up to 10 times greater than the gas in the post-shock region. Over time, the tips of R-T fingers are disrupted by shearing forces (Kelvin-Helmholtz instabilities), indicated by a flattened tip that may begin to bend backward at the edges. After

about 2000 years, the density of the pre-shock gas is low enough that the mass fluxes of newly shocked material is less than the mass flux into the fingers, and the growth of the fingers slows dramatically while the thickness of the filaments increases.

According to these results, we recognize that we are observing the Crab at a special time during the interaction of the PWN and the stellar ejecta. The R-T instability is prevalent throughout the Crab (Hester et al. 1996), which is consistent with it being just under 1000 years old. The model predicts that the R-T instabilities should be growing most efficiently during this time period. Further, Jun (1998) determined that at $t \approx 1000$ yr the fingers become decoupled from the shock front in that they expand more slowly. The simulation predicts an asymptotic limit for the power-law index of expansion for the fingers to be $a_f = 1.04$, which is slightly higher than what is expected for free expansion but considerably less than the asymptotic limit for the shock, $a_s = 1.2$ for the self-similar solution. It is noted, however, that the Jun model only reached $a = 1.157$ for a time of 4000 years after the explosion, which is four times the age of the Crab.

5.2. Limitations of the Existing Model

The canonical case considered by Jun (1998) provides many useful insights but leaves the most physically relevant cases unexplored. The assumption of a constant luminosity ($l = 0, L \propto t^{-l}$) throughout time is incorrect. The Jun (1998) model assumes a luminosity that is two orders of magnitude greater than what the current luminosity is measured at in order to simulate earlier times in the nebula's history; however, the luminosity is known to be decreasing in time as the pulsar's energy

is deposited into the synchrotron nebula. The pulsar has lost $\approx 3.6 \times 10^{49}$ ergs of energy since its formation, mostly to the relativistic wind (Hester 2008). A decreasing luminosity in time is accommodated in the Jun (1998) model as value $l > 0$ which will in turn impact the rate of expansion since $r \propto t^a$ and $a = (6 - n - l)/(5 - n) = (1 - l)/(5 - n) + 1$. If the luminosity decreases in time, then the value of a is smaller and the expansion is slower. We would expect, then, that the actual value of r at a given time may be smaller than what Jun (1998) predicts on the basis of $l = 0$.

Jun (1998) also did not include magnetic fields in the numerical simulations of the pulsar wind and the ejecta. As discussed in Chapter 1, magnetic fields are known to be significant in the Crab Nebula in both the inner synchrotron nebula (Michel et al. 1991) and in the filaments (Hester et al. 1996). Including magnetic fields in the calculations would affect many of the parameters. For example, it is likely that if magnetic tension within the filaments were taken into account, the R-T instability would occur later in time because the magnetic tension has the effect of keeping the interface at the contact-discontinuity stable (Hester et al. 1996). In addition, the filaments are sufficiently ionized so that they “freeze in” magnetic flux, and when the R-T fingers grow the magnetic field lines bend to conform to the shape of the R-T finger (Hester et al. 1996). The field lines act much like a series of rubber bands being stretched and that can not cross over one another. The magnetic forces keep the fingers attached to the overlying filaments making them less subject to K-H instabilities or detaching from the overlying filaments altogether (Hester et al. 1996). We expect that the magnetic field lines stretching along the contours of the R-T

fingers and back up through the filaments will keep the expansion rate of the R-T fingers more closely coupled to the expansion of the outer filaments than the analysis of Jun (1998) would suggest. The overall effect of magnetic fields is to cause the fingers to form later in the expansion history, grow and stay attached to the filaments for a longer time period, and cause the finger to expand at a velocity that is more like the velocity of the filaments than what Jun (1998) predicts.

The two-dimensional Jun (1998) model did not include the effects of radiative cooling in the post-shock gas, which is also known to occur in the Crab (Sankrit & Hester 1997). Where radiative cooling is important, the filaments are more compressible, and should be thinner and denser than in areas of the nebula where radiative cooling is not important. Jun (1998) discussed these effects in the context of his self-similar solution, but does not take this into account in the numerical models involving R-T development. We assume that higher densities would shorten the time needed for the R-T instability to initiate because the density in the filaments would reach the critical density necessary for the instability to take hold earlier than what the above model predicts. The magnetic tension would have to be overcome though, and it is unclear from the existing models which of the competing effects - filament density or magnetic tension - has the greater effect on the timing of R-T instability development.

Finally, Jun (1998) assumed a uniform density profile ($n = 0$) for the expanding ejecta and this is a very unlikely scenario. A better model of the Crab would involve freely-expanding ejecta that become less dense with distance from the expan-

sion center; in that case, the shock front would accelerate faster and likely cause R-T fingers to develop at earlier times ($t < 1000$ yr). A decreasing ejecta density profile ($n > 0$) could also limit the duration of R-T finger growth compared to what the model by Jun (1998) predicts because the shock would transition from the stationary phase to the moving medium phase to the self-similar phase ($r_{\text{shock}} \propto t^{6/5}$, $a = 1.2$) faster. The mass flux into the filaments and hence into the fingers would be less in the $n > 0$ case, and this could also shorten the duration of R-T finger growth. If this is the case, then we may expect to see shorter fingers in the Crab Nebula than what the Jun (1998) model predicts.

5.3. Applying the Existing Model to the Crab Nebula

The Jun (1998) model is very useful but is not directly applicable to the Crab Nebula without correcting for some of the caveats discussed above. Here we describe modifications necessary to apply it to the Crab Nebula specifically. A major goal of this dissertation is to evaluate the difference in the expansion rates between the NW and SE sides of the nebula which means we need to evaluate separate values of a in the equation $r \propto t^a$ at these two locations. Images of the Crab Nebula clearly indicate that the nebula is not circular but rather elliptical in shape (see Chapter 3). The model by Jun (1998) assumes a circular PWN with spherically symmetric ejecta and a stationary pulsar. Here we explain how we can take that model and include the transverse velocity of the pulsar and the distribution of the freely expanding ejecta around the expansion center.

The first correction that must be made accounts for the transverse velocity of the pulsar towards the NW. The pulsar's motion toward the NW since the time of the explosion has caused the nebula to expand faster in the NW direction. At any given instant in time, though, the velocity of the pulsar is irrelevant compared to the velocity of the expanding PWN. The plasma in the synchrotron nebula is moving relativistically so that the 120 km s^{-1} motion of the pulsar has virtually no effect on the pressure at the edge, which is driving the shock front. Using the relationship that $r \propto t^a$, then the PWN will have an instantaneous outward velocity that follows from

$$v_{\text{PWN}} = \frac{dr_{\text{PWN}}}{dt} = at^{a-1} = \frac{ar_{\text{PWN}}}{t} \quad (5.16)$$

or

$$a = \frac{v_{\text{PWN}}t}{r_{\text{PWN}}} \quad (5.17)$$

where r_{PWN} is defined as the distance from the pulsar to the edge of the PWN since the expansion of the PWN is dependant on the location of the pulsar.

In the frame of the shock, the shock speed at any location around the perimeter can be defined as $v_s = v_{\text{PWN}} - v_{\text{ej}}$, or the difference between the expansion of the PWN and the velocity of the freely expanding ejecta (Sankrit & Hester 1997). Assuming a strong shock, it follows then that $P_{\text{PWN}} = \rho_{\text{ej}}v_s^2 = \rho_{\text{ej}}(v_{\text{PWN}} - v_{\text{ej}})^2$.

5.3.1. Predicting an Asymmetrical Rate of Expansion

Now if we move to the pulsar's frame of reference, the expansion of the PWN will appear to propagate more slowly in the NW direction than the SE direction due to the pulsar's transverse velocity. In the NW, we define that speed as $v_{\text{PWN,NW}} = v_{\text{ej,NW}} + v_{\text{s,NW}} - v_p$ where now the pulsar's motion with respect to the approximate

location of the explosion is taken into effect. Similarly, in the SE we have $v_{\text{PWN,SE}} = v_{\text{ej,SE}} + v_{\text{s,SE}} + v_{\text{p}}$.

If we assume the freely expanding ejecta are expanding homologously away from the location of the explosion, then at any point in time we can define $t = r_{\text{rmE}}/v_{\text{ej}}$. Substituting this value and the values solved above for velocity into the equation for the expansion index of the PWN, we find that in the NW:

$$a_{\text{NW}} = \frac{r_{\text{E,NW}}}{r_{\text{p,NW}}} \left[1 + \frac{v_{\text{s,NW}} - v_{\text{p}}}{v_{\text{ej,NW}}} \right] \quad (5.18)$$

and in the SE:

$$a_{\text{SE}} = \frac{r_{\text{E,SE}}}{r_{\text{p,SE}}} \left[1 + \frac{v_{\text{s,SE}} + v_{\text{p}}}{v_{\text{ej,SE}}} \right]. \quad (5.19)$$

These equations for the expansion index include both the transverse velocity of the pulsar and the distribution of the freely expanding ejecta around the location of the explosion. The results of our 3-D ellipsoid distances are that $r_{\text{p,NW}} = 2.2$ pc, $r_{\text{E,NW}} = 2.5$ pc, $r_{\text{p,SE}} = 2.1$ pc, $r_{\text{E,SE}} = 1.8$ pc. The values for the distance from the location of the explosion to the freely expanding ejecta (r_{E}) can be used to determine v_{ej} by knowing the time between the explosion and the VLA radio observations (used to determine the edge of the ellipsoid) is 944 years. This results in $v_{\text{ej,NW}} \approx 2500$ km s⁻¹ and $v_{\text{ej,SE}} \approx 1900$ km s⁻¹. The transverse velocity of the pulsar is the motion viewed from earth, or the motion in the plane of the sky. To take into account the tilt of the nebula, we divide the measured transverse velocity by $\cos 30^\circ$ to arrive at $v_{\text{p}} = 140$ km s⁻¹.

The speed of the shock can not be directly determined from our observations. We can estimate the velocity of the shock, though, by assuming that the pressure of

the PWN is the same at both the NW and SE sides of the nebula (due to a high sound speed) and then using the ratio of the shock velocities at both ends as follows:

$$\frac{v_{s,NW}}{v_{s,SE}} = \frac{\rho_{SE}}{\rho_{SE}} = \frac{r_{E,NW}^{n/2}}{r_{E,SE}} \quad (5.20)$$

where we have assumed that the ejecta density fall-off is $\rho \propto r_E^{-n}$.

Unfortunately, the power-law index for ejecta density, n , has not been determined for the Crab Nebula. Mioduszewski et al. (2001) modeled the radio emission of a young Type II supernova remnant, SN 1993J, to infer the ejecta density power-law fall-off. Simulations of the hydrodynamics and radiative transfer predict that the density goes as $r^{-1.7}$ for SN 1993J. This particular supernova progenitor was likely more massive than the progenitor of the Crab. Stancliffe & Eldridge (2009) used a stellar evolutionary code to determine that the progenitor mass of SN1993J was between 15 - 17 M_\odot . This star was also part of a binary system. The Crab Nebula progenitor, however, was believed to be between 8-13 M_\odot (Hester 2008). Still, we will take the density fall off value of 1.7 to be a reasonable estimate for the ejecta density power-law fall off and this results in $v_{s,NW}/v_{s,SE} = 1.32$. Shock models of the Crab Nebula by Sankrit & Hester (1997) that included a shock moving into freely expanding ejecta showed that shock velocities of $v_s = 130 - 150 \text{ km s}^{-1}$ resulted in emission line intensities that are in agreement with ground-based observations. They also found that shock speeds about $\approx 195 \text{ km s}^{-1}$ were so high that filaments could no longer form in the age of the remnant. The implication of shock speeds greater than this value is that the filaments can not form. If there are no filaments, then the synchrotron nebula is not confined any longer and “breaks free”. This is precisely what

is seen in the NW part of the remnant. Values of $v_{s,SE} = 150 \text{ km s}^{-1}$ and $v_{s,NW} = 200 \text{ km s}^{-1}$ agree with our calculations for the ratio of shock speeds, the observational evidence presented here with regards to filament formation, and the results of Sankrit & Hester (1997) shock models of the Crab Nebula's filaments.

Now we can determine what we believe the expansion index should be in both the NW and SE sides of the nebula as follows:

$$a_{NW} = \frac{2.5\text{pc}}{2.2\text{pc}} \left[1 + \frac{200\text{kms}^{-1} - 140\text{kms}^{-1}}{2500\text{kms}^{-1}} \right] = 1.164 \quad (5.21)$$

and in the SE:

$$a_{NW} = \frac{1.8\text{pc}}{2.1\text{pc}} \left[1 + \frac{150\text{kms}^{-1} + 140\text{kms}^{-1}}{1900\text{kms}^{-1}} \right] = 0.988. \quad (5.22)$$

Varying the input values for the shock speed by $\pm 10\%$ changes the expansion indices by about ± 0.01 in the NW and ± 0.008 in the SE. This means that within the expected shock velocities predicted by the Sankrit & Hester (1997) models, we would not expect the value of a to change from these calculated values in any significant way. If we change the distances to the pulsar and the expansion center by $\pm 10\%$, then the values of a change by ± 0.03 in the NW and ± 0.003 in the SE. Our assumed value of n may also be incorrect, however allowing for different values would only serve to make the expansion indices of the NW and SE more asymmetrical, while still having values within those above plus or minus the possible errors quoted here. We believe our largest uncertainty is in the value of n , which may be closer to -4 (Sollerman et al. 2000). Keeping $v_{s,SE}$ constrained to 150 km s^{-1} and changing the density power law to $n = -4$ changes a_{NW} to 1.20, which is very close to the asymptotic limit proposed

by Jun. We infer from these results that, with respect to the pulsar where $r_p \propto t^a$, $a \approx 1.164 \pm 0.036$ in the NW and $\approx 0.988 \pm 0.036$ in the SE. Per the Jun model, which determined that acceleration occurs when $a > 1$, this means that in the SE the PWN is not accelerating outward but is expanding outward at a constant speed away from the pulsar. In the NW, however, the PWN is accelerating away from the pulsar. In other words, the PWN has expanded farther in the NW direction than it would have if the pulsar had no transverse velocity. What we conclude from this model is robust considering the agreements between the shock model by Sankrit & Hester (1997), ground-based observations, and the corrections we have made to the Jun (1998) model to fit the Crab.

5.3.2. *Predicting the Asymmetry of R-T Fingers*

As discussed in Chapter 1, in order for R-T fingers to grow there must be acceleration. What we conclude by our calculations above is that we expect there to be acceleration in the NW, but in the SE we expect the interface has the conditions that acceleration is marginal. The Jun (1998) model concluded that, when there is acceleration of the contact-discontinuity, R-T fingers will grow. What this means is that we would expect the R-T instability to be active in the NW and only marginally active in the SE. The observations presented here do show a strong NW-SE asymmetry in the lengths and development of the R-T fingers that can be explained, now, simply in terms of the pulsar's transverse velocity and the overall effect that has on the expansion of the synchrotron nebula.

5.3.2.1. Ages of R-T Fingers

Our interpretation of the expansion index, a , can be extrapolated in time to predict the future evolution of the nebula and likewise the history of the R-T instability. We expect that the pressure in the nebula is decreasing in time, however if we project the expansion index in a small increment in time, such as 100 years, we will assume that the pressure of the synchrotron nebula is equal to the pressure today. A schematic of the expansion in the NW 100 years in the future and the variables that follow are shown in Figure 24. In Figure 24, E represents the approximate location of the explosion and P_o is the location of the pulsar today.

First, we define $(r_{P,E})_o = 0.3$ pc, which is the distance between the pulsar and the explosion center at this point in time, as determined from the distance between R_E and R_P in the 3-D ellipsoid. Since the pulsar has a transverse velocity (assumed constant) of 140 km s^{-1} , then in 100 years time the pulsar will move about $v_p \Delta t = 0.014$ pc along the long axis of the nebula.

The expansion of the PWN away from the explosion center in the NW, 100 years from now, is defined by $r'_E = r_{E,NW} + v_{PWN,NW} \Delta t$ where $v_{PWN,NW} = v_{ej,NW} + v_{s,NW}$ and using the values above this gives $r_{E,NW} = 2.78$ pc. The distance of the pulsar to the edge of the PWN can be determined from $r_{P,NW} = r'_{E,NW} - (r_{P,E})_o + v_p \Delta t = 2.466$ pc. The density of the pre-shock ejecta is $\rho'_{NW} = \rho_{o,NW} (r'_{E,NW} / r'_{P,NW})^{-1.7} = 0.83 \rho_{o,NW}$. The shock velocity is then determined by $v'_{s,NW} = (\rho_{o,NW} / 0.83 \rho_{o,NW})^{0.5} v_{s,NW} = 220 \text{ km s}^{-1}$. The freely expanding ejecta velocity is assumed to be expanding homologically and therefore $v'_{ej} = v_{ej,NW} (r'_{E,NW} / r'_{P,NW}) = 2780 \text{ km s}^{-1}$. Using these values

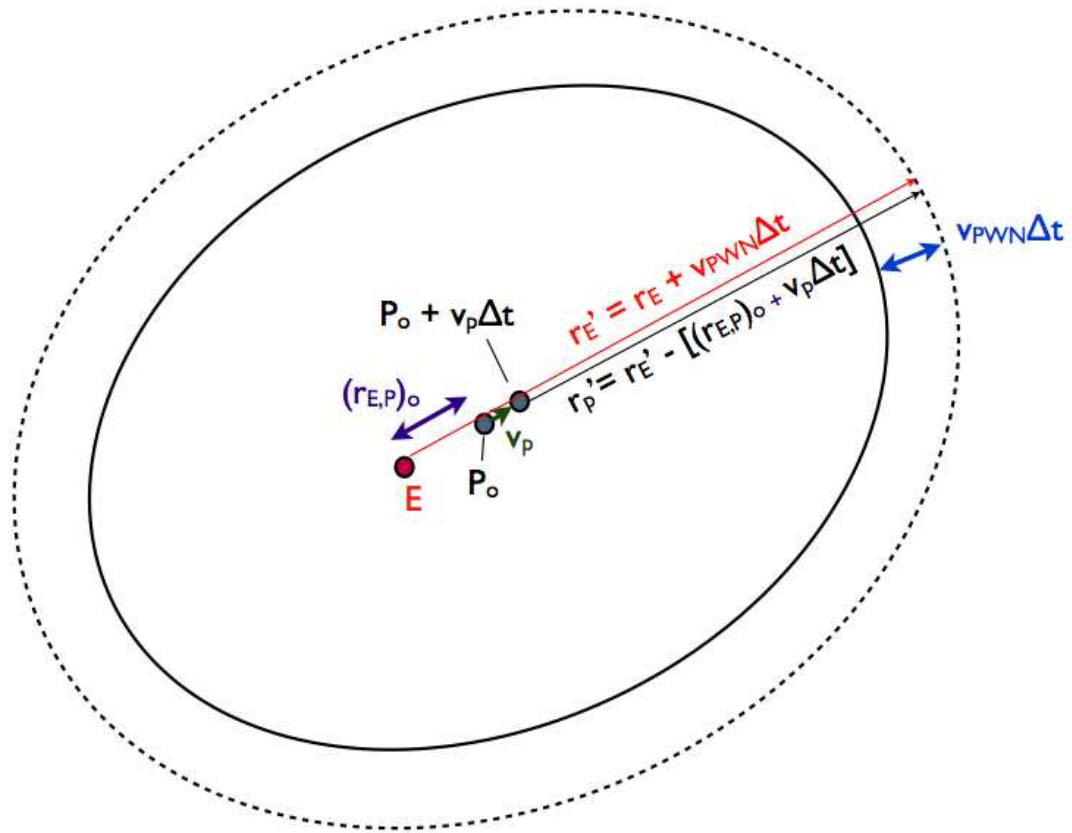


Figure 24. A schematic showing the projected evolution of the nebula in 100 years and the variables used to determine how the index of expansion, ‘a’ will change. This schematic projects the nebula 100 years into the future with quantities relevant for the NW. This image is not to scale.

in the equation for the expansion index, we estimate that in the NW a will slightly decrease to a value of 1.163 in the next 100 years. We can follow similar arguments to determine the value of a 100 years in the past. Our projections for both the NW and SE are presented in Table 5.

Table 5
Projection of the expansion index, a , ± 100 years in the
NW and SE.

Variable	NW	NW	NW	SE	SE	SE
	$(t_o - 100)$	(t_o)	$(t_o + 100)$	$(t_o - 100)$	(t_o)	$(t_o + 100)$
r_E (pc)	2.22	2.5	2.78	1.59	1.8	2.00
r_p (pc)	1.93	2.2	2.47	1.89	2.1	2.31
v_s (km s ⁻¹)	181	200	220	135	150	164
v_{ej} (km s ⁻¹)	2220	2500	2780	1672	1900	2111
ρ (ρ_o)	1.22	1.00	0.83	1.23	1.00	0.84
a	1.169	1.164	1.163	0.980	0.987	0.990

We find that in the NW, the expansion index is decreasing slowly in time. This indicates that the nebula will not expand outward as quickly as it has in the past, and as a result we predict that the R-T instability will be less and less effective as time goes on and in some instances has ceased completely since filaments can no longer form. However, in regions where the nebula continues to accelerate and until the expansion index drops below 1, the conditions are met for R-T fingers to develop. At

the same time, the instability was likely more effective in the past, again supporting the idea that the R-T fingers would have begun growing in the NW some time ago. A precise time can not be determined from these calculations because the pressure would not have been the same in the past as it is today (it would have been higher). However, we strongly argue that the instability occurred in the NW more than 100 years ago and throughout that time the fingers have continued to grow.

In the SE, our calculations show that in the past, the PWN was *not* accelerating, and that in the next 100 years the boundary will be increasing in distance from the pulsar faster than the rate it is expanding right now. The value we calculate for a is increasing in time in the SE, therefore we believe that the R-T instability has only recently become effective in the SE. These fingers are therefore young, and would not have had the time that the NW fingers have had to collect a lot of dense filamentary material and grow to the same lengths as the fingers in the NW. However, since the value of a is increasing in time, we predict that the instability will become more effective, and the R-T fingers will grow and develop in the SE during at least the next 100+ years, perhaps only reaching the most active stage of development in the future.

5.4. Results

We have used our observations to show that the transverse velocity of the pulsar may cause the NW-SE asymmetry we see in the R-T fingers. The motion of the pulsar has effectively carried the synchrotron nebula in the NW direction. The consequence of this motion, as predicted by using the expansion index a where $r \propto t^a$, is that

the PWN is accelerating in the NW direction but is only marginally accelerating in the SE. Acceleration of the contact-discontinuity is a necessary component in the development of the R-T instability. When we project the value of a in time, we predict that the expansion index will slowly decrease in time in the NW and slowly increase in time in the SE. This means that the R-T instability will become less effective in the NW direction in time (R-T fingers will slow in their growth) whereas in the SE we predict the R-T growth will become more dominant than it's been in the past. In the next chapter, we present observational evidence of a NW-SE asymmetry in the R-T finger development that supports these results.

CHAPTER 6

An NW-SE Asymmetry in the Filaments and R-T Fingers

6.1. Introduction

The *HST* emission line observations of the Crab in [O III], [S II], and [O I] show an obvious NW-SE asymmetry in the length, development, and separation of R-T fingers; long, well-developed fingers are prevalent in the NW quadrant of the Crab but virtually no where else in the nebula. Here, we combine models of the formation of the R-T instability (Hester et al. 1996), photoionization of the filaments (Sankrit et al. 1998), and the interaction of the PWN with the ejecta Jun (1998) with our *HST* mosaics to provide a reasonable explanation for why this asymmetry exists. According to the work by Hester et al. (1996), a difference in filamentary density would likely give rise to a difference in the development of R-T instabilities. Hester et al. (1996) was the first to do a quantitative analysis of the growth rate and characteristic wavelengths of magnetic Rayleigh-Taylor instabilities in the Crab Nebula. They used previously published values for the ejecta density and expansion velocities to quantify the growth rate and characteristic wavelength that would be expected for those conditions. Their model explains all of the various morphological properties of the filaments by differences in filamentary density at the contact-discontinuity. The filamentary density, ρ , is defined to be the density of gas in a filament composed of shocked ejecta, and this density is much greater than the density in the synchrotron nebula. The behavior of the filaments changes as ρ exceeds a value $\rho_{\text{crit}} = B^2/(g\lambda)$, where λ is the wavelength of the instability and g is the acceleration of the contact-discontinuity. The R-T instability is most effective when g and λ are large. In the Crab, though, we assume that both of these parameters

do not change much in time and so it is the density that the most dominating factor in driving the R-T instability. Hester et al. (1996) assumed a magnetic field strength ($600 \mu\text{G}$) and λ and found that filaments with densities below the critical value, about $170 \text{ atoms cm}^{-3}$, will have a stable interface. Near the critical density ($\rho/\rho_{\text{crit}} \approx 1$), R-T instabilities develop but the magnetic field is stretched along the length of the fingers and prevents any other instabilities from taking place. At even higher densities ($\rho/\rho_{\text{crit}} > 1$), the instability begins acting as it would if it were non-magnetic and Kelvin-Helmholtz (K-H) instabilities (characterized by flattened tips and vortices) can begin to disrupt the tips of the fingers due to shearing forces of the synchrotron nebula. When $\rho/\rho_{\text{crit}} \gg 1$, it is also possible for the finger to fragment, leaving a sphere of dense gas surrounded by synchrotron emission.

The strength of the emission lines in a R-T finger can be used to infer relative densities; higher emission from a tracer implies more atoms in that ionization state radiating at that wavelength. Hester et al. (1996) found that the brightness and ionization structure of the R-T fingers vary systematically with the morphology. R-T fingers having a low surface brightness (low density) are highly ionized, showing little or no emission from low-ionization lines and tend to be in the magnetically dominated regime of the instability. The R-T fingers that are most dense (highest surface brightness) are no longer dominated by the magnetic field and show a stratified ionization structure, with the tips of the fingers having [O III] on the outside, [S II] in an inner shell, and [O I] in the cores. This stratification is due to the synchrotron radiation being absorbed by the outer layers of the finger, leaving the inner gas

shielded and at densities and temperatures that are conducive to atoms that emit low-ionization emission lines.

Sankrit et al. (1998) constructed photoionization models to study the morphological and ionizational structure of the filaments using *HST* observations taken in the NW quadrant of the Crab Nebula. The model used cylindrically symmetric filaments and had three input parameters: density structure (quadratic core with exponential tail), incident flux, and elemental abundance. Varying these three parameters alone, Sankrit et al. (1998) were able to match the observed properties of three filaments. They determined that the high-ionization emission is much more diffuse than low-ionization emission, with the [O I] emission coming from dense filaments with scales less than 1'', while [O III] emission arose from scales larger than this. The observations also showed that there is a wide range in the distribution of the emission — all lines can be found in the same compact filamentary structures or they can be isolated such that the cores of the filaments contain low-ionization lines while the outer parts have only high-ionization emission. The amount of high-ionization emission with respect to low-ionization emission increased as the size of the filament increased, meaning that larger filaments are less dense and shielding is less effective. The Sankrit et al. (1998) models of cylindrical R-T fingers with radii on the order of 10^{16} cm, core Hydrogen column densities on the order of 10^{18} - 10^{19} cm^{-2} , and envelope hydrogen column densities on the order of 10^{16} - 10^{16} cm^{-2} , effectively predict all of these stages. The results of Hester et al. (1996) and Sankrit et al. (1998) suggest that different filamentary densities have caused the R-T instabilities to de-

velop differently throughout the Crab Nebula, which in turn has led to the observed ionizational differences.

In the previous chapter, we applied the Jun (1998) model of PWN to the Crab by including the effects of the pulsar's proper motion toward the NW and the distribution of the ejecta around the explosion center. The results predict that the acceleration of the contact-discontinuity may be the largest factor in the development of R-T instabilities in the Crab Nebula. The pulsar's proper motion has the effect of carrying the synchrotron nebula with it in the NW direction, such that the shock not only propagates farther in that direction over time, but the expansion of the synchrotron nebula into the filaments is also greater in the NW. Those results led us to predict that the R-T fingers would have begun growing in the past in the NW, and should have only recently begun to grow in the SE. Here, we are able to use the observations to test that prediction by determining the stage of the instability and by measuring the lengths of R-T fingers.

6.2. An Asymmetry in the Thickness and Density of the Filaments

Chapter 4 explained that, due to the asymmetry in the pre-shock ejecta density (with respect to the pulsar), we expect that the shock in the NW is traveling faster than the shock in the SE. Here we analyze the ionizational structure of the filaments in order to determine how the ejecta density asymmetry (and the asymmetry in shock speeds) manifests itself in the formation of filaments. First, we would expect a faster shock to result in higher temperatures and therefore longer cooling times for the post-shock gas. A longer cooling time would lead to a thicker cooling region of lower

density, and this is confirmed in the model by Jun (1998) which was discussed in Chapter 5 which predicts that in post-shock gas that can cool radiatively, the filaments are thinner and an order of magnitude more dense than in regions where the gas can not cool radiatively (v_s is high). We can use the *HST* emission line mosaics to compare the thickness and density of the filaments in the NW and SE by measuring then the strengths of low- and intermediate-ionization lines. The emission line intensities will be lower for less dense filaments. Denser filaments provide better shielding from the synchrotron emission and should appear more ionizationally stratified. The thickness of a filament can be determined by the width of the [O III] emission at a given location.

First, we examined the thickness and ionization structure of the filaments in the NW and SE. Figure 25 shows the regions where we measured the line intensities. The profiles were taken in the direction from the contact-discontinuity ($x \approx 0$) towards the shock. In the NW, the filaments are about 60% thicker than they are in the SE, based on the width of the [O III] emission. The thickness of the NW filament is approximately 0.016 pc and in the SE the filaments is approximately 0.0097 pc. The difference in thickness is a direct result of the cooling properties of the gas, with gas in the SE cooling radiatively and the NW having longer cooling times.

The ionization structure also differs between the filaments in the NW and SE. The density is represented by the strength in the line emission, therefore we can only determine relative densities rather than quantitative values. Looking first at the [O III] emission, we note that in the NW the emission rises steeply at the contact-

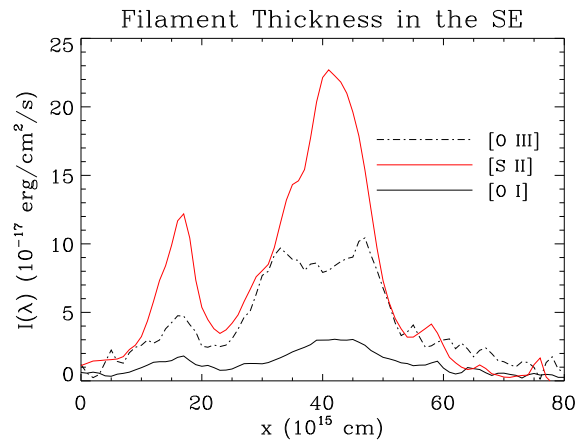
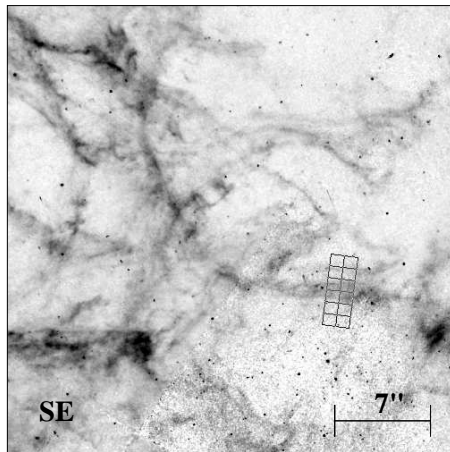
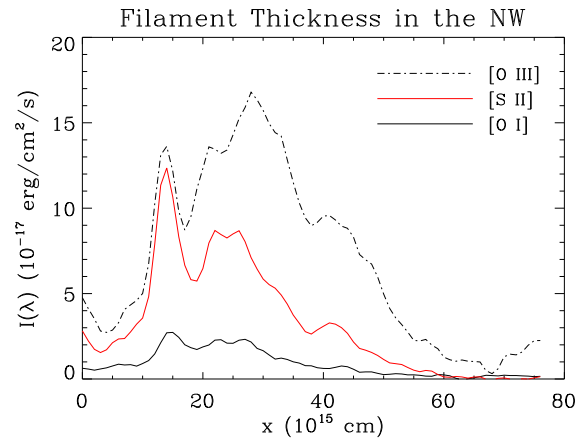
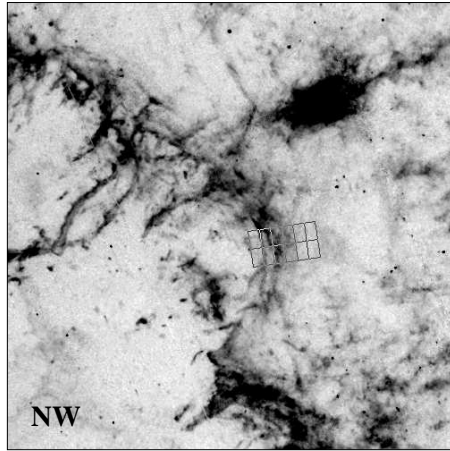


Figure 25. An [O III] image of the NW and SE regions of the Crab including the locations where emission line profiles were measured and shown to the right of the respective image. The line profiles indicate the thickness of the filaments and show their ionization structure for the purpose of comparing these properties between the NW and SE sides of the Crab.

discontinuity. The emission has several peaks and then declines slowly in the direction towards the shock. This slow decline in brightness represents the long cooling time of the gas after a fast shock in which the filaments do not cool quickly. There is almost no [O I] emission in the NW filaments, with only small increases in [O I] emission concentrated in regions coincident with [O III] and [S II] emission peaks. Since higher surface brightness indicates higher densities, this may be expected. The [S II] emission in the NW shows peaks consistent with the [O III] peaks, but unlike [O I], [S II] shows a declining brightness in the cooling region behind the shock, indicating that [S II] emission may come from both dense filaments where the gas is shielded from synchrotron radiation and radiative cooling behind the shock.

The [O III] emission in the SE is only about 60% as strong as the [O III] emission in the NW. But more significantly, on both sides of filaments in the SE, the [O III] emission falls sharply. This is in marked contrast to the NW where the emission decreases more slowly in the cooling region. The sharp filament boundaries in the SE support the claim that the shock is slower here and the gas is cooling on short timescales and forming filaments. The [S II] emission is significantly stronger in the SE than in the NW, peaking at a location where the [O III] emission is rather smooth. Higher line intensities indicate higher densities, consistent with the results by Jun (1998) for radiative cooling.

The density in the filaments is the dominating factor in how the R-T instabilities will develop (Hester et al. 1996), providing there is an acceleration of the contact-discontinuity. Because we are limited in the emission lines we can study using

the *HST* observations, quantifying the density of the filaments around the perimeter is not possible; however, we can infer relative densities by studying the intensity of the lines with respect to ionization levels of an atom. We present a high-resolution image of [O III] - [S II] in both the SE, Figure 26a, and NW, Figure 26b, sides of the Crab. The regions were chosen because they represent the best side view of the filaments in the NW and SE and are nearly the same region used in Figure 25. It is immediately obvious from these figures that the SE contains a significant amount of [S II] emission throughout the filaments. Although the [S II] is not as diffuse as the [O III] in the SE, it is present almost everywhere that [O III] is present. The opposite is true in the NW; the NW does not contain any significant level of intermediate-ionization lines in the outermost filaments. Rather, in comparison to [O III] emission, [S II] is largely constrained to the tips of R-T fingers. This asymmetry is further evidence that the densities of filaments in the SE and NW are quite different. SE filaments have higher densities than the filaments in the NW, which is due to the gas cooling radiatively behind the shock. The Jun (1998) model predicts that when the R-T fingers have completed growing, the tips of the fingers may reach densities that are 10 times greater than the density of the filaments. Although we can not accurately give quantitative values on the densities, we can say from the ionization structure that the tips of the R-T fingers in the NW are denser than the overlying filaments, and this is not the case in the SE.

These results indicate that overall, the filaments in the SE are thinner and more dense than the filaments in the NW, which suggests filaments formed via radiative

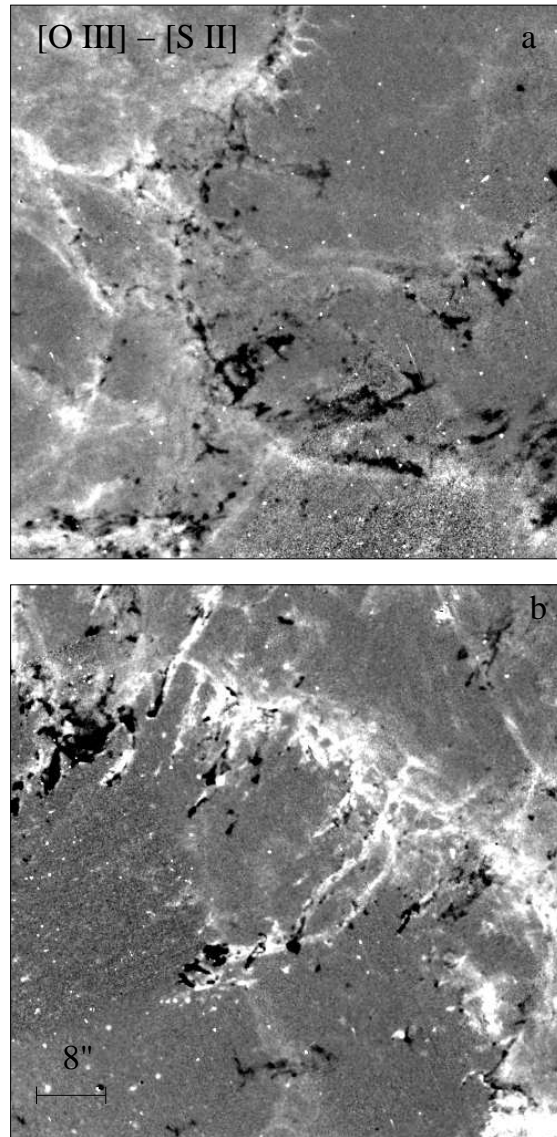


Figure 26. [O III] - [S II] images of the SE (a) and the NW (b) showing the difference in density in these filaments. Intermediate-ionization lines, such as [S II], require shielding from photoionizing photons coming from the synchrotron nebula.

cooling behind the shock front Jun (1998). It follows from the work of Hester et al. (1996), that this asymmetry in density may cause an asymmetry in the development of R-T instabilities, however as shown in Chapter 6, it may be that the asymmetry in the acceleration of the contact-discontinuity may prove to be the more important factor in R-T development.

6.3. An Asymmetry in the Morphology of R-T Fingers

The observations presented here allow us the opportunity to study R-T finger development throughout the entire nebula, and we note that there is a strong NW-SE asymmetry in the morphology of the R-T fingers. In particular, the lengths of the R-T fingers vary dramatically between the NW and SE sides of the nebula. A more subtle difference is that the wavelength of the instability, or the distance of separation between the fingers, is asymmetrical as well. Here, we quantify the differences the lengths and separations of the R-T fingers in the NW and SE regions. In Chapter 5, we applied the results of Jun (1998) model of PWN to the Crab and found that the synchrotron nebula may not be expanding fast enough in the SE direction to cause acceleration of the dense filaments. If this is the case, then we would not expect the development of R-T fingers there. If the interface is just marginally unstable, we would expect there to be a very unorganized morphology in the filaments. In regions where the contact-discontinuity is accelerating, as the model implies for the NW, the instability should have developed long, well-defined R-T fingers. Here we determine if the predictions we make from that model agree with the *HST* observations.

6.3.1. *R-T Finger Lengths and Development*

The primary asymmetry between the NW-SE sides of the Crab is the difference in the length of R-T fingers. We show a high-resolution image of R-T fingers in the SE and a region in the NW in Figure 27, with some fingers numbered that we will discuss further. Clearly, the fingers in the NW appear much longer than the fingers in the SE. Of course, one must take into account projection effects when measuring distances in the nebula. To minimize projection effects, the images shown in Figure 27 were taken symmetrically through the nebula’s major axis. Lengths were measured for fingers within 25° of the defined symmetry axis. The fingers in the SE are “pointing” into the sky while the fingers in the NW have their tips pointed towards Earth-bound observers, but the angle at which the fingers are tilted should be similar between the two ends and would not account for the large difference in lengths that we see. The F-P studies of the Crab by Lawrence et al. (1995) were utilized also indicate that these fingers are as close to edge-on as possible, due to their radial velocities being within a few hundred km s^{-1} (of zero radial velocity) in either the redshifted or blueshifted direction. These fingers have the largest velocity component along the plane of the sky, and therefore the lengths we measure should be most accurate.

The longest fingers in the NW, such as fingers 11, 12 and 13, are more than twice as long as the longest fingers in the SE, fingers 1 and 7. Both the NW and SE regions also have small fingers (2,3 and 14) and areas that appear to be just becoming unstable (4, 8 and 15). Overall, there were 18 easily identifiable and well-developed fingers in the NW compared to 11 in the SE within the constricted area. We measured

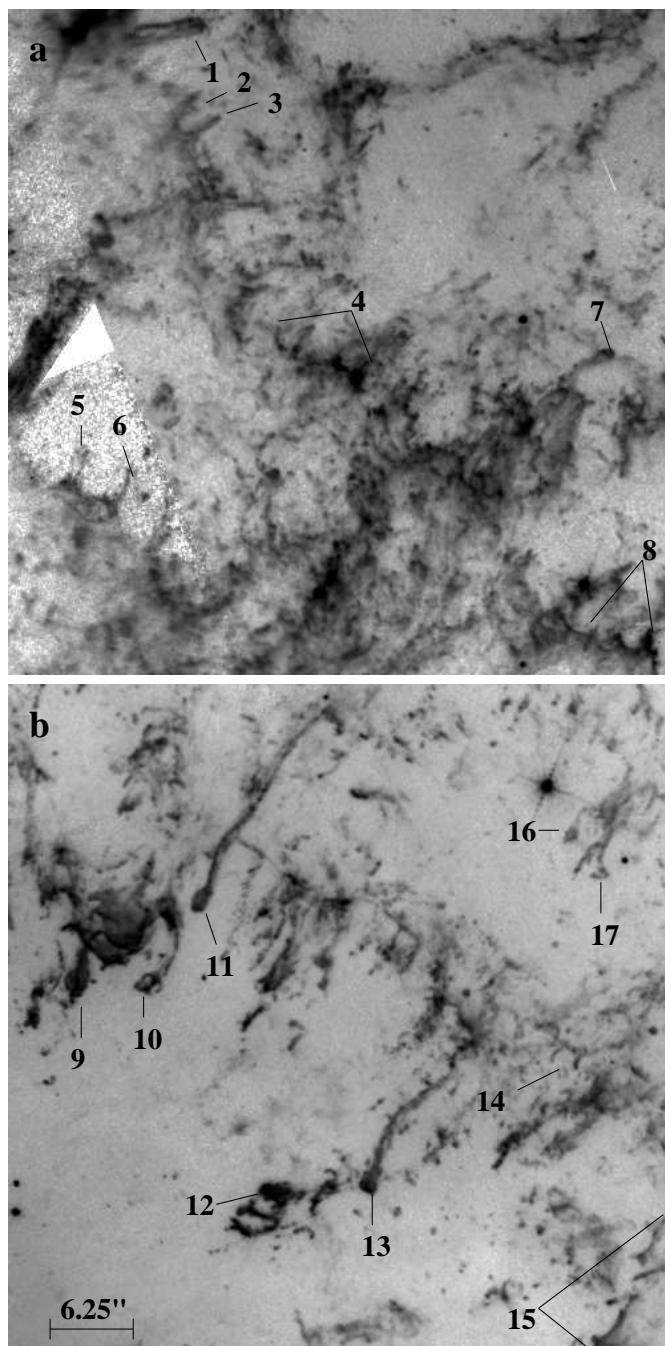


Figure 27. The differences in the lengths of R-T fingers between SE (a) and the NW (b) sides of the Crab Nebula shown in [S II] emission.

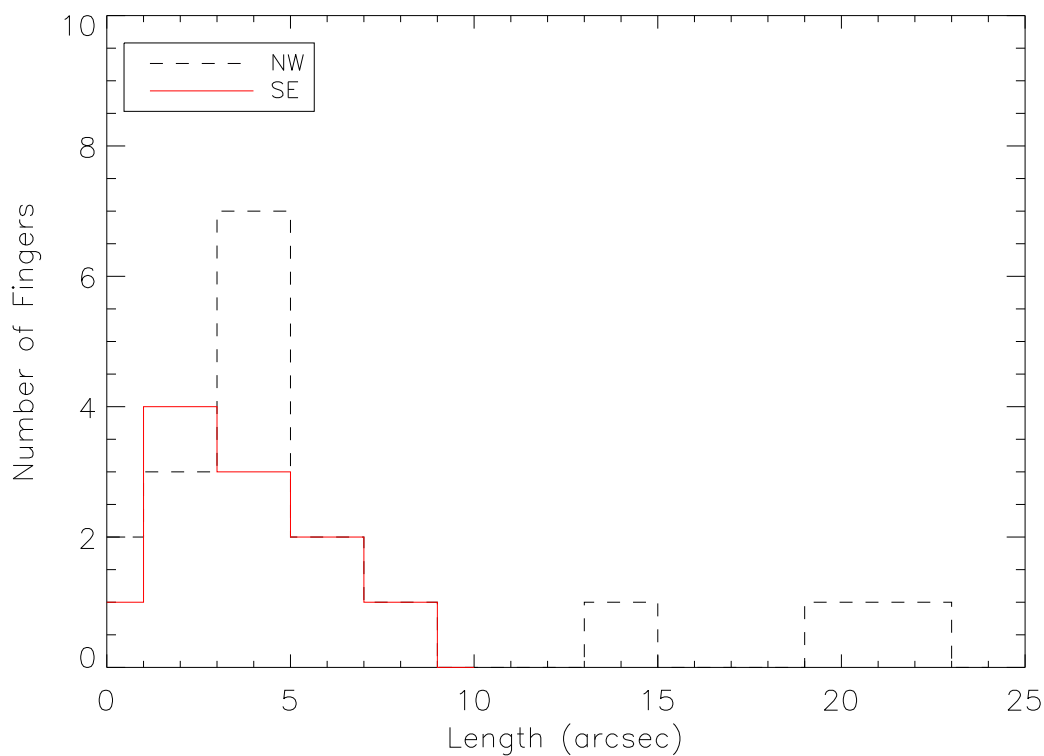


Figure 28. Histogram of the measured lengths of R-T fingers in a 25 degree symmetric area in the SE and NW regions of the nebula.

approximate (2-D) lengths (projected into the sky) for the longer fingers in both the NW and SE by measuring the length between points along the finger and assuming the distance between those points was linear. The results of these length measurements are shown using a histogram in Figure 28. Our measurements indicate that the longest fingers in the SE reach about $8''$, whereas fingers in the NW have projected lengths up to $22''$. The 2-D projection of the nebula means that these are minimum lengths; however, constraining the location of the comparison over a symmetric region would make it unlikely that this $> 60\%$ difference is due to projection effects. We argue that this NW-SE asymmetry in the lengths of R-T fingers is a real effect.

The histogram shown in Figure 28 appears to imply that the NW contains more fingers but this is not the case. The NW simply has more fingers that had measureable lengths ($>$ a few pixels). The R-T instability is apparently in different stages of development in the NW and SE sides. This is inferred due to the filaments in the NW being very organized — the R-T fingers are isolated and easy to define — while the SE contains many areas where the instability has not progressed enough to make long fingers. Rather, the SE is just marginally unstable and contains about a hundred very small fingers and wave-like perturbations (like those seen in regions 4 and 8). The more active instability, meaning that the dominant wavelength has not yet been established, results in the SE a more un-organized morphology and only a few long, well-developed fingers. We predict that in the future the acceleration will increase and a dominant wavelength will be determined. The fastest growing wavelength is determined by the growth rate, defined as

$$n^2 = \frac{2\pi g}{\lambda} \left(1 - \frac{\lambda_c}{\lambda} \right) \quad (6.1)$$

and is equal to twice the critical wavelength (λ_c) (Hester et al. 1996).

A more subtle asymmetry between the morphology of the R-T fingers is the physical separation between them, or the wavelength at which the instability takes hold. We measured the separation of the R-T fingers over a symmetrical 25° area from the major axis of the nebula (the same area used to measure the finger lengths). Figure 29 shows histograms of the wavelength of the instability in the SE compared to the NW. Our measurements indicate that the R-T instability takes effect over a scale of about 1 arcsec in the SE. In the NW, there is a tendency for the instability to

take effect at a slightly larger wavelength ($\approx 1 - 1.5''$) and the maximum wavelength extends to up to $3.5''$, or about $1''$ larger than the greatest separations in the SE. Until the dominant wavelength has taken over the R-T development in the SE, and R-T fingers become prominent throughout the region, we can not accurately determine what the critical wavelength is. The histogram reflects the observation that the SE is very active in that there are more than a hundred wave-like perturbations that could be measured in the SE and only about half of that number measured in the NW. This reflects a difference in the amount of time the instability has been effective in the two areas. In the NW, the interface has been accelerating and the dominant wavelength was determined in the past (Chapter 5). In the SE, the interface has only recently begun to accelerate and therefore the instability has not yet produced the evenly separated, well-defined fingers.

6.3.2. *Ionization Structure at the Tips of R-T Fingers*

R-T Fingers that have been growing for a longer period of time will have more dense ejecta transferred into the finger from the filaments, and this would be observed by those fingers having higher densities (stronger line emission.) Differences in density would affect the ionizational structure of the fingers, because denser fingers would provide better shielding and appear more ionizationally stratified. Like the filaments, denser fingers would show more low- and mid-ionization emission lines. Sankrit et al. (1998) were the first to use a photoionization model describe that the fingers in the NW part of the nebula are ionizationally stratified, meaning that the high ionization emission, [O III], is on the outside of the finger. Inside the shell of [O III] emission,

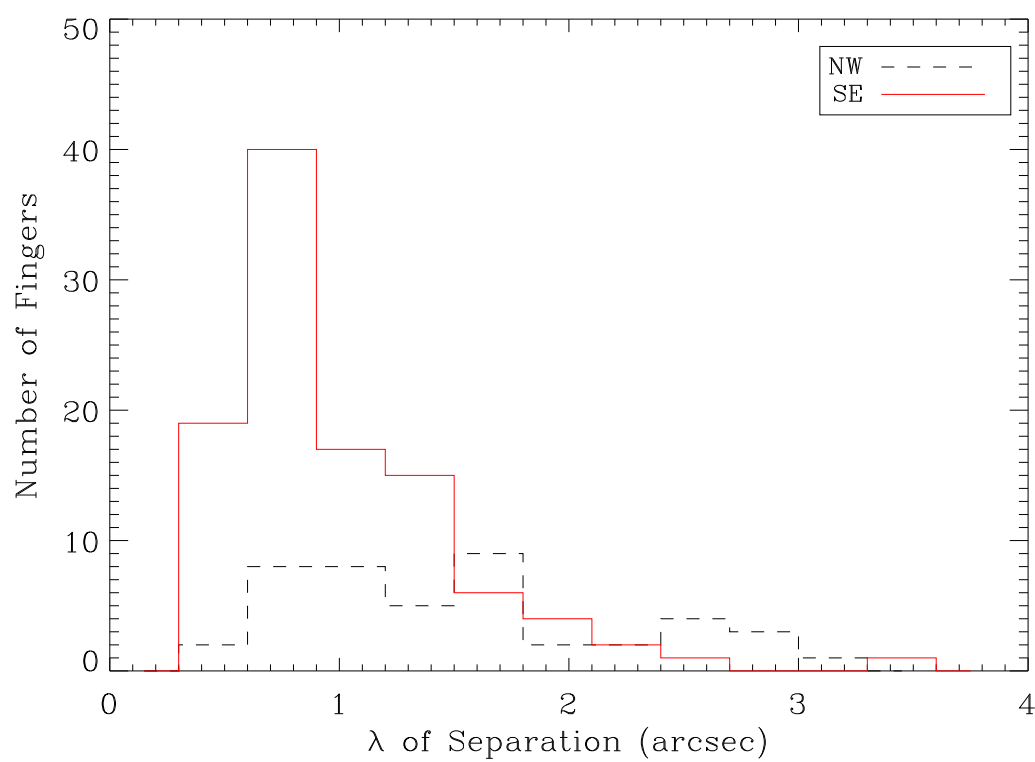


Figure 29. Histograms of the measured separations of R-T fingers in a 25 degree symmetric area in the SE and NW regions of the nebula.

[S II] is found, while [O I] emission exists only in the core of the finger tips where the gas is shielded.

We studied the ionizational structure of fingers in both the NW and SE to determine if there were variations in density and ionization structure with respect to location in the nebula. This was done by measuring the line intensity for [O III], [S II], and [O I] across the tips of R-T fingers. Figure 30 shows two representative fingers in the SE (a,b) and Figure 31 shows NW (c,d) areas of the nebula, respectively. The profiles represent average intensities along the width of the boxed regions in the corresponding image. The x-axis of both Figures 30 and 31 is the length scale in centimeters, with zero starting at the top center of the box in the image. Figure 30a shows the profile of a long finger in the SE, which is labeled Finger 1 in Figure 27. The profile across this region shows [O III] emission surrounding the finger but the [O III] has no clear association with the finger itself, meaning that there are no sharp edges where the finger begins and ends. This lack of an edge to the finger indicates that the gas on the outside of the finger is not very dense and therefore is easily photoionized by the synchrotron nebula. The [S II] emission is highly constrained to the finger, showing a sharp edge on either side and two peaks that correspond with two [O III] peaks. These [S II] emission peaks represent the densest part of the R-T fingertip. This is also indicated by the [O I] profile, where the only emission occurs at these two locations. Also in the SE, Finger 7 from Figure 27, shown in high-resolution in Figure 30b, is a long and well-developed finger. The ionization structure and emission strengths are similar to finger 1. The [O III] level does not rise steeply

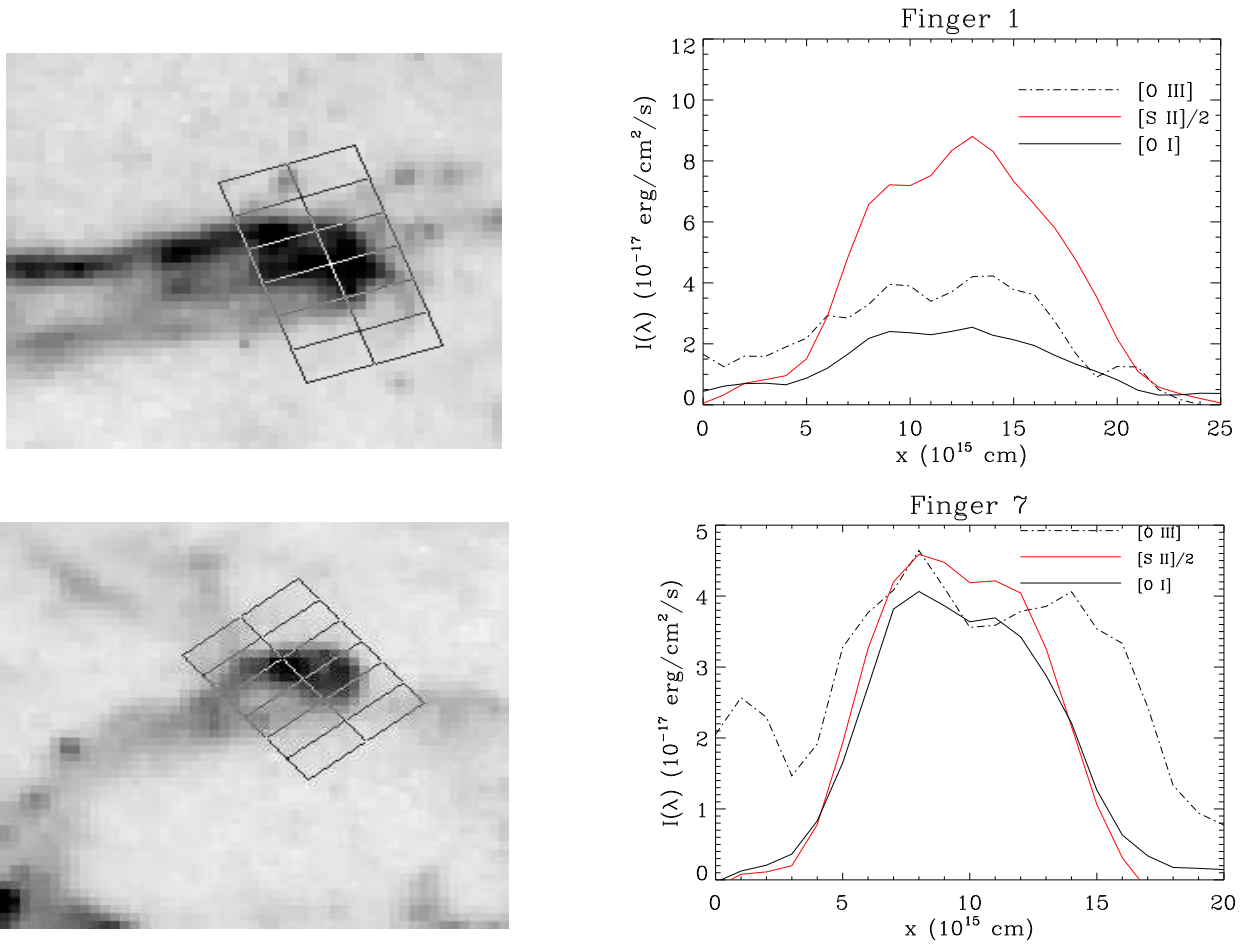


Figure 30. Locations and corresponding line intensities of R-T fingers in the SE.

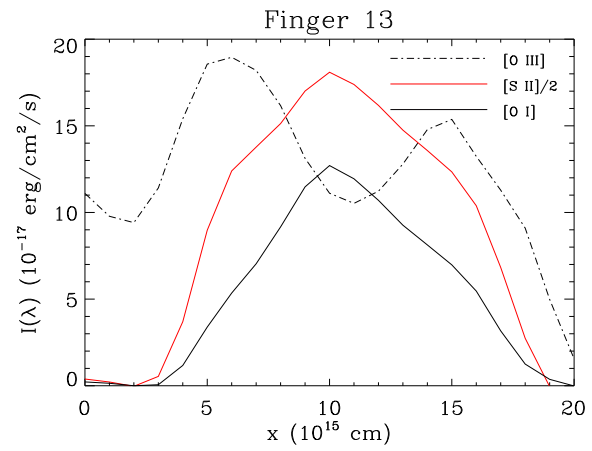
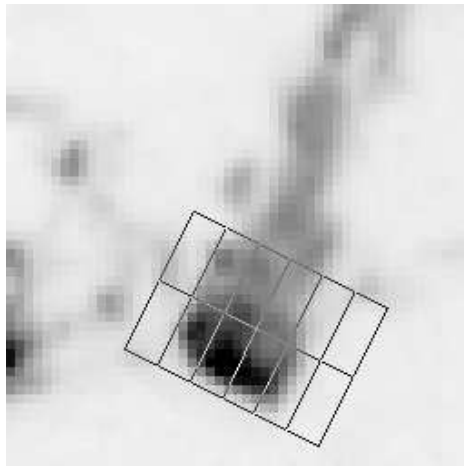
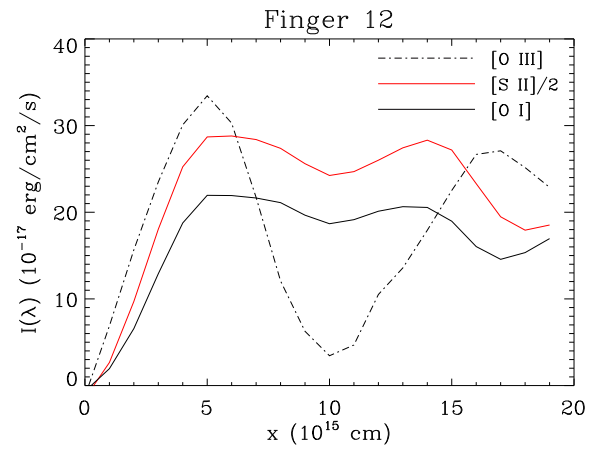
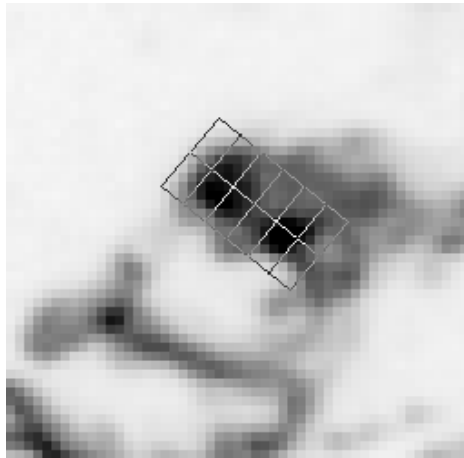


Figure 31. Locations and corresponding line intensities of R-T fingers in the NW.

at the boundary of the finger but rather has a diffuse nature again indicating lower densities. The intensity of the [O III] emission is quite similar between both finger 1 and finger 7. Both the [S II] and [O I] emission arise from compact structures with the highest intensities occurring from the region in the R-T finger that coincides with the densest region of the finger. The [O I] emission is slightly more intense than in finger 7, but the [S II] emission is weaker. The F-P data suggest that finger 1 has a radial velocity between -365 km s^{-1} to -685 km s^{-1} . The *HST* filter bandpass is wide enough to collect the wavelengths of the blue-shifted [O III], [S II] and [O I] emission lines and therefore their respective intensities should be representative of the actual emission. Finger 7 has a radial velocity between -165 km s^{-1} and 155 km s^{-1} , meaning that this finger is nearly aligned edge-on to our line of sight and again all three emission lines would be within the wavelengths observed in the *HST* filter bandpass. Hester et al. (1996) show that fingers of this morphology are still magnetically dominated. The low level of ionizational stratification and the lack of a sharp boundary to the finger is representative of the finger not having been growing for a long period of time.

The tip of R-T fingers in the NW show a very different ionizational structure than what we have shown for fingers in the SE. Figures 31c and d show line intensity profiles that correspond to fingers 12 and 13 in Figure 27. Figure 31c shows a very interesting line profile. The edge of finger 12 is very clear in [O III] emission, which has a steep rise in intensity. We suggest that this finger is highly stratified and therefore the [O III] emission is strongest near the edge of the finger where we are viewing a greater column density of material, and we see two peaks in the line intensity at those

locations. Note that Finger 12 (Figure 31c) has a noticeable depression in the [O III] intensity at the core, or center, of the finger tip, indicating that the core is dominated by low-ionization line emission. The low-ionization emission, however, also shows two peaks in the line intensities, but these peaks are coincident for the [S II] and [O I] lines. The rise in [O III] emission is separated from the [S II] and [O I] emission by approximately 1.5×10^{15} cm indicating a higher level of stratification. The center of Figure 12 has a significant decrease in the intensity of all three emission lines. We interpret this as being a region of such high density that molecules, such as molecular hydrogen, can form. Molecular hydrogen has been found in the Crab using infrared spectroscopy by Graham et al. (1990), although those observations did not include this R-T finger. This finger should be a prime candidate in future H₂ studies of the Crab.

Figure 31d (finger 13 in Figure 27) is similar to Finger 12 in that it shows a well-defined edge in the [O III] emission defined by the two [O III] emission peaks. The [S II] and [O I] line emission peak at the center indicating that finger 13 has a dense, well-shielded core. The peak in the low-ionization emission is coincident with the depression in the [O III] line emission, indicating that this finger has a stratified structure. Note that the [O I] emission is more concentrated than the [S II] emission because it is contained in the densest part of the core. According to Hester et al. (1996), fingers that show this level of ionization stratification are in the non-magnetic regime of the R-T instability and will develop as they would in the linear case. This indicated that the contact discontinuity at this location has been unstable for a longer

period of time than the interface in the SE, and has had more gas transferred from the filaments into the finger.

Comparison of the intensity of the line emission shown in Figures 30 and 31 provide more evidence that the fingers in the NW are older and more dense than the fingers in the SE; the [O III] line intensities of the R-T fingers are 3 - 4 times higher in the NW, the [S II] intensities are between 2 - 4 times higher in the NW, and the [O I] intensities are also 3 - 4 times higher in the NW. The Fabry-Perot data indicate that Fingers 12 and 13 have radial velocities of $195 \pm 295 \text{ km s}^{-1}$ and $258 \pm 232 \text{ km s}^{-1}$, meaning both fingers would have line emission that emits within the *HST* filter bandwidth for all three emission lines. The discrepancy between the line intensities of the NW and SE can not be explained by the narrow-band filters used in these observations. Instead, we argue that the tips of the cores R-T fingers in the NW are a few times denser, and therefore more ionizationally stratified, than the cores of R-T fingers in the SE, with some of NW R-T fingertips possibly being dense enough to harbor molecules such as H_2 . We argue that this represents a difference in the age of these fingers, because the fingers in the NW would have met all of the conditions for the instability to be effective in the past while the SE side has not.

6.4. Proper Motions of R-T Fingers

It is currently unknown if the R-T fingers are continuing to grow or if they are just expanding homologously in time with the rest of the filaments. The *HST* observations show all ranges of the instability, from an unstable surface, to small fingers, to long well-developed fingers beginning to show evidence of K-H instabilities,

and finally isolated knots of emission (Hester et al. 1996; Blair et al. 1997). We were able to use an archived *HST* *WFPC-2* [S II] image taken on November 9, 1995 to determine the proper motion of several R-T fingers in the NW. The 1995 image overlaps Field 2 of our data set, taken on January 1, 2000 and the overlapping stars were aligned to the 2000 mosaic using techniques similar to those used to make the mosaics. We have approximated stellar offsets of about $0.06''$ between the two mosaics, or just over a half-pixel. We measured the location of R-T fingers tips and the location where that R-T finger attaches to the overlying filament in both epochs. We then routinely found the minimum chi squared of coincidence of the subtracted [S II] images by varying the spatial alignment of the two epochs and overlaying the images in order to calculate the distance traveled in the plane of the sky. The output of the routine was compared with manual results estimated by eye and both methods gave similar results. Next, we calculated the transverse velocity of those locations over the time of these two observations. We also measured the velocity that the R-T finger tip and filament would have been expected to travel assuming homologous expansion and the Kaplan et al. (2008) expansion center. We used the same technique to calculate the transverse velocity of two, isolated knots of emission to determine if they experienced a different expansion rate than fingers and filaments that were attached to each other. The knots chosen were in a close spatial relationship to Finger 12 as a means to compare results. The specific R-T fingers measured were fingers 10, 11, 12 and 13 from Figure 27. Figures 32 and 33 contain an [S II] image of the respective R-T fingers and knots with red asterisks representing the x, y locations of the R-T fingers,

filament or knot being measured. Beside that image there is a subtracted image of the two epochs with vectors representing the transverse velocity we measured (red) and the transverse velocity expected assuming homologous expansion (green). The x,y pixel offsets of reference stars within both images were used to determine the standard deviation in proper motions. We estimate the error to be about $0.01'' \text{ yr}^{-1}$ or 207 km s^{-1} , although this is a minimum error due to the non-uniformity of the shape of fingers between the two epochs.

Figure 32 a and b show that the R-T finger tip and the filament are expanding at a velocity that is about 300 km s^{-1} higher than what is expected assuming homologous expansion. That being the case, the finger appears to be expanding with the filament and does not show signs of significant growth in the 5 year timeframe of these images. In comparison, the knots of emission that are not physically attached to any other filaments shown in Figure 32 c and d, are expanding at about 200 km s^{-1} faster than what would be expected assuming homologous expansion, but considering the possible errors in these measurements an assumption of homologous expansion is not unreasonable.

Figure 33 a and b show similar images as discussed above but for R-T finger 11. In this case, the tip of the finger has a transverse velocity that is about 300 km s^{-1} greater than the expected value but the filament is greater by only about 100 km s^{-1} . In this case, the filament may be “pulling” the finger along faster due to the physical attachment. However, this observed difference could be due to line-of-sight effects if the finger is angled toward our line of sight near the filament but is closer to edge-on

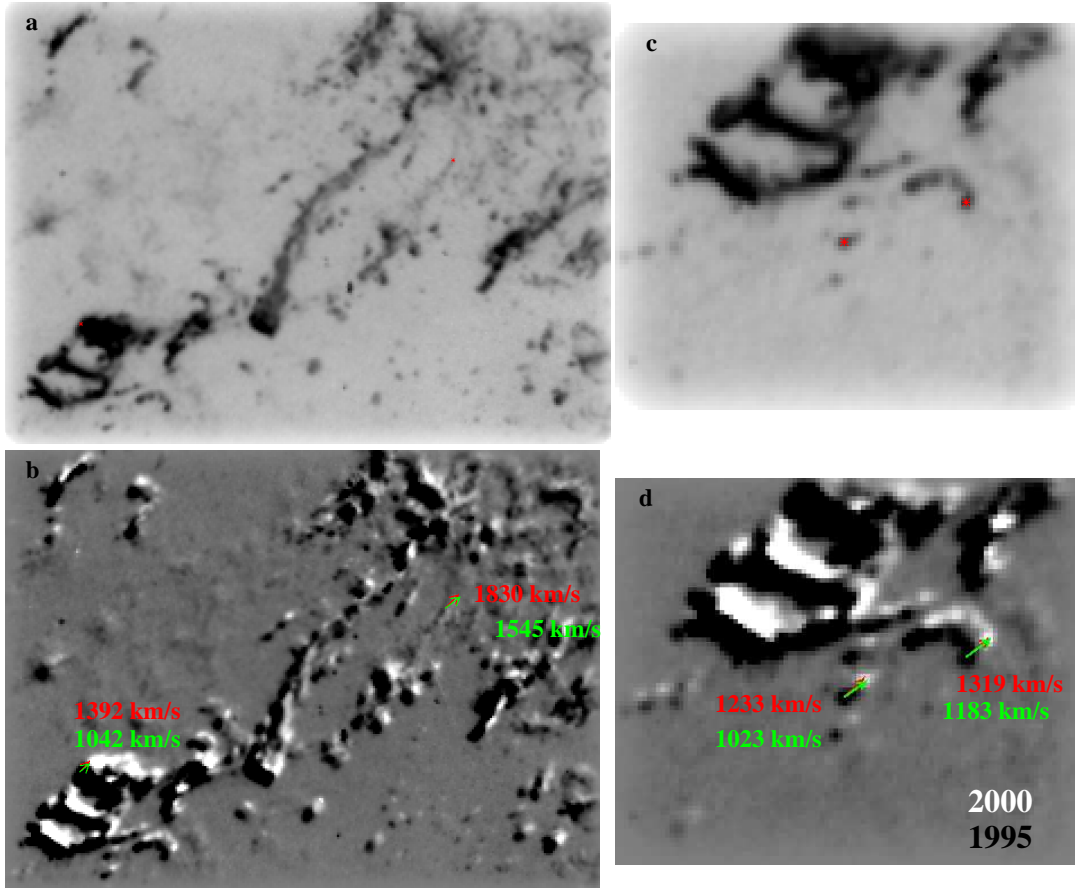


Figure 32. Locations in the NW where we used a 1995 archived *HST* *WFPC*-2 image and our *HST* *WFPC*-2 image taken in 2000 to calculate the transverse velocity of R-T finger 12, the filament it attaches to, and two isolated knots of emission. a. An [S II] image showing the x,y locations used to measure the velocity of finger 12 and associated filament b. A subtracted image of the two epochs with vectors representing the measured (red) and expected (green) transverse velocity c. [S II] image of two knots with positions marked d. The measured (red) and expected (green) transverse velocity vectors for the knots. The errors in the velocities may reach 207 km s^{-1} due to stellar offsets.

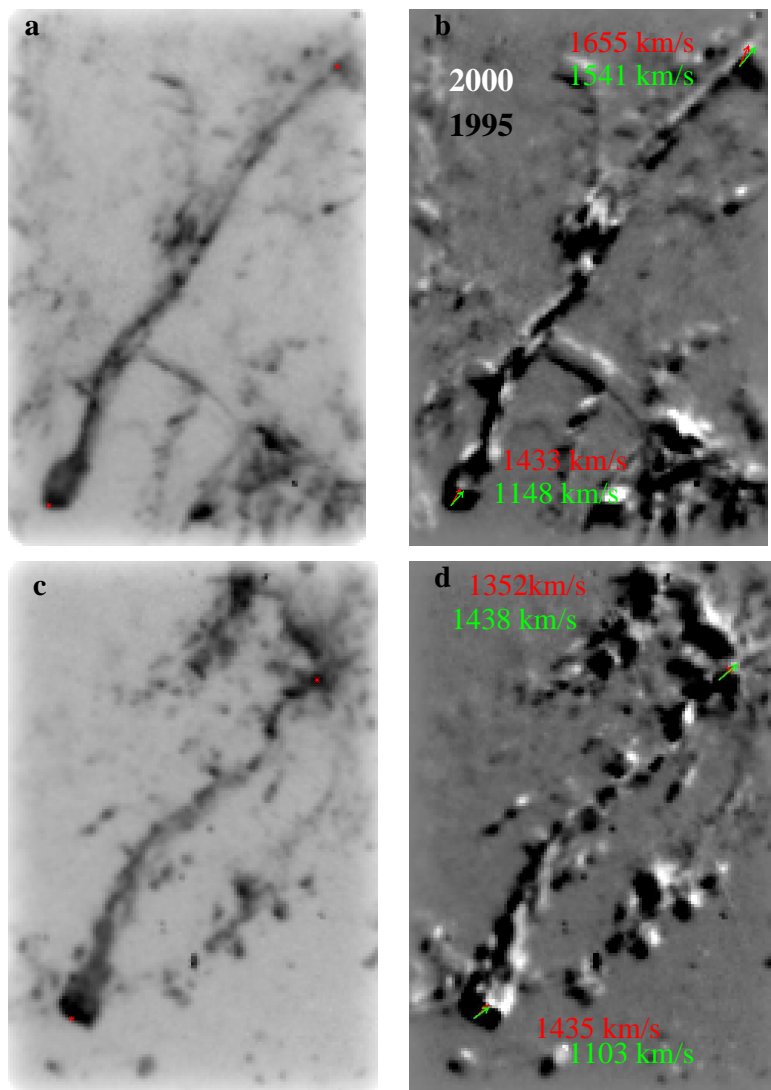


Figure 33. Locations in the NW where we used a 1995 archived *HST* *WFPC*-2 image and our *HST* *WFPC*-2 image taken in 2000 to calculate the transverse velocity of R-T fingers 11 and 13 and the filament they attach to. a.) An [S II] image showing the x,y locations used to measure the velocity of finger 11 and associated filament b.) A subtracted image of the two epochs with vectors representing the measured (red) and expected (green) transverse velocity c.) [S II] image of finger 13 with x,y positions marked d.) The measured (red) and expected (green) transverse velocity vectors for the knots. The errors in the velocities may reach 207 km s^{-1} due to stellar offsets.

near the tip due to curvature in the finger. Finger 13, shown in Figure 33 c and d shows a similar effect as finger 11. The tip is expanding 300 km s^{-1} faster than what would be expected for homologous expansion but the filaments in this case are very close to the homologous expansion assumption, especially when taking into account errors. The reasons for this difference could again be due to the connection of the finger to the filament or a line-of-sight effect.

6.4.1. *Development of R-T fingers in Time*

There are two possible explanations for the NW-SE asymmetry in the length of R-T fingers in the Crab Nebula. One explanation is that the R-T fingers developed at roughly the same time but the R-T fingers in the NW grew faster and are now longer than the fingers in the SE. The second possibility is that the fingers in the NW formed before the fingers in the SE but grow at a similar rate, so that the difference in age is what has caused the prominent asymmetry in the lengths between the two sides.

We suggest that the asymmetry in the lengths of R-T fingers present in the Crab Nebula can be explained by the transverse velocity of the pulsar and the effect this has on the expansion of the synchrotron nebula. In Chapter 4, we presented evidence in support of a varying shock speed around the perimeter of the nebula that is dependant on the distance of the shock from the expansion center and the ejecta density at a given location. The pulsar's transverse velocity toward the NW and the elliptical shape of the synchrotron nebula has caused the shock to propagate through the freely expanding ejecta faster and farther in that direction than any other. In

other words, this means that the shock has passed through a higher volume of ejecta in the NW than in the SE because it is farther from the expansion center and that ejecta is now contained in filaments and R-T fingers. That being the case, then one would expect that the filaments in the NW contain more mass than the filaments in the SE.

There must be a minimum mass density of a filament that is necessary for the mass to overcome the magnetic tension and cause the filament to become R-T unstable (Hester et al. 1996). We assume that the magnetic field strength is nearly equal at both the NW and SE edges. The reason we can assume this is because radio images of the Crab Nebula do not show significant differences in the intensity of emission around the perimeter. So, if the magnetic field is similar at the edge of the synchrotron nebula, then the mass density of the filaments would be the dominating factor in the development of R-T instabilities according to the formula $\rho_{\text{crit}} = B^2/g\lambda$ (Hester et al. 1996). The faster progression of the shock through the ejecta in the NW direction should lead to the filaments in the NW reaching this critical density earlier than anywhere else in the nebula. If the first fingers to form in the NW, then those fingers would be expected to have more material transferred into them today than fingers that developed later. We have presented results that show that the NW region of the nebula does contain the longest R-T fingers. The geometry of the nebula shown in Figure 16) is such that the edges of the nebula along the major axis (the NW and SE) have the largest distances from both the pulsar and the approximate explosion center. The next region that R-T fingers would be expected to

have developed, then, would be the SE, while regions in the north and south parts of the nebula would develop R-T fingers last. There are several reasons to believe this. First, the acceleration of the contact-discontinuity is a critical component of the R-T instability. Regions that have not expanded as far from the center of the remnant have obviously not accelerated as quickly as those regions that have covered larger distances in the same amount of time. Another factor is the amount of ejecta that has been swept up by the shock. In areas where the shock has passed through more ejecta (the NW and SE), there is more dense gas at the contact-discontinuity and the critical density, ρ_{crit} needed to overcome the magnetic tension would be reached before regions that have swept up less gas. The *HST* images presented here show that SE does contain most of the other R-T fingers in the nebula but even the few long fingers in the SE are only about half as long as the fingers in the NW. Very few R-T fingers are found outside of the NW-SE regions and virtually no long fingers ($> 4''$) exist anywhere except the NW or the SE. These observations alone, though, do not provide the information necessary to determine if the fingers formed at the same time or if the NW fingers formed first.

The results of Chapter 5, where we applied the PWN model by Jun (1998) to the Crab Nebula, have shown that the interface in the SE has only recently begun to accelerate. Therefore, even if the filaments have reached the critical density necessary for the instability to take hold, the interface would remain stable. Acceleration is a necessary component for the R-T instability. Our observations support what we predicted in the previous chapter: The SE side has only recently begun to accelerate

and therefore has a very unorganized morphology and few fingers. The R-T instability is more active in the SE, meaning that the contact-discontinuity is perturbed throughout, indicating that the fingers are in a more active state of growth. The appearance of the instability in the SE is consistent with what we would expect if there has not been time for the strongest modes to dominate the instability. In the NW, the interface has been accelerating in the past such that the wavelength of the instability is well-determined and has produced long, well-developed fingers. Over time, gas from the filaments has been transferred into the fingers and they appear more dense and ionizationally stratified than the fingers in the SE.

6.5. Results

We found that there is an asymmetry in several filamentary properties. First, the filaments in the SE are thinner and denser than the filaments in the NW, shown by the amount of [S II] relative to [O III]. In the NW, the [S II] emission is much more confined to the tips of R-T fingers, but in the SE the [S II] emission is prevalent all throughout the filaments. This is due to the properties of the shock. Faster shocks result in thicker, but less dense filaments because the gas is not able to radiatively cool as quickly. This effect is predicted by Jun (1998) and is found to agree with our interpretation of difference shock speeds around the perimeter as a result of the asymmetry in the pre-shock ejecta density with respect to the pulsar (Chapters 3-4).

We have also determined that there is an asymmetry in the lengths and distributions of R-T fingers. In the NW, R-T fingers are up to twice as long as the longest fingers in the SE. In fact, the SE contains only two long ($> 4''$) fingers. The overall

morphology of the SE filaments is quite different than what is seen in the NW. In the SE, the filaments appear very unorganized and more active indicating that the instability took affect later here. We predicted in Chapter 5 that the interface has only recently begun to accelerate in the SE, and this observation agrees with that prediction. We also predicted that the contact-discontinuity has been accelerating in the NW, which explains why the observations show long, well-developed and well-defined fingers in the NW. We attribute the asymmetry in the development of the R-T instability to the expansion of the PWN. Since the PWN is always centered around the pulsar, the expansion is faster in the NW direction and acceleration of the contact-discontinuity has been taking place. The fingers developed in the NW long ago, and have been in an active state of growth, explaining why these fingers are twice as long as the fingers in the SE, which have only recently begun to grow.

The difference in age of the R-T fingers has led to more gas being transferred from the filaments to the finger in the NW than in the SE, meaning the NW tips of the fingers are more dense and more ionizationally stratified. In the NW, the tips have well-defined edges, with a sequence of ionization layers moving into the core: [O III] on the outside, [S II] farther in, and [O I] at the center. Hester et al. (1996) explain this morphology as filaments that are no longer magnetically dominated. The SE tips do not have well defined edges in [O III] emission. The [S II] and [O I] emission occur in the tips as well, but the line intensities are much lower meaning that the densities are lower and the temperatures are higher. These fingers are still magnetically dominated (Hester et al. 1996). All of the emission lines are about 3

times weaker in intensity in the SE R-T finger tips.

These observations agree with our predictions from the PWN model that implied an acceleration of the NW contact-discontinuity and only a marginally accelerating interface in the SE. From our predictions and these observations, we infer that the R-T fingers began growing at different times in the nebula’s history. The different formation times would be a direct result of the transverse velocity of the pulsar affecting the expansion of the nebula along its long axis, and the overall gradient in ejecta density with respect to distance from the expansion center. These effects combine to form the following picture: when the synchrotron nebula initially began expanding, it would have encountered a declining density gradient toward the NW but an increasing density gradient in the SE direction because the ejecta was distributed around the point of the explosion while the pulsar was “kicked” away and has been moving along with the ejecta expelled at that same velocity. If the synchrotron nebula formed simultaneously with the pulsar, this effect may not have dramatically altered the evolution of the nebula. Still, the transverse velocity of the pulsar towards the NW has, over time, had the effect of accelerating the expansion of the nebula in that direction and accelerating the filaments on the NW side, more. Using a 3-D ellipsoid, we calculated that the NW is about 1.4 times farther from the expansion center than the SE side. We assume, then, that the NW has swept up more ejecta here than in the SE, and furthermore the critical mass density of the filaments necessary to cause the R-T instability to begin should have been reached earlier in the NW. The R-T fingers in the NW would be expected to have earlier formation times, thus explaining

why the fingers in the NW are currently the longest and most developed fingers in the nebula. Further, the conditions for the R-T instability would have been even better met in the past. We predicted that in the past, the acceleration in the NW would have been slightly higher, the shock speeds less (due to propagation into less dense ejecta), meaning shorter cooling times and denser filaments. The fingers have likely passed their fastest stage of growth, and perhaps have ceased growing altogether since the shock is increasing in speed and the critical density may no longer be reached in the NW filaments. On the contrary, the synchrotron nebula expansion (and acceleration) into the surrounding ejecta would occur at a slower rate in the SE since the pulsar moves in the opposite direction, causing the R-T development to begin later in the nebula's history. The appearance of unorganized filaments is evidence that the instability is just taking effect. However, our predictions from Chapter 5 suggest that acceleration will increase in time, therefore the growth of R-T fingers should continue in this region. Perhaps in hundreds of years, the SE filaments will look more like what the NW filaments look like today.

Different ages of the R-T fingers explains the ionizational asymmetry between fingers in the NW and fingers in the SE. The tips of NW fingers show more intense emission indicating that the NW fingers contain more gas than the tips of fingers in the SE. Also, the R-T fingers in the NW are ionizationally stratified, with [O III] shells and low ionization cores. The [O III] is more diffuse in the SE and therefore the fingers show no sharp edge. We attribute this asymmetry to the NW finger tips having higher densities and therefore permit a higher level of shielding from the EUV

synchrotron radiation giving more ionizationally stratified finger tips. Combined with the stronger overall emission, these observations can be attributed to the NW fingers having filamentary gas deposited into them over a longer period of time making them both more massive and more dense as the gas compressed. In the SE, we believe the filaments have been unstable for a shorter period of time and therefore less gas has been siphoned into the fingers. The younger age leads to less dense fingers and consequently a less stratified nature because there is less shielding.

Unfortunately, from these observations alone we are unable to determine the exact ages or growth rates of the R-T fingers. Proper motion measurements of the R-T fingers in the NW seem to suggest that the R-T fingers expand faster than what would be expected from homologous expansion, perhaps due to their attachment to the outer filaments.

CHAPTER 7

Dust Extinction in the Crab

7.1. Introduction

Core-collapse supernovae, like the explosion that caused the Crab Nebula, are thought to be important mechanisms for producing dust in the universe. Observations of galaxies at high-redshift ($z \gtrsim 6$) show that they contain $\gtrsim 10^8 M_{\odot}$ of dust (Bertoldi et al. 2003, Pei et al. 1991, Pettini et al. 1997). These galaxies are only about 1 Gyr, and would not have had time for a significant amount of stars to evolve to the red giant stage. Rather, supernovae are believed to be responsible for producing dust in the quantities that are deduced from observations. Models by Dwek et al. (2007) indicate that each SN must produce between $0.1 - 1 M_{\odot}$ of dust to account for the high amounts of dust in the early universe. Current estimates of dust produced in supernovae fall far below this value, however, with infrared observations of various supernovae suggesting the dust masses are more like $10^{-4} - 10^{-3} M_{\odot}$ (Kotak et al. 2009). The production of dust in core-collapse supernovae remains an open question.

As stated in Chapter 1, Cernuschi, Marsicano, & Codina (1967) were the first to propose that dust could condense from the supernova ejecta at a time shortly after the explosion when gas densities are very high. The dust grains are thought to form from metals in the helium-core layer of the expanding ejecta where densities are high and temperatures are cool (Nozawa et al. 2010). There are several examples of Type II supernovae that show evidence of dust formation in the ejecta (Lucy et al. 1989; Elmhamdi et al. 2003; Sugerman et al. 2006). In each of these cases, the dust is estimated to have formed later than 400 days after the explosion. Other SNR show dust forming at earlier times, and Nozawa et al. (2008) found that the

timing of the formation of dust grains may be dependent on the mass of the hydrogen envelope; dust will form at earlier times when the progenitor has a relatively low-mass hydrogen envelope. The mass of the hydrogen envelope can also affect the dust grain properties. A low-mass hydrogen envelope allows the ejecta to have a higher expansion velocity and a lower gas density, which has the effect of preventing large grains from developing.

A low-mass hydrogen envelope may also hasten the time at which the reverse shock encounters the ejecta, and dust grains that are embedded in such shock-heated gas could be destroyed both by sputtering and by colliding with the shock-heated ions (Nozawa et al. 2010). A model by Silvia et al. (2010) shows that grains that are larger than $0.1 \mu\text{m}$ lose about 30% of their mass, whereas grains smaller than this may be completely destroyed in the reverse shock. They also demonstrated that the compositional make-up of the grains also matters: 80% of Fe grains can survive the reverse shock but only 20% of SiO_2 grains remain. We do not know the conditions of hydrogen-envelope of the progenitor star of the Crab Nebula. We do know, though, that the supernova was a cavity explosion and therefore no reverse shock has formed that would have destroyed dust in the expanding ejecta. The dust that formed in the Crab supernova explosion does have to survive the the shock produced by the expanding synchrotron nebula if we are able to see the dust in the filaments, but we note that shock speeds that we expect in the Crab at the boundary of the synchrotron nebula ($100\text{-}200 \text{ km s}^{-1}$) are far less than what would be expected for a reverse shock (10^3 km s^{-1}), making the conditions more apt for the survival of dust grains.

Several IR studies have been done to estimate the mass of dust in the Crab. The peak of the IR emission in the Crab Nebula, due to dust, is at about $50 \mu\text{m}$, which would arise from gas at about 60 K (Marsden et al. 1984). Recent *Spitzer* data of the Crab taken with the *Multi – Band Imaging Photometer for Spitzer (MIPS)* at 24 (measuring dust at about 200 K) and $70 \mu\text{m}$ (measuring dust at about 40 K) over the equatorial region showed an infrared excess; however, the authors were uncertain if the excess was due to warm dust or line emission from the filaments (Temim et al. 2006). They estimated from the infrared excess that the amount of dust in the Crab is between 10^{-3} to $10^{-2} M_{\odot}$. It is therefore likely that the excess emission measured by *Spitzer* is due to warm dust in the nebula, but the peak dust emission could be well outside of the *Spitzer* bandpass. We argue that, to date, the infrared studies have not been able to account for the amount of dust in the Crab and that estimates for the mass of dust associated with those studies [$0.001\text{-}0.03 M_{\odot}$ (Temim et al. 2006, Marsden et al. 1984) are lower limits. Cold dust would not be observed, and there is the added caveat that the subtraction of the synchrotron nebula introduces significant uncertainties in the masses derived. Ouellette et al. (2010) reviewed observations of the Crab and concluded the condensation efficiency, η_{cond} (the fraction of the supernova ejecta that condenses into dust), was in the range of $10^{-3} < \eta_{\text{cond}} < 0.1$. Condensation efficiencies of the upper end of this estimate are consistent with what would be necessary to make supernovae major contributors to dust in the early universe.

The Crab Nebula offers a unique opportunity to study dust production in Type

II supernovae for several reasons. First, the Crab Nebula is a young and relatively nearby supernova remnant, allowing high-resolution imaging with respect to other SN. Also, the supernova explosion occurred in a cavity, so there is a reasonable chance that dust present in the ejecta was produced in the explosion and would survive. Perhaps most significantly, the presence of the PWN serendipitously allows us the opportunity to observe the stellar ejecta directly, as it is cooling behind the shock. At the optical wavelengths of the synchrotron emission, at the resolution afforded by *HST*, we are able to resolve individual clumps of dust through extinction of synchrotron light, and correlate those dust clumps with the densest regions of the filaments. The dust present in the filaments at this time was either swept up from the ISM, created in the expanding SN ejecta soon after the explosion, or created in the cooled, post-shock gas that makes up the filaments. Observations in the extinction of synchrotron light allow us to distinguish between these possibilities.

Observations that yield a dust-to-gas mass ratio in dust associated with the filaments are especially diagnostic. Sankrit et al. (1998) used photoionizational modeling of an R-T finger in the NW region of the Crab to determine the gas-to-dust ratio at a specific location (region G in Figure 6 of H96, dust knot 4E in FB90). They measured the drop in continuum intensity at the location of the dust absorption feature, and they assumed that the dust was located halfway into nebula along our line-of-sight, based on the morphology of the finger. They measured the extinction to be 1.2 mag at the center of the filament. They then assumed a uniform grain size of $0.075 \mu\text{m}$ (following FB90), which is consistent with the extinction occurring at visible

wavelengths and for dust with ISM opacity. At the wavelengths near the continuum filter, ($\approx 5500\text{\AA}$), the ratio of the actual extinction cross section to the geometric cross section, called the extinction efficiency, Q_e , is approximately 2 (Spitzer 1978) and they used this value to calculate the dust column. Again following FB90 and taking the density of dust to be 2 g cm^{-3} , Sankrit et al. (1998) found that the dust mass column for dust clump 4E (FB90) is about $1.1 \times 10^{-5}\text{ g cm}^{-2}$. Sankrit et al. (1998) used Model F from their photoionizational models of an R-T finger and a helium abundance of 2 times the solar value to estimate that the column density of the gas in the filament is $8.8 \times 10^{-5}\text{ g cm}^{-2}$. The resulting dust-to-gas ratio is 0.13, or an order of magnitude above the typical ISM value of 0.01 (Pei 1992). This is to be contrasted with infrared dust studies of the Crab overall, which find a dust-to-gas ratio that is more similar to the ISM value (Strom & Greidanus 1992; Green et al. 2004). Here, we build on the ideas of how Sankrit et al. (1998) determined the gas-to-dust ratio in the filaments but more accurately determine the three-dimensional location of the dust in the nebula and the extinction levels at those locations.

In this chapter, we address several outstanding issues regarding dust in the Crab supernova remnant and its possible origins. First, we use the correlation of dust absorption features in the continuum mosaic and the low-ionization emission to study the distribution of the dust in the ejecta. For example, if the dust formed in the ejecta soon after the SN explosion or if the dust was part of surrounding ISM, the dust would and be well-mixed in the ejecta and there would be a high correlation between dust and [O I] emission in filaments of all morphological types. Another

possibility is that the dust is currently forming in the densest parts of the nebula, the tips of R-T fingers, and in that case we may expect to find dust that is more localized to regions where the R-T instability has produced long R-T fingers with dense tips. Second, we wanted to determine more accurate dust-to-gas ratios in the filaments. This was completed by following a procedure much like what was done by Sankrit et al. (1998), and incorporating velocity information from F-P data (Lawrence et al. 1995) to provide a better estimate for the physical location of the dust within the synchrotron nebula. More accurate dust-to-gas ratios would help constrain the origins of the dust. Values near 0.01 would likely indicate an ISM origin, whereas values $\gg 0.01$ would imply formation in the supernova ejecta or in the R-T fingers. The combination of the dust-to-gas ratio and the association with [O I] allows us to distinguish between the three possible sources of dust in the Crab.

7.2. Dust Absorption in the Crab Nebula

The *HST* continuum image shows the visible ($\lambda 5370 \text{ \AA}$) synchrotron emission. Apparent in this image, due to the high resolution, are areas of extinction that are due to dust grains absorbing some of the synchrotron emission. These “absorption features” were first noted in ground-based images of the synchrotron nebula [Fesen & Blair (1990), hereafter FB90, Hester et al. 1990], and appear as dark clumps surrounded by bright emission. The *HST* continuum mosaic presented here is the first data set to show the global distribution of dust in the nebula at a resolution that resolves the individual dust clumps. Figure 34 shows the portion of the synchrotron nebula where the intensity of the visible synchrotron emission is high enough that

the dust absorption features can be seen. We note from Figure 34 that there is a notable “chain” of dust crossing the front face of the nebula, particularly on the east side of the pulsar, that continues through the west side. A portion of this chain was noted by FB90 (around Region 2). The dust in this extended region crossing east to west corresponds to a bright filament that crosses the front face of the Crab (FB90) and the dust is believed to correspond to the densest regions of the filaments. Other areas of dust absorption are seen throughout the nebula but tend to appear as isolated features with typical scales of about $2''$.

The dust absorption features we observe in the *HST* continuum image must either reside on the near-side of the remnant or in filaments that are very nearly edge on. We can not observe dust within ejecta on the far-side of the remnant because there would be no synchrotron emission behind it to be absorbed. We also can not see dust in filaments where the synchrotron emission is weak (near the edge of the nebula) because the emission is too faint for any drop in intensity to be noted. For these reasons, we estimate that dust absorption features seen in the *HST* continuum image represent roughly half of the dust in the Crab.

7.3. Correlating Dust Absorption Features with Low-Ionization Emission

The *HST* mosaics give us the opportunity to study the correlation of individually resolved dust clumps with the low-, intermediate-, and high-ionization gas. To complete such an analysis it was essential to determine which filaments are on the front face of the nebula versus which are on the back; we are not able to see dust that is on the back-side and would mistakenly infer no association with dust for

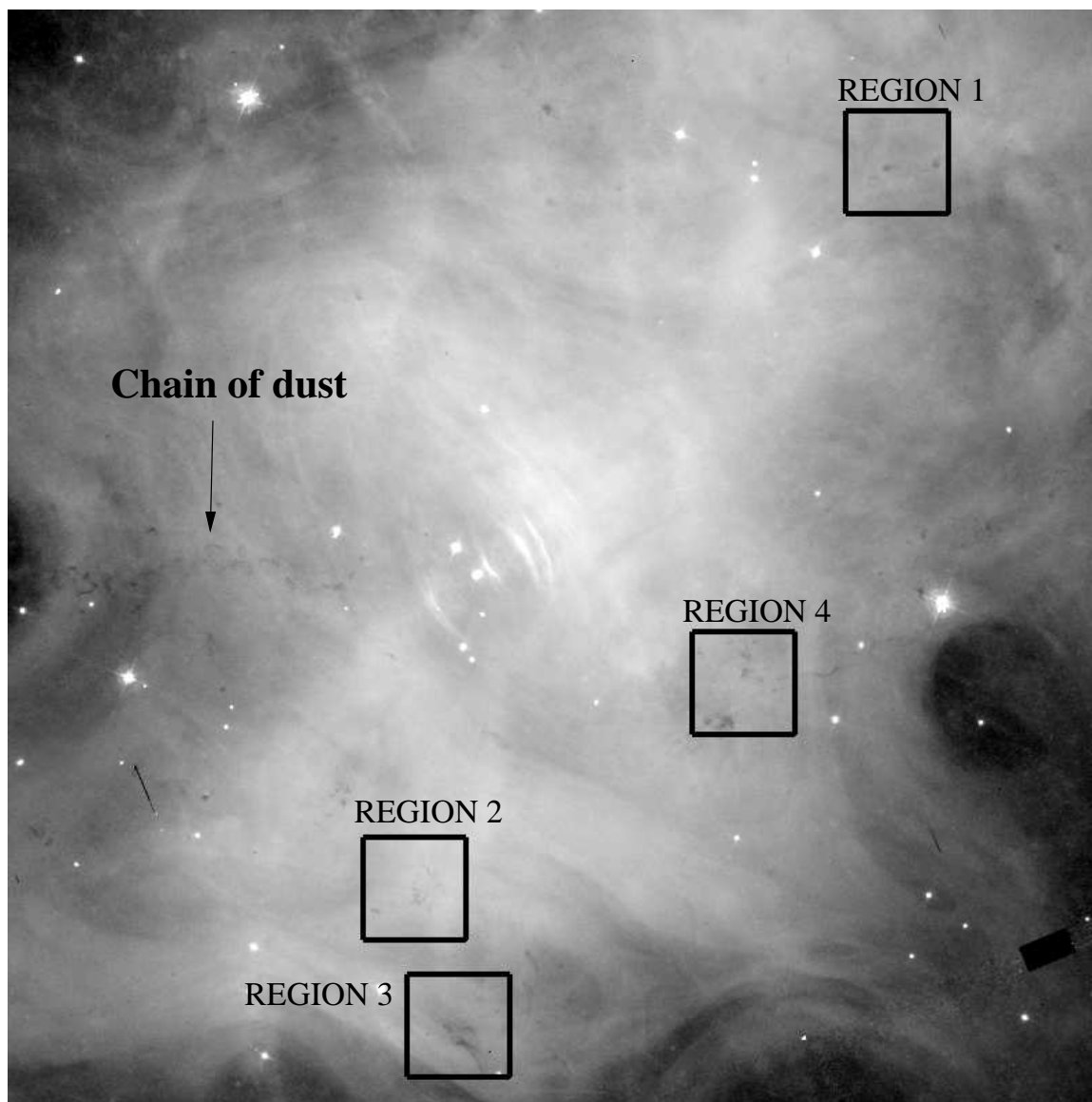


Figure 34. The F547M filter mosaic with boxes around dusty regions that are shown at higher resolution in later figures.

red-shifted filaments. The F-P data set by Lawrence et al. (1995) was utilized for this purpose. The resolution of the F-P data set is $0.84'' \text{ pixel}^{-1}$, so large filaments were easily distinguished in the F-P data and associated to the *HST* images. Small filamentary structures, such as small R-T fingers and isolated knots of emission, were not always resolvable in F-P images, and precise velocities could not be determined in those cases.

We must also take into effect the nature of the *HST* observations. The emission line images were taken using narrow-band filters, and the emission associated with fastest moving filaments along our line of sight [$\pm 1500 \text{ km s}^{-1}$, (Trimble 1968)] is Doppler-shifted outside of the filter bandpass (see Table 3). We created a visual representation of this limitation, shown in Figure 35, by adding F-P images together that had velocities where the [O III] emission line was within the FWHM of the filter (red), and also outside the FWHM of the filter (green). The [O I] filter captures a similar range of velocities, therefore the [O I] emission would be transmitted similarly to what is seen for [O III]. The [S II] emission line is a doublet; for this reason, at least one of the [S II] wavelengths is within the FWHM of the *HST* filter over a wider range of doppler-shifted velocities than either [O III] or [O I]. We are able to see [S II] emission over a wider range of velocities. Filaments along the front face of the nebula that are the most blue-shifted may show a weak correlation between [O I] and the dust, but only because their emission is shifted outside of the FWHM of the filter and is not completely represented. It is to be noted that these are precisely the regions where the dust is most easily viewed (near the center of the remnant) because the synchrotron

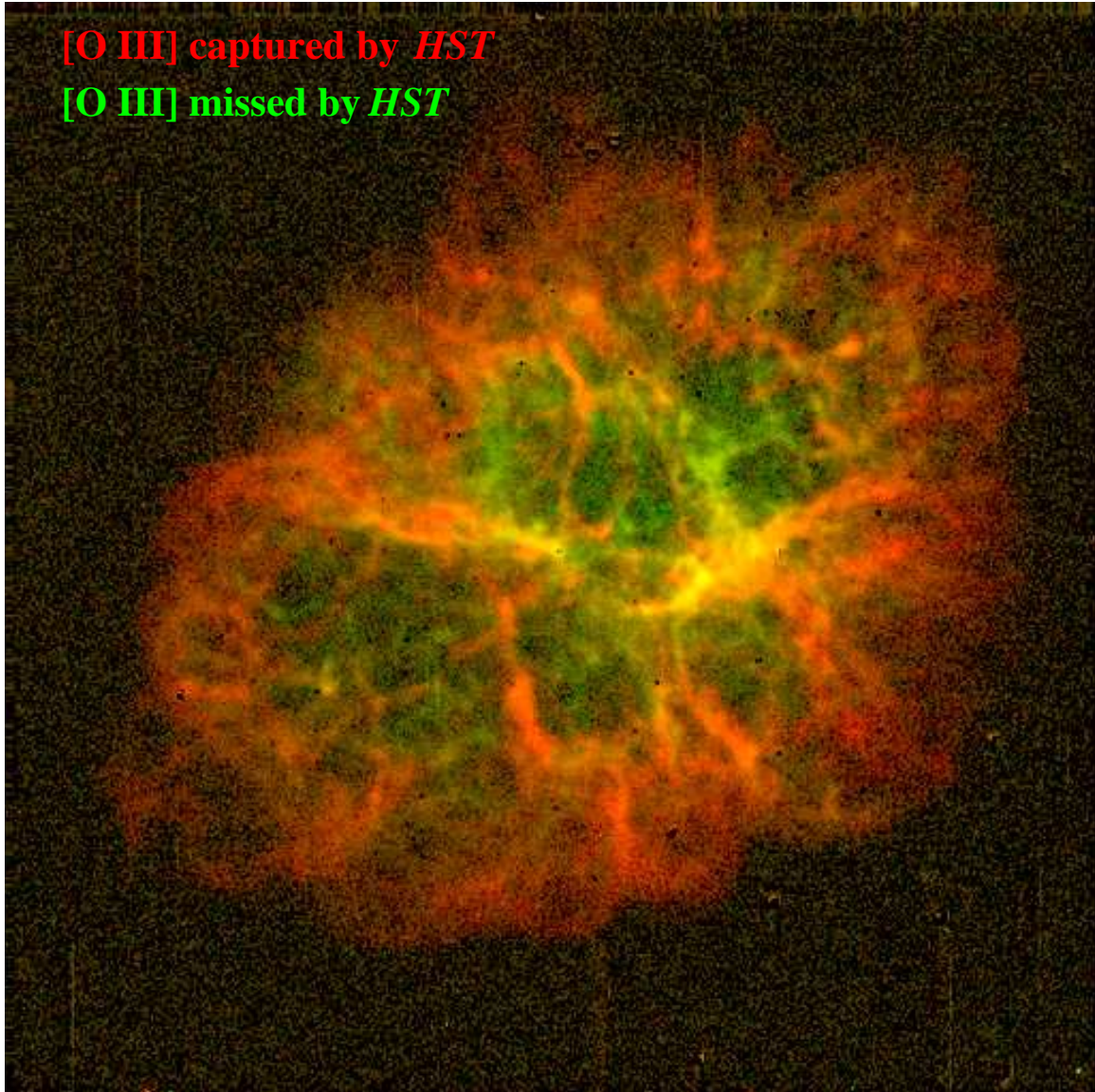


Figure 35. The transmission of [O III] with respect to location in the nebula. [O III] emission that was within the FWHM of the *HST* filter is shown in red, and the [O III] emission doppler-shifted outside of the *HST* filter, based on F-P studies of the Crab by Lawrence et al. (1995), is shown in green. It is apparent from this image that the [O III] is best represented at the edge of the nebula where the expansion of the filaments is in the plane of the sky.

nebula appears brightest there, making the extinction more noticeable. In order to make statements about the correlation between [O I], [S II] and [O III] and dust, we used the transmission curves provided in the *HST* Data Handbook to quantify the percentage of transmission that is expected at a given velocity (determined by F-P data). The transmission values were useful in determining if the association between the dust and line emission that is inferred by the line intensities is an accurate correlation, or if a weak association is due to the velocity of the filaments and the bandpass properties.

We know that the highest radial velocities are across the front face of the nebula. However, to determine the most accurate radial velocities for very specific locations in the nebula, we incorporated F-P data by Lawrence et al. (1995). The F-P data set was taken using exclusively [O III] emission and the data is separated over velocity ranges of 320 km s^{-1} . We recognize that our velocity estimates for a filament have inherent errors due to the velocity spread of the data cubes and also from assuming that the regions of low ionization emission (and dust) have the same radial velocity as the [O III] emission; however we do not believe these velocities are in error by more than about $\pm 200 \text{ km s}^{-1}$. When the velocity of a filament was determined, we used the central velocity of the F-P data cube to estimate the Doppler-shift of the [O III] emission line. The velocity of a specific filament was used to calculate the transmission percentage of each line emission filter in order to make statements about the correlation between dust and gas.

The four boxed regions in Figure 34 show areas where we have created high-

resolution images of the dust absorption features in Figures 36, 39, 40, and 41. These images have specific dust clumps labeled using the notation developed by FB90 when possible. However, in many instances we have been able to fully resolve the dust and have broken down features noted by FB90 into various segments that are followed by a lowercase letter. We have also labeled dust absorption features not discussed in earlier literature, and those are labeled with an ‘L’ followed by a numeric. Each of the high resolution images contains the *HST* continuum image and the *HST* [O III], [S II], and [O I] emission line images for the same region. We were able to estimate the amount of extinction based on the variation in continuum intensity at the locations where we see dust absorption features, and show these variations as contours in the high resolution images (Figures 36, 39, 40, and 41) that represent extinction values of $A_{5470} = 0.1$ mag and $A_{5470} = 0.2$ mag. We discuss each of these regions and the dust associated with them below.

Region 1 in Figure 34 is shown in high resolution in Figure 36. Contained in this region is FB4d, a relatively circular clump that has an extinction of 0.2 mag at the center. This dust is associated with the tip of one of the longest R-T fingers in the NW, labeled Finger 12 in Figure 27, and is the case where we previously suggested that densities may be high enough for molecular hydrogen to have formed. Significantly, this dust absorption feature shows little correlation with any of the emission lines. In fact, the dust appears in a “voided” region that is surrounded by emission, even [O I]. We have previously suggested that this area may be so dense and well-shielded that there is a core of molecular hydrogen. Molecular hydrogen has been detected in

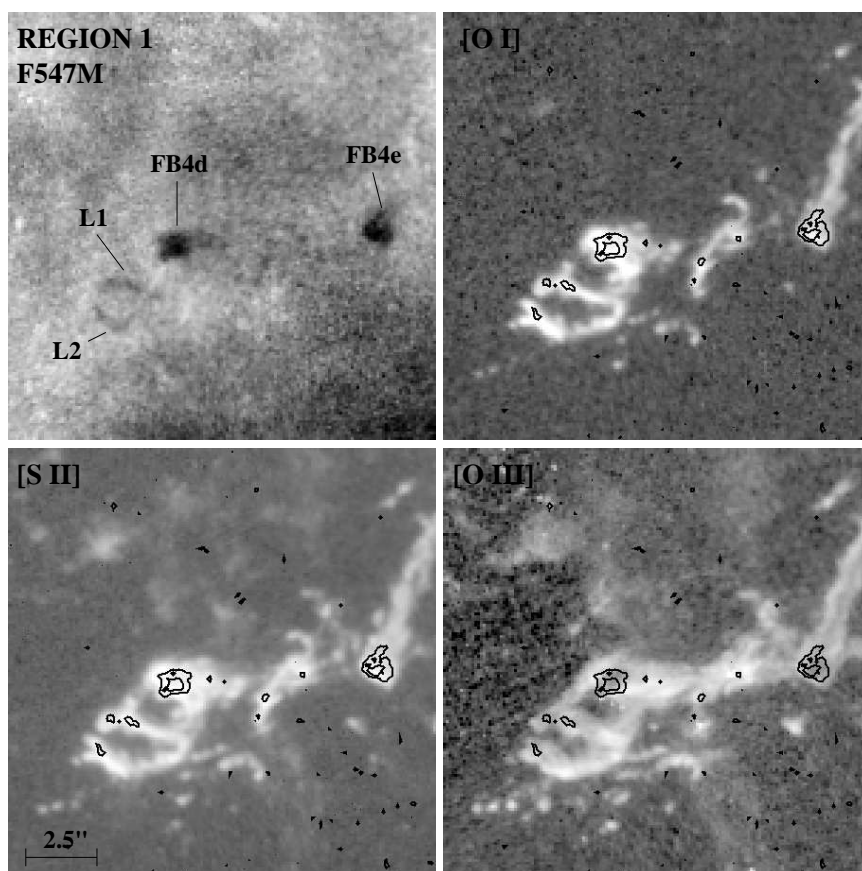


Figure 36. Region 1 from Fig. 34 shown in the continuum and line filters, respectively. This data is contained in field 2. Contours represent A_V values of 0.1 and 0.2.

two other locations in the Crab by Graham et al. (1990), but because they are on the far-side of the remnant (based on the F-P data) we can not determine if those features are coincident with dust.

Because the synchrotron light shows such high extinction at the location of FB4, and the finger is resolved in the F-P data so that we may estimate the finger's radial velocity, we estimated the dust-to-gas ratio for this feature for the purpose of comparing our value to that inferred by Sankrit et al. (1998) as a way of benchmarking our technique. The extinction can be estimated by measuring the decrease in continuum intensity over the location of the dust. We simply took a profile of the *HST* continuum at the location of FB4d to measure the reduction in continuum flux; the plot is shown in Figure 37a. The upper dashed line represents the average continuum intensity at that location and the lower dashed line represents the intensity after extinction. By measuring the drop in flux over the location of the dust clump, we may infer the amount of extinction of synchrotron emission due to dust. In this example, the upper dashed line represents the total flux of the synchrotron nebula without extinction, which we will call I_{TOT} , where I_{TOT} is the sum of the background flux and the foreground flux:

$$I_{\text{TOT}} = I_{\text{B}} + I_{\text{F}}. \quad (7.1)$$

The lower dashed line is the value of the extincted synchrotron emission (I_{DUST}) due to dust along the line-of-sight. It is decreased according to

$$I_{\text{DUST}} = I_{\text{B}}e^{-\tau} + I_{\text{F}}. \quad (7.2)$$

where τ is the optical depth. By taking the difference between I_{TOT} and I_{DUST} and

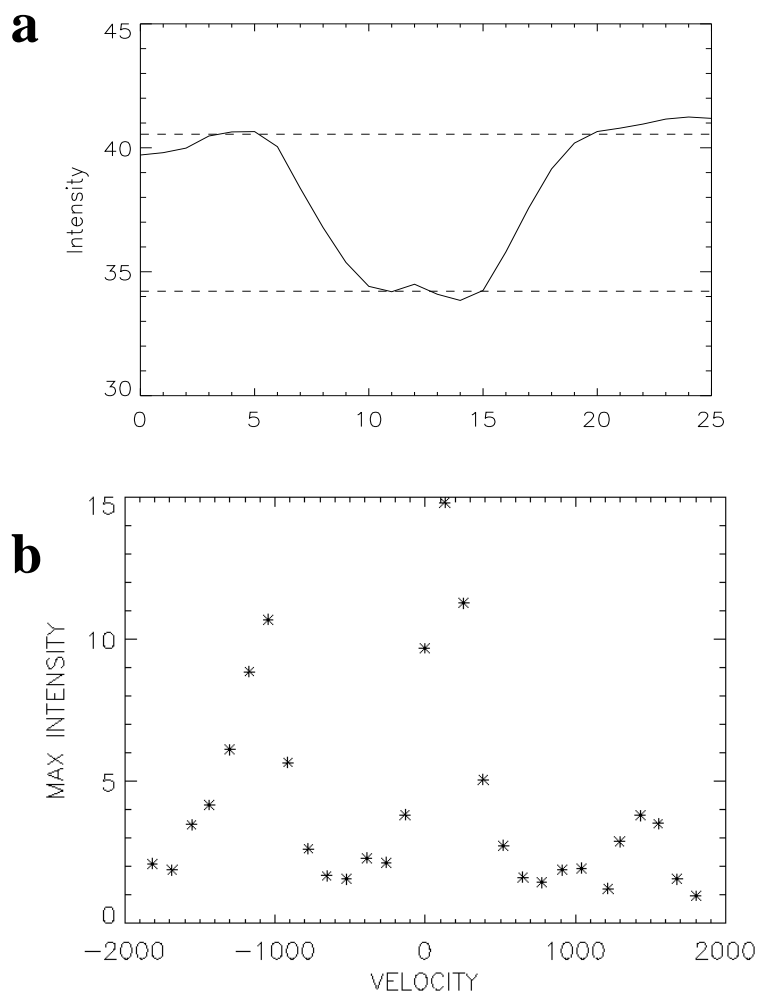


Figure 37. a.) A cut through the F547M continuum image at the location of FB4d. This allowed us to infer how much emission was being absorbed by the dust b.) A plot of intensities for F-P velocity cuts (in km s^{-1}) through the dust feature FB4d. Using the peaks of the intensities, we would then look at the images by eye to determine which velocity the line emission feature that correlates with the dust can be seen. Here it is the $v = +200 \text{ km s}^{-1}$ feature.

assuming that the synchrotron emission per unit volume is uniform throughout the nebula, we can relate the flux to the distance of the dust from the backside of the nebula, y :

$$I_B = yI_{\text{TOT}}. \quad (7.3)$$

We now have an equation for the optical depth:

$$\tau = -\ln \left[1 - \frac{1}{y} \left(1 - \frac{I_{\text{DUST}}}{I_{\text{TOT}}} \right) \right]. \quad (7.4)$$

Knowing the radial velocity of this dust is necessary to determine the percentage of synchrotron emission that lies in front of the dust absorption and is still included in the measured continuum flux. Figure 37b shows how we incorporated F-P data (Lawrence et al. 1995) to determine that value. The [O III] intensity was measured at the location of the dust for all of the F-P data cubes, and the associated profile for FB4d is shown in 37b. The peaks in the intensity vs. velocity plot correspond to filaments along that line-of-sight. The images of those particular velocity cubes were examined to determine which image contained Finger 12 (and FB4d). We estimate from the F-P data that FB4d has a radial velocity of $+200 \text{ km s}^{-1}$. If this feature is truly redshifted, there must be enough dust and/or background synchrotron emission to cause measurable extinction. Figure 38 is a schematic of the physical location of FB4d in the nebula. The view is from above the nebula, such that we would be viewing the nebula face-on (from Earth) when looking from the bottom of the figure “through” the nebula to the top of the figure. The black oval marks the contact-discontinuity between the synchrotron nebula and the filaments. FB4d is represented by a grey circle in the figure and has the vector, $v_r(\text{D})$ to represent its

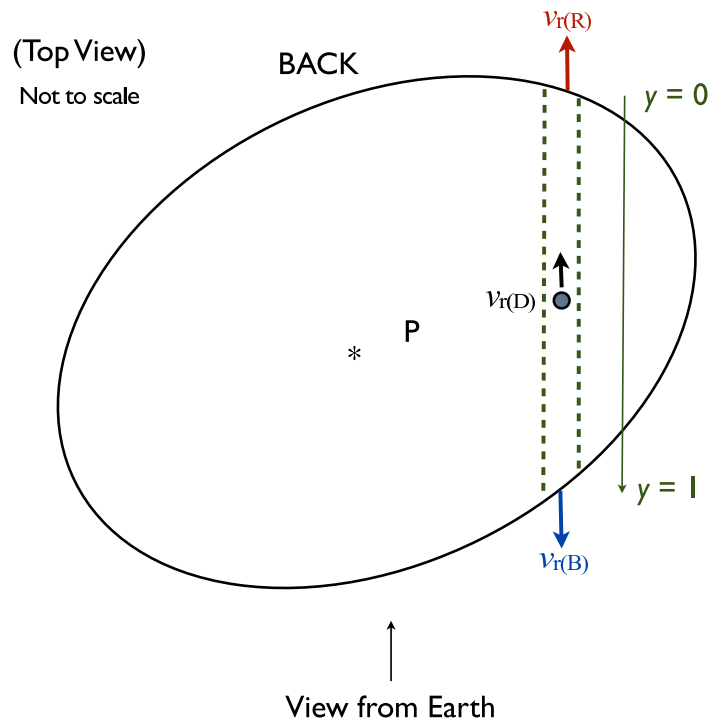


Figure 38. A schematic showing the location of a dust absorption feature (FB4d) with respect to the fastest moving filaments [$v_r(R)$, $v_r(B)$] along the line-of-sight from Earth and the location of the pulsar (P). The thickness of the synchrotron nebula at that location is y . The approximate explosion center is represented by an asterisk.

radial motion. The location of the pulsar is shown as ‘P’, and the expansion center is shown as an “*” in Figure 38 (not to scale). The area between the green dashed lines represents the column over which peak intensities were measured in the F-P velocity data cubes through the line-of sight of the dust absorption feature. The thickness of the column is y ; $y = 0$ represents the back of the nebula and $y = 1$ represents the front. The fastest expanding red- and blue-shifted filaments in that column are at the edge of the nebula and are expanding with velocities that are approximately proportional to their distance from the expansion center (Trimble 1968). The radial velocity of the red- and blue-shifted filaments ($v_r(\text{R})$ and $v_r(\text{B})$, respectively), were determined by the F-P data over the location of the dust clump. Using the assumption of homologous expansion, then the thickness of the synchrotron nebula can be determined from

$$y = \frac{v_r(\text{D}) - v_r(\text{R})}{v_r(\text{B}) - v_r(\text{R})}. \quad (7.5)$$

The F-P data (Figure 37b) were used to infer that the fastest moving filaments along the line-of-sight of FB4d have velocities of $\pm 1500 \text{ km s}^{-1}$ and the radial velocity of the dust is $+200 \text{ km s}^{-1}$. These values give a total thickness of $y = 0.43$ at this location, meaning that 43% of the synchrotron emission (along a line of sight not passing through the dust clump) is coming from behind the dust.

Now that we know the physical location of the dust along our line-of-sight, we may calculate the extinction due to dust at that location. $I_B = 0.43 \times 40.5 = 17.4$ flux units, which measures the total background flux. From Figure 37a, we see that $I_{\text{DUST}} = 34.2$ flux units, which is the total flux measured (foreground + extincted

background) at the location of the dust. The foreground flux, I_F , is simply the difference between the total flux “off” the dust and the total (unextincted) background flux, which is approximately 23 flux units. Substituting these values into the equation above gives $\tau = 0.45$. The extinction in magnitudes is equal to

$$A_{5470} = -2.5 \log_{10} \left(\frac{I_B e^\tau}{I_B} \right) = -2.5 \log_{10} e^\tau = -1.086\tau \quad (7.6)$$

and for FB4d we find that $A_{5470} = 0.49$ magnitudes.

We can use the above analysis to determine an overall gas-to-dust ratio for the dust absorption feature. Following the estimations of dust grains used by (Fesen & Blair 1990), which assume an ISM-like dust grain, we assume a dust radius of 0.075 μm and a bulk density of 2.0 g cm^{-3} . The column density of the gas, N_d , is calculated from

$$A_{5470} = 1.086 N_d Q_e \sigma_{\text{dust}} \quad (7.7)$$

where Q_e is the extinction efficiency factor and is equal to about 2 for the wavelength of the continuum filter (Spitzer 1978), and the cross section of a dust grain is $\sigma_{\text{dust}} = \pi r_{\text{dust}}^2 = 1.77 \times 10^{-10} \text{ cm}^2$. Substituting in our values, we get $N_d = 1.27 \times 10^9 \text{ cm}^{-2}$ for FB4d. As the mass of one dust grain is

$$m_{\text{dust}} = \rho_{\text{dust}} V_{\text{dust}} = \frac{4\pi}{3} r_{\text{dust}}^3 \rho_{\text{dust}} \quad (7.8)$$

and is equal to $3.5 \times 10^{-15} \text{ g}$, the mass column of dust for FB4d is this value times N_d and is equal to $4.4 \times 10^{-6} \text{ g cm}^{-2}$. Photoionization models by Sankrit et al. (1998) (Model F) estimate the mass column of hydrogen (assuming a helium abundance of 2 times solar) to be roughly $8.8 \times 10^{-5} \text{ g cm}^{-2}$ for long, well-developed fingers such as

the finger associated with FB4d. We can use these values to estimate the dust-to-gas ratio and estimated the ratio to be about 0.050 for FB4d. This is five times higher than the typical ISM value of 0.01 (Pei 1992). The photoionizational model F by Sankrit et al. (1998) has a differs from the measured spectra by about 8%. We infer an error to our dust-to-gas ratio of 0.050 ± 0.004 for this filament.

There are several other dust absorption features shown in Figure 36. The dust absorption feature labeled FB4e is coincident with low-ionization emission arising from the dense tip of a R-T finger. This finger has a low radial velocity according to the peak intensity plot of F-P data, indicating that it is viewed nearly edge-on with respect to our line of sight and is well sampled by all three emission line filters. We note that there is no dust along the length of the finger, and we find this to be typical of fingers in the NW (the longest fingers in the nebula). As noted in Chapter 5, this R-T finger shows a stratified ionizational structure. This is based on the hollow appearance of the [O III], as noted by Sankrit et al. (1998). The dust correlates with the strongest [O I] and [S II] emission, as expected if these areas are the most dense and most well-shielded areas of the finger.

Features L1 & L2 in Region 1 are also examples of dust at the tips of R-T fingers. Both L1 and L2 appear more extended and the amount of extinction is weaker, as noted by the contours. These fingers appear in the same velocity-space as FB4d, and we believe they may be slightly red-shifted. The emission lines are well sampled for L1 and L2, and the dust is correlated with the low-ionization lines.

Region 2 is shown at high resolution in Figure 39. FB2c, considered to be a

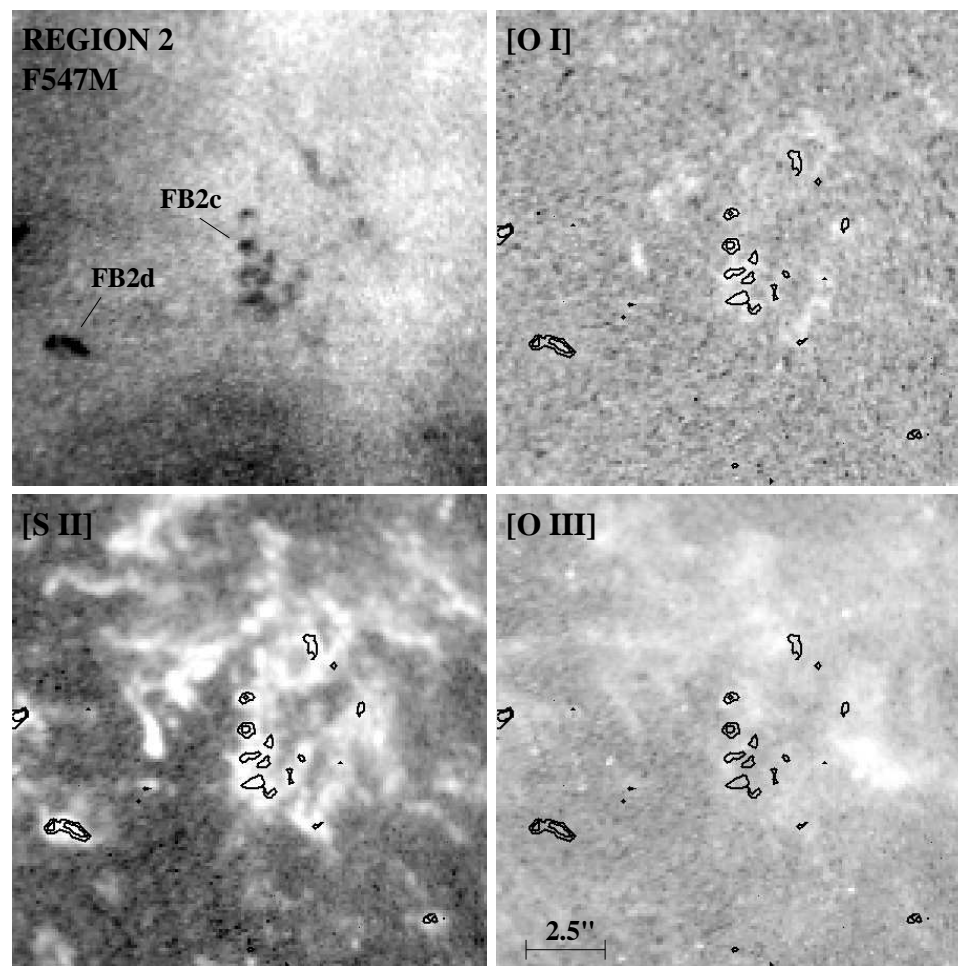


Figure 39. Region 2 from Fig. 34 shown in the continuum and line filters, respectively. Contours represent A_v values of 0.1 and 0.2.

single dust extinction feature by Fesen & Blair (1990), can be broken up into at least 6 - 7 circular clumps in our *HST* data that reach extinction levels of up to $A_{5470} = 0.2$ mag. It may be that our line of sight is along the length of the R-T fingers, such that when we observe the fingers from base-to-tip we see regularly spaced, circular areas of dust absorption. From this vantage point, we can not discern if the dust is concentrated at the tips of the fingers or throughout the length. These clumps have velocities of roughly -650 km s^{-1} according to F-P data. The [S II] emission is well sampled in this velocity range, but only up to a maximum of 96 percent of [O III] and 93 percent of the [O I] emission is transmitted. The appearance of a better correlation of dust with the [S II] rather than [O I] is probably due to velocity effects. There is no correlation between the [O III] intensity and dust extinction.

Figure 39 shows several more R-T fingers that are prominent in the [S II] image located to the left of FB2c. These fingers show no indication of dust. F-P data indicate that these fingers lie on the backside of the remnant and have velocities of $+1040 \text{ km s}^{-1}$. If there is dust in these fingers, we are unable to view it by absorption of synchrotron light because they are on the back-side of the nebula and are not absorbing synchrotron light along our line-of-sight.

The dust absorption feature FB2d has a velocity of about -950 km s^{-1} according to F-P images. The transmission of [O III] is less than 10% at these velocities, and is well outside of the FWHM of the filter. The same is true for [O I] emission. The [S II] emission, however, should be well sampled at these velocities. The emission line images reflect these differences in transmission due to the filters, as there is almost

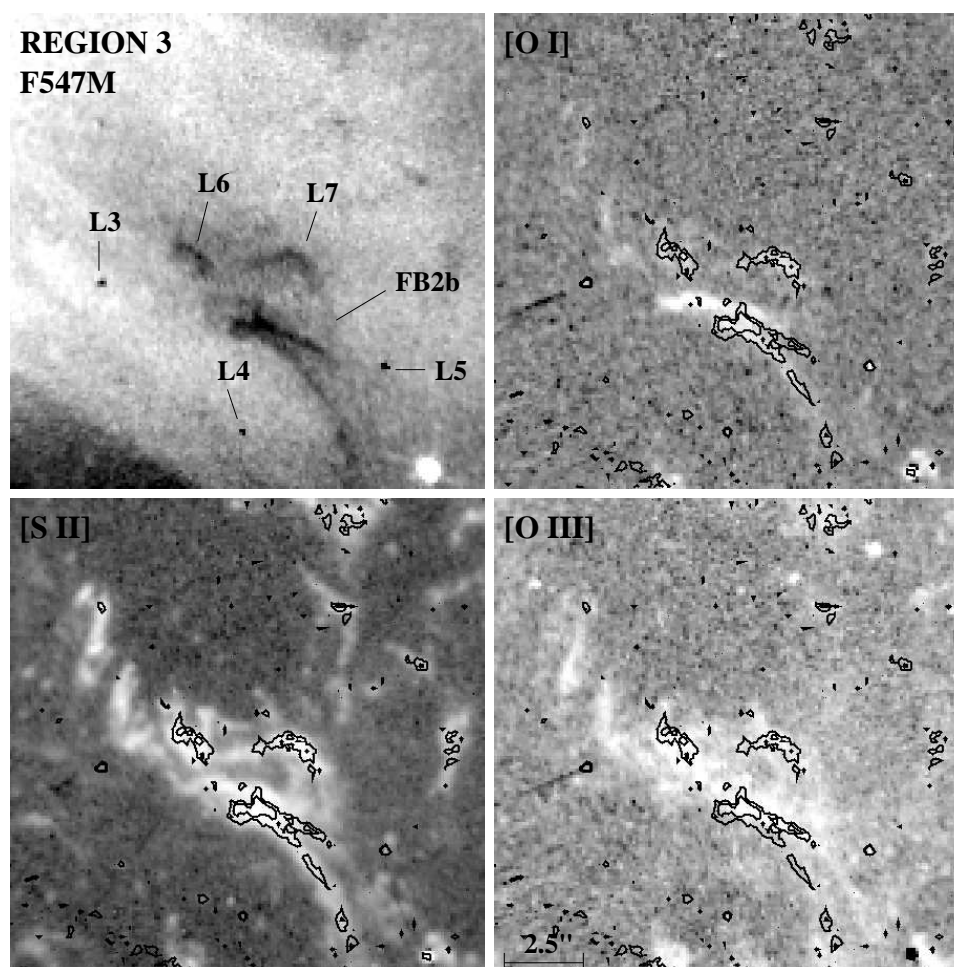


Figure 40. Region 3 from 34 shown in the continuum and line filters, respectively. This is part of the data from field 3. Contours represent A_v values of 0.1 and 0.2.

no indication of either [O III] or [O I] emission at the location of FB2d while there is [S II] emission.

Region 3, shown in Figure 40, contains the dust absorption feature FB2b that shows that in some instances dust exists along the length of a R-T finger. This example indicates that dust was present at the time the finger started forming and is being transferred to the tip of the finger along with the gas. Synchrotron extinction

at the location of FB2b reaches $A_v = 0.2$. We can not be certain that this dust is all located in one finger; the base of the finger has two distinct branches, so there could be two fingers crossing our line of sight here and the overall extinction is a combination of two fingers along our line-of-sight. Since the morphology is similar to what was modeled by Sankrit et al. (1998), we determined a dust-to-gas ratio for this feature. The velocity of the dust is about -525 km s^{-1} and the thickness of the synchrotron nebula at this location is $y = 0.69$. Using the measured drop in flux over the dust, we calculated optical depth to be 0.45. This morphology of this finger is most closely represented by Model D of Sankrit et al. (1998), therefore the mass column of hydrogen used to determine the dust-to-gas ratio was $4.63 \times 10^{-5} \text{ g cm}^{-2}$. We found that $M_{\text{DUST}}/M_{\text{GAS}} \approx 0.100$. This is a very high value and likely is overestimated due to an underestimate of the gas at this location. If we use the model for more well-developed fingers, as used for FB4d, we find $M_{\text{DUST}}/M_{\text{GAS}} \approx 0.05$. In reality it is likely somewhere between these two extremes. The photoionizational model (D) varies from the observed spectra by an average of 13%, and therefore we infer an error of 0.100 ± 0.013 for this finger.

There is a notable bright filament just above FB2b that is apparent in the [S II] and [O I] images that shows no strong indication of dust. In the Continuum image, there appears to be extinction but at values less than $A_v = 0.1$. The F-P data place both this filament and FB2b on the blue-shifted side of the remnant with an estimated velocity of $v \sim -500 \text{ km s}^{-1}$. At these velocities the [O III] and [S II] lines are well sampled and [O I] lies just outside the FWHM (transmission of about 11.5

percent). FB2b has a strong correlation with both [S II] and [O I] emission as we would expect due to shielding from photoionization and higher densities.

Region 3 contains what appear to be several isolated knots of emission that harbor dust, namely L3, L4 & L5. Knots such as these are believed to be an end-product of the R-T instability, where the density at the tip of a finger was high enough to overcome all of the magnetic forces and break free, leaving a sphere of gas inside the synchrotron nebula (Hester et al. 1996). Knots like these are surrounded by high-energy photons on all sides and therefore must be dense to be persistent over time and still show a stratified ionization structure. It may come as a surprise to realize that dust can be found within these structures, but in the case of L3, L4 and L5 the extinction values do reach $A_v = 0.2$. A similar dust-bearing knot of emission in the northern part of the remnant was imaged by Blair et al. (1997). The knots in these *HST* images are exactly coincident with strong [O I] emission and some [S II] and [O III] emission. Due to the small spatial scale of the knots, we could not get velocity estimates from the F-P data set to constrain the effectiveness of the transmission through the *HST* filter or determine dust-to-gas ratios.

L6 and L7 in Figure 40 appear as arcs and do not show any R-T development. The direction we are viewing from may hinder visibility of R-T instabilities here, or we could be looking at filaments that are stable. L6 and L7 could not be distinguished in the F-P data due to their small spatial size, therefore we can not discern their radial velocities. The dust associated with L6 and L7 is again coincident with the low ionization lines. In the [S II] emission line image, the structure appears more like

a connected filament rather than a R-T finger. If this is the case, then this provides further evidence that the dust and gas are well-mixed. If we were viewing these filaments face-on, for instance, and there were R-T fingers pointing into the nebula that were not visible, we would expect to see regularly spaced knots of emission rather than extended dust absorption features like L6 and L7. We believe these are dense filaments that may or may not be unstable, with the dust absorption arising from the dense cores of the filament(s) and not from tips of R-T fingers.

Region 4, shown in Figure 41, is part of a long chain of dust stretching from east to west across the nebula and mentioned in FB90. As before, the dust features labeled by FB90 can be broken into individual clumps when viewed at *HST* resolution. FB1a, in the lower left of Figure 41, shows high levels of continuum extinction and has large spatial scale in terms of the typical sizes of the dust absorption features seen in the Crab. Like L6 and L7 in Figure 41, we argue that this dust arises from the core of the filament and not in R-T fingers. The association of this dust absorption feature with [O I] and [O III] is weak, however it is coincident with [S II] emission. We estimate that the velocity of this dust absorption feature is between roughly -700 km s^{-1} and -500 km s^{-1} , which is outside of the FWHM of both the [O I] and [O III] filters and explaining the lack of association of the dust with these lines.

FB1b and FB1c are more isolated clumps of dust in comparison to FB1a, and they both are associated with the same filamentary structure based on the F-P images. The F-P data indicate an expansion velocity of between -700 km s^{-1} and -950 km s^{-1} . This rather large uncertainty in velocity is due to the [O III] emission

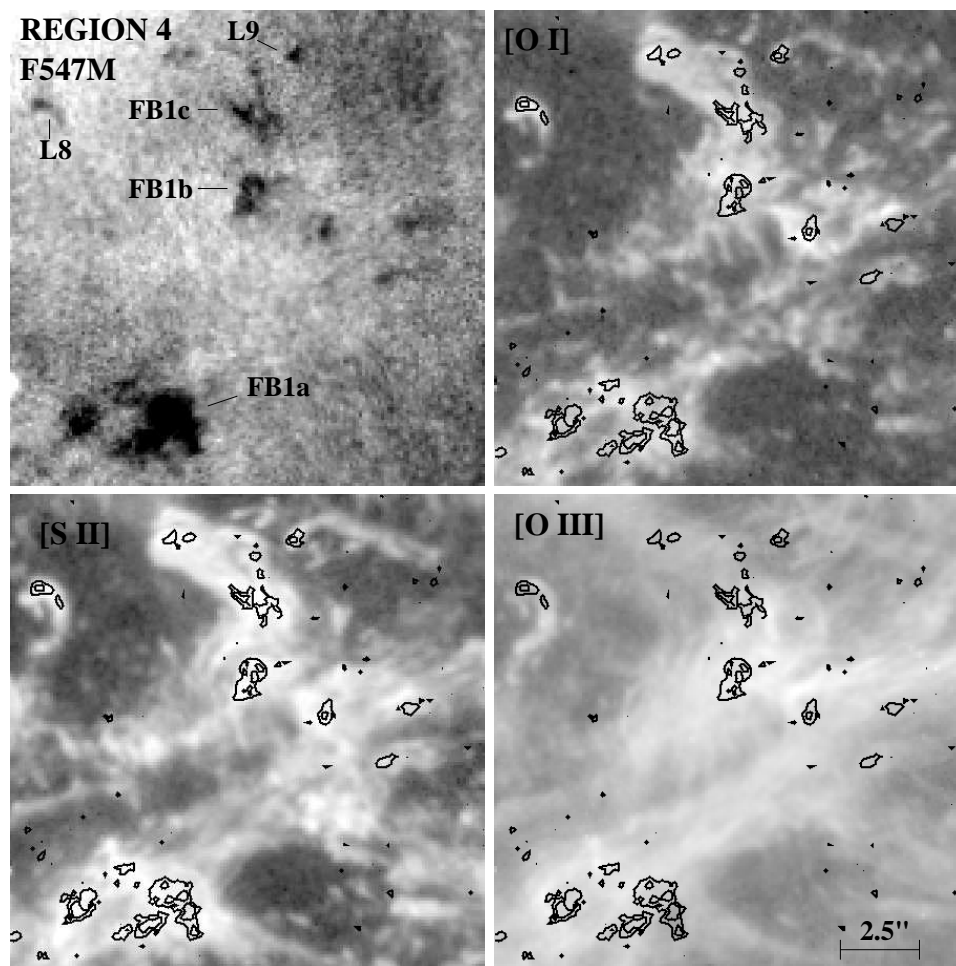


Figure 41. Region 4 from 34 shown in the continuum and line filters, respectively. Contours represent A_v values of 0.1 and 0.2.

from this filament being visible over a wide range of velocities. Assuming the higher of these two values, the $\lambda 6731$ [S II] line is still within the filter FWHM, however, only 3% of $\lambda 6717$, 1% of [O I], and less than 1% of [O III] emission are transmitted. Close inspection of the [S II] image reveals that the filament at the location of FB1b has a wave-like structure that is characteristic of the earliest stages of the R-T instability. Dust at this level of the instability is further evidence that the dust and gas are well-mixed in the ejecta and that dust exists in the filaments prior to R-T finger formation. FB1c could be either a filament or an edge-on R-T finger. If it is a R-T finger, it has dust at the tip and also where the finger attaches to the overlying filament. If it is a filament, then the clumps of dust may correlate to locations where the interface is unstable. The high velocities of these features make the dust appear to correlate best with the [S II] emission, however we are confident that this is simply due to the transmission properties of the *HST* filters. Finally, the dust absorption features L8 and L9 are very concentrated dust clumps that are clearly associated with the tips of R-T fingers in the line emission images. These features are too small to be resolved in the F-P data; however, the contours show that the amount of extinction is significant for both of these features.

7.4. Results

Combining the *HST* continuum mosaic which maps the dust on the front side of the nebula with the filamentary structure determined by the line emission images has allowed us to determine the association between the gas and dust over the entire nebula. *HST* provides a high enough resolution that we may resolve individual dust

clumps over the entire front-face of the nebula for the first time. We found that the dust is exactly coincident with low-ionization emission, namely [O I] and [S II], which is what we would expect since the dust must be in dense regions that are shielded from ionizing photons. In some of our examples, it appears that the dust is better correlated with [S II] emission rather than [O I] emission, however in those regions high radial velocities have shifted the wavelength of the [O I] emission outside of the FWHM of the filter. We used the correlation between dust and the low-ionization gas ([O I]) to conclude that all low-ionization regions contain some amount of dust and we have proven that dust is found in filaments of all morphological types rather than only regions where the R-T instability is dominant. This is an important result. The strong association of [O I] and dust strongly suggests that the dust is globally distributed and well-mixed with the gas, indicating that the bulk of the dust was swept up with the gas as the shock progressed through the freely expanding ejecta.

The dust is also not associated with filaments of a specific morphological type. In this study, we found evidence that dust can reside in newly unstable surfaces, along the lengths of R-T fingers, just at the tips of R-T fingers, and in isolated spherical clumps within the synchrotron nebula. It is clear from the *HST* data that dust, like the gas, is present at the time the interface between the synchrotron nebula and ejecta becomes unstable. The gas and dust flow down the length of an R-T finger and are compressed at the tip. Interestingly, the longest fingers (in the NW) show dust only at the tips, which is also where we find the strongest [O I] emission. If these fingers are the oldest fingers in the Crab, as we have suggested, it may be that the growth of

the fingers has slowed to the point where there is little to no mass transfer into the finger and the dust has accumulated at the tips of the fingers. Another possibility is that the column of gas along the length of the long fingers is too small to provide adequate shielding for the dust. Shorter fingers, such as Regions 2, 3 and 4, show some instances of dust along the entire lengths of R-T fingers and also in filaments that are just becoming unstable. We have found dense, stable filaments that have strong dust absorption ($A_{5470} \approx 0.2$ mag). This means that the filaments do not have to be R-T unstable in order to contain dust. Rather, the dust exists in the filaments before the R-T instability begins and the dust and gas are siphoned into the fingers together. This rules out the formation of dust in the R-T fingers as being the sole source of dust in the filaments. The dust was either formed in the supernova or is swept-up ISM dust.

We calculated the dust-to-gas mass ratio for two R-T fingers in the Crab. The results indicate that the dust-to-gas ratio is anywhere from 5-10 times higher than what is found for typical ISM in the Milky Way Galaxy [0.01, (Pei 1992)]. This is quite a significant result in terms of dust production in Type II supernovae, since it implies a significant fraction of the metals do condense into dust. Unfortunately, we are not able, at this time, to measure the total mass of dust or infer the total condensation efficiency.

We note that in order to conduct these calculations, we had to assume a dust grain size opacity when currently the size distribution and optical properties of dust in the Crab are not known. We followed the analysis by Sankrit et al. (1998) and FB90,

who argue that grain sizes smaller than what we have assumed would not effectively cause greater amounts of extinction of synchrotron emission at these wavelengths (because the grains are already as small as the wavelength of absorbed light.) We also assumed that the mass of gas in these filaments was similar to the fingers modeled by Sankrit et al. (1998) with similar morphological properties.

We also have errors in our estimates of the locations of the dust within the nebula. The large (320 km s^{-1}) velocity spread in the F-P data set makes it difficult to firmly associate a velocity to a given filament. Also, very bright filaments across the face of the nebula can be seen in the F-P data over a large range in velocities. The velocity of such a filament and therefore the dust contained within it must be estimated by using the intensity of the images. We believe our errors in velocities could be as large as 200 km s^{-1} which would mean an error of about 6% in the dust-to-gas ratio through the parameter y in equation 7.5. The F-P data is only available in [O III], and we have shown that the dust is coincident with the low-ionization emission. The low-ionization emission is contained in the cores of the filaments and at the tips of R-T fingers. With regards to the velocity errors due to the spread in F-P data we consider this error as minor in comparison. We did not take into account the 30° tilt of the nebula into the sky when we were calculating the thickness of the nebula through the line-of-sight of a particular dust feature, however the assumption of homologous expansion is consistent with what was found by Trimble (1968) and in the proper motion studies presented in this work. The amount of continuum flux coming from the behind a given dust feature would be higher than what we have

accounted for and the thickness of the nebula through the line-of-sight of the dust would be greater. We acknowledge that assumption of homologous expansion is also not accurate due to the tilt of the nebula into the sky. All of these cases affect how much of the continuum emission would have been from the foreground of the dust and would change our calculated dust-to-gas ratios but probably by less than 10%. More detailed studies of the sizes of dust grains in this nebula by observing the extinction of synchrotron light at various wavelengths would be a critical aid in determining more accurate ratios and the total mass of dust contained in the filaments.

The dust-to-gas ratios that we estimated for both R-T fingers are much higher than the ISM value. For this reason, we may dismiss the possibility that the dust in the Crab consists of dust from swept up ISM. This is a very significant result. We have already determined that the dust is not currently forming in the filaments, and now we have ruled out an ISM origin. We conclude that the dust present globally throughout the filaments was created in the supernova explosion and was swept up with the ejecta in the shock driven by the the PWN. This is important not only in studies of dust production in Type II SN, but also in models of the survival of dust grains in shocks.

CHAPTER 8

Conclusions

8.1. Summary

In this dissertation, we have used *HST* WFPC-2 observations covering the entire Crab Nebula to study the shock front, the development of R-T instabilities, and the presence of dust in the filaments. In addition to our own data, we have incorporated VLA radio observations of the synchrotron nebula by Bietenholz & Kronberg (1990) and F-P data by Lawrence et al. (1995) to gain a more thorough understanding of the location of the shock front, the shock velocity, three-dimensional distances in the nebula, and the radial velocity of the filaments.

We have found that there is a NW-SE asymmetry in the properties of the Crab Nebula that can be explained by the 120 km s^{-1} transverse velocity of the pulsar towards the NW (Kaplan et al. 2008). We used the geometrical information of the nebula determined by Lawrence et al. (1995) to create a 3-D ellipsoid that maps the boundary of the VLA radio data. We used the ellipsoid to calculate the distance between the edge of the radio emission (the approximate location of the shock front) from both the pulsar location and the estimated explosion center (Kaplan et al. 2008). We found that the synchrotron nebula is symmetrically distributed around the pulsar and has been carried along with the pulsar in time. The freely expanding supernova ejecta, though, are not related to the position of the pulsar but instead are distributed around the estimated explosion center. According to our 3-D model, the nebula is 1.4 times farther from the explosion center in the NW than it is in the SE. This has caused the shock, which is driven by the expansion of the pulsar wind nebula into the freely expanding ejecta, to have progressed through more ejecta in the NW

direction since the time of the explosion than it has in the SE. This has two effects. First, the filaments in the NW would contain more ejecta mass than the filaments in the SE because more ejecta has been swept up in the shock. Secondly, the density of freely expanding ejecta that the shock is encountering at this time would be less in the NW than the pre-shock ejecta density in the SE if we assume a power-law fall-off in ejecta density with distance from the explosion center ($\rho \propto r^{-n}$).

The conditions just described are the root cause of the NW-SE asymmetry that is seen in the *HST* images of the Crab Supernova Remnant. The pre-shock ejecta density determines the shock speed, assuming that the pressure at the edge of the synchrotron nebula is the same everywhere, according to $P = \rho v_s^2$. The shock speed directly affects how the filaments will form. For example, according to models by Sankrit & Hester (1997), shock speeds above 195 km s^{-1} result in post-shock gas that can not cool in the age of the remnant. No dense filaments will form behind shocks at those speeds, and this is what we believe is occurring in the NW where the synchrotron nebula has broken out and is now expanding beyond the [O III] emission (Figure 18). The SE, however, will have slower shock speeds because the pre-shock density is higher than in the NW. Gas shocked in the SE will cool and compress, which provides a barrier to the expanding synchrotron nebula. In the SE, the VLA radio data edge is coincident with the edge of [O III] emission meaning the synchrotron nebula is still contained by dense filaments. The ionizational structure at the edge of the nebula also indicates a difference in shock speeds. Lower ionization lines that form as the post-shock gas cools quickly via magnetic-dipole (forbidden) radiation,

such as [S II], form in the post-shock cooling region in the SE (Figures 22, 23 and 26). The NW side only shows [O III] emission at the edge of the nebula. In regions of the NW where filaments have formed, farther in from the edge and therefore at places closer to the expansion center, we still find evidence that the shock speeds are higher based on the thickness of the filaments. The filaments in the NW are thicker but less dense than the filaments in the SE. Thicker and less dense filaments indicate longer cooling times and faster shock speeds. In the SE, the ratio of [S II]/[O III] is higher than it is in the NW, because those filaments have cooled faster and have reached the densities that create adequate shielding from high-energy photons.

The density of the filaments and the acceleration of the contact-discontinuity determine how the R-T instability will take hold in the filaments. Models of R-T instabilities in supernova remnants by Jun (1998) show that acceleration of the interface must be positive before the instability will create long, well-developed fingers. We applied the results of the Jun (1998) by imposing an instantaneous expansion rate ($r \propto t^a$) and applying that expansion to the Crab Nebula by incorporating the transverse velocity of the pulsar and the variation of pre-shock ejecta density with distance from the explosion center to show that $a > 1$ and the synchrotron nebula is accelerating the filaments in the NW and has been doing so for some time. But the synchrotron nebula remains centered around the pulsar as it travels in the NW direction at 120 km s^{-1} , so even though the nebula is expanding in all directions, it has not significantly accelerated the contact-discontinuity in the SE. We have found that, at this time, the SE contact-discontinuity may be weakly accelerating. Since the

shock speed will accelerate in time as the pre-shock ejecta density decreases, the acceleration of the interface may increase in the future but it has not been accelerating for as long as the NW boundary. What we would expect, from these results, are long, well-developed R-T fingers in the NW where the acceleration has been occurring and where more ejecta mass has been swept up. In the SE, where the boundary is just marginally accelerating, we would expect the instability to be just taking hold. This would be indicated by unorganized filaments that may have a wave-like morphology and some small fingers. When we project the value of a in time, we predict that the expansion index will slowly decrease in time in the NW (but acceleration will continue to increase), while in the SE we predict the expansion index will slowly increase in time.

Acceleration is just one necessary component of R-T instabilities in the Crab. Hester et al. (1996) determined that the density of the filaments plays a crucial role in the development of R-T fingers, because the density must be high enough to overcome the magnetic tension in the filaments that keeps the interface stable, called the critical density. They estimated that the critical density in the filaments would be about $1.1 \times 10^{-21} \text{ g cm}^{-3}$ (assuming a pure helium gas). Our results indicate that in the NW, the fingers formed in the past, but due to the higher shock speeds that result in a lack of filament formation, we suggest that the density of the filaments will no longer reach the critical density and the instability will not be effective in the NW. In the SE, we believe the critical density may have been reached in the past, however the acceleration of the interface was not positive and the fingers could not develop.

Our results indicate that the SE boundary has only recently begun to accelerate. We expect the R-T instability will become less effective in the NW direction in time (R-T fingers will slow in their growth) whereas in the SE, we predict the R-T growth will become more dominant than it's been in the past — the longest fingers will be very long.

We tested these predictions through the observations and have found a strong asymmetry in the lengths and distributions of R-T fingers. Namely, the R-T fingers in the NW are up to 2 times longer than R-T fingers in the SE. In the SE, the filaments appear very unorganized. We argue that the instability may be less organized in the SE than it is in the NW because the interface has only recently begun to accelerate and the dominant wavelength of the instability has not yet been established. Also, since the acceleration began in the past in the NW, the fingers are older there and have had more time to grow.

The density of the R-T fingers are also different between the NW and SE, with the tips of R-T fingers in the NW being more ionizationally stratified indicating higher densities. In the NW, the tips have well-defined edges, with a sequence of ionization layers moving into the core: [O III] on the outside, [S II] farther in, and [O I] at the center. The SE tips do not have well defined edges in [O III] emission. The [S II] and [O I] emission is mostly concentrated in the tips, but the line intensities are much lower. All of the emission lines are about 3 times weaker in intensity in the SE R-T finger tips. This means that although the filaments are denser in the SE, the tips of the fingers are denser in the NW. This can be explained if the NW fingers are

older and have had more time to collect dense gas at the tips and which has been continually compressed. The shock speeds in the NW have increased over time and at this point the cooling region is too thick to produce dense filaments. In the SE, we believe the filaments have been unstable for a shorter period of time and therefore less gas has been siphoned into the fingers; the filaments contain the vast majority of the shocked, cooled, ejecta.

The final result of this dissertation was the association of dust with the low-ionization line emission in the Crab Nebula. Dust can be seen in the continuum image because the dust causes extinction of synchrotron emission and results in dark patches of lower intensity in the image. We expect this dust was formed from the explosion because the environment surrounding the Crab is relatively empty with respect to the typical ISM (Wallace et al. 1999). We analyzed the correlation of the locations of dust visible in the *HST* continuum image with the filamentary structure determined by the line images to determine the association between the gas and dust over the entire front-face of the nebula. We have found that dust can be found in some amount anywhere there is low-ionization emission. Dust can reside in the filaments, along the lengths of R-T fingers, just at the tips of R-T fingers, and in isolated, spherical clumps that are physically surrounded by synchrotron emission. We have compared the distribution of dust and low-ionization emission ($[\text{O I}]$) to determine that dust is found everywhere that we can constrain $[\text{O I}]$ emission to be coming from blue-shifted filaments. We also see dust in filaments of all morphological types. This is a significant result because it means that dust is globally distributed and well-mixed

with the gas, providing observational evidence that the bulk of the dust was swept up with the gas as the shock progressed through the freely expanding ejecta. It probably did not form predominantly in the densest regions of the filaments and fingers only, although we can't rule out some contributions.

We have calculated dust-to-gas ratios for dust clumps in the Crab by calculating the change in intensity of the synchrotron emission through the line-of-sight of the dust. The results indicate that the dust-to-gas ratio is anywhere from 0.050 ± 0.004 - 0.100 ± 0.013 , which is 5-10 times higher than what is found for the typical ISM. This is quite a significant result in terms of dust production in Type II supernovae and is higher than the value of 0.0075 estimated by infrared studies (Green et al. 2004). We note that in order to conduct these calculations, we had to assume a dust grain size when currently the size distribution and optical properties of dust in the Crab are not known, following the analysis by Sankrit et al. (1998) and FB90. We argue our assumption provides a lower limit on dust. Also, the thickness of R-T fingers varies throughout the nebula and the column of gas we assumed (Sankrit et al. 1998) could be in error. The large (320 km s^{-1}) velocity spread in the F-P data set (Lawrence et al. 1995) makes it difficult to firmly associate a velocity to a given filament and therefore it's exact physical location in the nebula. In some instances, this could cause an error in the dust-to-gas ratio of about ± 0.01 . Still, we conclude that the dust in the filaments provides too high of an extinction to be due to ISM dust, and the dust is too globally distributed to have formed only in the densest filaments, therefore the dust was produced in the supernova explosion and swept up

with the ejecta in the shock propagating outward from the synchrotron nebula.

8.2. Future Work

The observational studies presented in this dissertation provide an overall picture of the physical processes that are occurring in the Crab Nebula and explain the overall morphological properties of the filaments. There are many more studies that can be undertaken to test these ideas and provide better constraints on our estimates of shock speeds, ages and growth rates of R-T fingers, and dust-to-gas ratios.

It is not currently known if the fingers in the Crab Nebula are still growing. Growth rates could be estimated by using several epochs of data to determine if the fingers are getting longer in time. Once growth rates are known, the ages could be estimated by knowing the length of the finger and time between epochs. We expect that the growth rates of the NW and SE fingers are different because they are in different stages of development. Proper motion studies may also provide some idea of finger development; the model by Jun (1998) predicts that fingers that are in an active stage of growth are decoupled from the filaments that they are attached to and accelerated outward at a slower rate. Observational tests are warranted.

The composition of the Crab is known to vary over very small spatial scales and this is evident in our 3-filter *HST* image. For this reason, high-resolution spectra over very localized areas could be used to constrain the photoionization and shock models that were begun by Sankrit & Hester (1997) and Sankrit et al. (1998). The line strengths of density-probative emission lines would allow us to compare the densities of filaments and R-T fingers between the NW and SE sides that may provide more

clues to the ages of fingers and the amount of mass that has been transferred from the filaments to the fingers. The difference in density of the filaments between the NW and SE sides is due to different shock speeds between the two sides. The more accurate values of density would provide much better constraints on shock speeds. If the densities of specific filaments and R-T fingers are known, straightforward quantitative analysis would provide significant constraints on so many other important physical properties of the R-T instability and growth rates. Also, the high-resolution spectra could be used to create the first reliable map of the elemental abundance variation in the ejecta; the abundances could be used to constrain the progenitor star's mass and spectral type, while also providing information on how the ISM may be enriched by Type II supernovae. We have obtained spectra of the Crab Nebula that could be used for these purposes from the *Multiple Mirror Telescope (MMT)* on Mount Hopkins using the *Hectospec* Camera. The fibers on this camera have a diameter of just 1.5'' and are ideal for this type of study. The data cover more than 30 areas of interest, including the brightest filaments, tips of R-T fingers, regions where we have found dust, and locations outside of the remnant where there is the observationally elusive freely expanding ejecta.

Unfortunately, we are not able, at this time, to measure the mass of dust in the Crab from these observations. More information on the dust in the Crab could be found by observing the extinction of synchrotron light at various wavelengths to more accurately sizes constrain the sizes (and chemical make-up) of dust grains in this nebula. Studies of these kinds would be a critical aid in determining more accurate

ratios and the total mass of dust contained in the filaments, and could be useful in models of dust production in Type II supernovae.

REFERENCES

- Benford, G. 1984, ApJ, 282, 154
- Bertoldi, F. et al. 2003, *Å*, 406, L55
- Bethe, H.A. & Wilson, J.R. 1985, AJ, 295, 14
- Blair, W.P. et al. 1992, ApJ, 399, 611
- Blair, W.P. et al. 1997, ApJS, 109, 473
- Blandford, R. et al. 1983, Nature, 301, 586
- Blondin, J.M., Chevalier R.A., & Frierson, D.M. 2001, ApJ, 563, 806
- Bietenholz, M.F. & Kronberg, P.P. 1990, ApJ, 357, L13
- Bietenholz, M.F., Kronberg, P.P., Hogg, D.L., & Wilson, A.S. 1991, ApJ, 373, L59
- Bradt, H. 2008 *Astrophysics Processes The Physics of Astronomical Phenomena*. Cambridge University Press.
- Bucciantini, N. et al. 2004, A&A, 423, 253
- Burbidge, G.R. 1956, ApJ, 124, 416
- Bychkov, K. 1975, Soviet Ast., 118, 420
- Caraveo, P. & Mignani, R. 1999, A&A, 344, 367
- Carroll, B. & Ostlie, D. 1996, *Modern Astrophysics*. Addison-Wesley Publishing Company, Inc.
- Cernuschi, F., Marsicano, F. & Codina, S. 1967, Ann. d'Ap., 30, 1039
- Chandrasekhar, S. 1961, Hydrodynamic and Hydromagnetic Stability (Oxford: Oxford Univ. Press)
- Chevalier, R. 1977, in Supernova, ed. D. N. Schramm (Dordrecht:Reidel),53
- Chevalier, R. & Gull, T. 1975, ApJ, 200, 399
- Clark, D. & Stephenson, R. 1977, *The Historical Supernova*. Oxford:Pergamon
- Comella, J., Craft, H. Lovelace, R., Sutton, J., & Tyler, G. 1969, Nature, 221, 453
- Davidson, K. 1978, ApJ, 220, 177
- Davidson, K. 1979, ApJ, 228, 179
- Davidson, K. & Fesen, R. 1985, ARA&A, 23, 119

- Davidson, K. & Humphreys, R. 1976, *PASP*, 88, 312
- Dopita, M. & Sutherland, R. 2003, *Astrophysics of the Diffuse Universe*. New York: Springer-Verlag
- Dudziak, G. & Walsh, J.R. 1997, *HST Calibration workshop*, ed. S. Casertano, et al., 338
- Dwek, E., & Werner, M.W. 1981, *ApJ*, 248, 138
- Dwek, E. et al. 1983, *ApJ*, 274, 168
- Dwek, E. et al. 2007, *ApJ*, 662, 927
- Imhamdi, A. et al. 2004, *Å*, 426, 963
- Fesen, R., Shull, J.M., & Hurford, A.P. 1997, *AJ*, 113, 354
- Fesen, R. & Blair, W. 1990, *ApJL*, 351, L45
- Fesen, R. & Gull, T. 1986, *ApJ*, 306, 259
- Fesen, R. & Kirshner, R. 1982, *ApJ*, 258, 1
- Gaensler, B.M. & Slane, P.O. 2006, */araa*, 44, 17
- Graham, J.R. et al. 1983, *Nature*, 304, 709
- Graham, J.R. et al. 1990, *ApJ*, 352, 172
- Green et al. 2004, *MNRAS*, 355, 1315
- Hansen, C., Kawaler, S. & Trimble, T. 2004, *Stellar Interiors 2nd Edition*. New York: Springer-Verlag.
- Hester, J.J. et al. 1990, *ApJ*, 357, 539
- Hester, J.J. et al. 1994, *BAAS*, 26, 951
- Hester, J.J. et al. 1995, *ApJ*, 448, 240
- Hester, J.J. et al. 1996, *ApJ*, 456, 225
- Hester, J.J. et al. 2002, *ApJL*, 577, L49
- Hester, J.J. 2008, *ARA&A*, 46, 127
- Iben, I. & Renzini, A. 1983, *ARA&A*, 21,27
- Johnston, S. et al. 2005, *MNRAS*, 364, 1397

- Jun, B. 1998, ApJ, 499, 282
- Kaplan, D.L., Chatterjee, S., Gaensler, B.M., Anderson, J. 2008, ApJ, 677, 1201
- Kennel, C.G. & Coroniti, F.V. 1984a, ApJ, 283, 694
- Kifonidis, K., et al. 2004, *Å*, 408, 621
- Kotak et al. 2009, ApJ, 704, 306
- Lawrence, S., et al. 1995, AJ, 109, 2635
- Lucy, L.B. et al. 1989, in IAU Colloq. 120, Structure and Dynamics of Interstellar Medium, ed. G. Tenorio-Tagle, M. Moles, & J. Melnick (Berlin: Springer), 164
- MacAlpine, G. M., et al. 2007, ApJ, 133,81
- Marsden, P.L. et al. 1984, ApJL, 278, L29
- Merrill, K.M. 1980, IAU Circ., No. 3444
- Michel, F., Scowen, P., Dufour, R., Hester, J.J. 1991, ApJ, 368, 463
- Mioduszewski, A., Dwarkadas, V., & Ball, L. 2001, ApJ, 562, 869
- Ng C.-Y. & Romani, R.W. 2006, ApJ, 644, 445
- Ouellette, N., Desch, S. & Hester, J.J. 2010, ApJ, 711, 597
- Nozawa, T. et al. 2008, ApJ, 684, 1343
- Nozawa, T. et al. 2010, ApJ, 713, 356
- Nugent, R. 1998, PASP, 110,831
- Ouellette, N. Desch, S.J. & Hester, J.J. 2010, /apj, 710, 1
- Osterbrock, D.E. 1989, Astrophysics of Gaseous Nebulae and Active Galactic Nuclei (Mill Valley: University Science Books)
- Ostriker, J. & Gunn, J. 1969, ApJ, 157, 1395
- Pei, Y.C. et al. 1991, ApJ, 378, 6
- Pei, Y.C. 1992, ApJ, 395, 130
- Pettini, M. et al. 1997, ApJ, 478, 536
- Piddington, J.H. 1957, AJP, 10, 530

- Romani, R. et al. 1990, ApJL, 349, L51
- Ruderman, M. & Sutherland, P. 1975, ApJ, 196, 51
- Sankrit, R. & Hester, J.J. 1997, 491, 796
- Sankrit, R., et al. 1998, ApJ, 504, 344
- Shapiro, S.L. & Teukolsky, S.A. 1983 *Black Holes, White Dwarfs, and Neutron Stars The Physics of Compact Objects*. New York: John Wiley & Sons, Inc.
- Shull, P., et al. 1984, ApJL, 285, L75
- Silvia, D., Smith, B. D., & Shull, J. 2010, eprint arXiv:1001.4793
- Sollerman, J. et al. 2000, ApJ, 537, 861
- Spitzer, L. 1978, *Physical Processes in the Interstellar Medium* (New York: Wiley)
- Stancliffe R. & Eldridge, J. 2009, MNRAS, 396, 1699
- Strom, R. & Greidanus, H. 1992, Nature, 358, 654
- ugarman, B.E.K. et al. 2006, Science, 313, 196
- Sutherland R. & Dopita, M. 2003, ApJS, 88, 253
- ynge, J.L. 1956 *The Relativistic Gas*. Amsterdam: North Holland Publishing Company
- Temim, T., et al. 2006, ApJ, 132, 1610
- Trimble, V. 1968, AJ, 73, 535
- Trimble, V. & Woltjer, L. 1971, ApJL, 163, L97
- Trimble, V. 1982, Rev. Mod. Phys., 54, 1183
- Uomoto, A. & MacAlpine, G. 1987, ApJ, 93, 1511
- van den Bergh, S. 1970, ApJ, 160, 27
- Velusamy, T. 1984, Nature, 308, 251
- Wallace, B. et al. 1999, ApJ, 124, 181
- Wang, C. et al. 2006, ApJ, 639, 1007
- Wang, C. et al. 2007, ApJ, 656,399

Weaver, R., McCray, R., Castor, P.R., & Moore, R.T. 1977, *ApJ*, 218, 377

Woltjer, L. 1958, *Bull.Astr.Inst.Netherlands*, 14, 39

Woltjer, L. & Véron-Cetty, M.-P. 1987, *A&A*, 172, L7

Wooden, D.H. et al. 1993, *ApJS*, 88, 477

Wyckoff, S. et al. 1976, *ApJ*, 206, 254